

AGING EFFECTS ON THE FATIGUE PERFORMANCE
OF DEEP ROLLED BAR STEELS

by
Timothy D. Barlow

A thesis submitted to the Faculty and Board of Trustees of the Colorado School of Mines in partial fulfillment of the requirements for the degree of Master of Science (Metallurgical and Materials Engineering).

Golden, Colorado

Date: _____

Signed: _____

Timothy D. Barlow

Signed: _____

David K. Matlock
Thesis Advisor

Golden, Colorado

Date: _____

Signed: _____

Professor Michael J. Kaufman,
Professor and Head
Department of Metallurgical and Materials Engineering

ABSTRACT

The effects of solute nitrogen on the strain aging response after deep rolling and on the effects of deep rolling at a temperature selected to maximize the difference in the dynamic strain aging response on the fatigue behavior of two medium carbon bar steels was evaluated in reverse bending at room temperature. The nominally 0.38 wt pct carbon hot rolled bar steels included a plain carbon steel alloy specifically designed to have an elevated free nitrogen content and a steel alloyed with 0.09 wt pct vanadium, 0.010 wt pct titanium, and 0.020 wt pct aluminum in order to reduce solute nitrogen through precipitation. The static strain aging response of the two alloys was evaluated at room temperature on samples prestrained to 2.5% and aged at temperatures between 100 °C and 260 °C. The microalloyed steel exhibited a peak strain aging index at 220 °C, while the plain carbon steel exhibited a constant strain aging index at all temperatures tested nearly the same as the peak value of the microalloyed steel. Stress reversal tests at temperatures between 100 °C and 300 °C showed that the microalloyed steel exhibited limited dynamic strain aging (DSA) over the temperature range tested while at 150 °C the plain carbon steel exhibited a maximum in DSA. Samples were deep rolled at room temperature and at 150 °C, and aged after room temperature deep rolling at 100 °C, a temperature selected to maximize the difference in strain aging index between the two alloys. The effect of deep rolling at room temperature, is an increase in the endurance limit of 55% over the as received condition. For the microalloyed steel, the room temperature deep rolled endurance limit was equivalent to the samples aged at 100 °C and those rolled at 150 °C. In contrast the plain carbon steel with an elevated free nitrogen content exhibited 9.2% increase in endurance limit when aged and an 18.2% increase after deep rolling at 150 °C. The enhanced response of the high nitrogen plain carbon steel was attributed to the development of more stable dislocation structures and correspondingly residual stress fields due to the effects of solute pinning on dislocations.

TABLE OF CONTENTS

ABSTRACT	iii
LIST OF FIGURES	vi
LIST OF TABLES	x
ACKNOWLEDGEMENTS	xi
CHAPTER 1 INTRODUCTION	1
CHAPTER 2 BACKGROND	2
2.1 Fatigue	2
2.2 Strain Aging	3
2.3 Bauschinger Effect	7
2.3.1 Minimizing the Bauschinger Effect	10
2.4 Deep Rolling	10
2.4.1 Elevated Temperature Rolling	13
CHAPTER 3 EXPERIMENTAL METHODS	14
3.1 Materials Selection	14
3.2 Metallography	14
3.3 Mechanical Testing	15
3.3.1 Tensile Testing	15
3.3.2 Strain Aging	15
3.3.3 Bauschinger Effect Testing	16
3.4 Fatigue Testing	17
3.4.1 Fatigue Machine Calibration	19
3.5 Deep Rolling	20
3.5.1 Optimization of Rolling Load	20
3.5.2 Elevated Temperature Rolling and Aging	21
3.6 Fractography	22
CHAPTER 4 RESULTS	23
4.1 Metallography	23

4.2	Mechanical Testing	23
4.2.1	Strain Aging	25
4.2.2	Bauschinger Effect Testing	25
4.3	Fatigue Testing and Deep Rolling	28
4.4	Fractography	33
CHAPTER 5 DISCUSSION		38
5.1	Strain Aging Responses	38
5.2	Deep Rolling	40
5.3	Aging Effects on Deep Rolling	40
5.4	Comparison to Previous Results	42
CHAPTER 6 SUMMARY		46
CHAPTER 7 FUTURE WORK		47
REFERENCES CITED		48
APPENDIX A TRANSMISSION ELECTRON MICROSCOPY		52
APPENDIX B X-RAY DIFFRACTION MEASUREMENT OF RESIDUAL STRESSES		55
B.1	X-Ray Diffraction Procedure	55
B.2	Analysis of X-Ray Diffraction Data	55
B.3	Results and Discussion of X-Ray Diffraction	56
APPENDIX C SURFACE FINISH		59
APPENDIX D MICROHARDNESS		61

LIST OF FIGURES

2.1	(a) shows the applied stress in a bending bar with no residual stresses present, (b) shows the residual stress profile typical of a shot peened part, and (c) shows the two stress profiles superimposed on one another [1]. Notice that the maximum tensile stress at the surface is reduced by the residual stress profile.	3
2.2	A schematic diagram showing the basic strain aging behavior of a low carbon steel. If a steel sample is loaded in tension to point X along the curve and unloaded (region A), then loaded again in tension immediately with no time to age it returns to point X with no discontinuous yielding. If a sample is loaded in tension to point Y and unloaded (region B) and aged before being reloaded in tension an increase in flow stress and a return of discontinuous yielding is seen in region C [1].	4
2.3	Stress strain curve from Baird [2] for a low carbon steel that is restrained to point A then unloaded and aged (curve b). This gives rise to a change in the flow stress shown as ΔY in this figure. This ΔY parameter can be used to quantify the strain aging response of a material at a given temperature and aging time. Curve a shows a sample that is loaded to point A then unloaded and loaded again immediately with no aging.	5
2.4	Engineering stress versus strain plots of two 1020 steels with different nitrogen contents [3]. The 1020 steel in (a) contains only 12 ppm N and even with this low amount DSA is observed at elevated temperatures. The 1020 has 180 ppm nitrogen and the serrated flow and flow stress is much higher in the 200 °C to 316 °C region due to the higher interstitial content.	7
2.5	A plot of the strain hardening exponent versus temperature of a 1020 steel with different amounts of nitrogen [3]. The steel with the largest peak in strain hardening exponent is the one with the highest nitrogen content.	7
2.6	A plot of strain aging index versus wt pct N with different amounts of Mn. As the amount of Mn increases the strain aging index is decreased [4].	8
2.7	A plot of flow stress at 10% strain versus temperature of a 0.1 wt pct C steel with different amounts of N and Mn. In the curves with no N the flow stress decreases with increasing temperature. When N is present there is an increase in flow stress with temperature to a peak at approximately 250 °C which is indicative of DSA occurring [4].	8
2.8	A schematic of a metal loaded in tension then compression from Li <i>et al.</i> illustrating the Bauschinger effect and showing the various parameters used to quantify the effect [5]. Both the tensile and compressive portions of the stress strain curve have been plotted in the tensile portion of the plot to simplify presentation. A clear drop in the yield stress is seen in the compressive part of the curve as well as permanent softening. Had the loading history been reversed (loaded in compression then tension) the curves would look the same.	9
2.9	Schematic showing typical case depths of various surface treatments. Deep rolling shows the greatest case depth of the purely mechanical treatments [6].	11
2.10	Diagram from Kloos <i>et al.</i> [7] showing parameters necessary to define a deep rolling process. . .	11
2.11	S-N curves for the baseline and deep rolled conditions for C38M (a sulfur modified and microalloyed 1038 ferrite pearlite steel). A baseline endurance limit of 241MPa (35 ksi) is observed with a deep rolled endurance limit of 386 MPa (56 ksi). This represents a 60% increase in endurance limit in the deep rolled conditioned versus the baseline condition [8].	12

2.12	Effect of residual stresses on the crack propagation behavior of a AISI 4140 steel. The vertical axis is the value of ΔK as a function of crack length with a dashed line at the value of ΔK_{th} and the horizontal axis is the crack depth with 0 being the surface. The compressive residual stresses decrease the effective applied stress to slow or even completely arrest the crack [6].	12
2.13	S-N curves for the baseline, room temperature rolled (RT), and elevated temperature rolled (RT) C38M from Richards [8]. The baseline endurance limit is 241 MPa (35 ksi), RT endurance limit is 386 MPa (56 ksi), and the HT endurance limit is 524 MPa (76 ksi). The HT endurance limit is a 36% improvement over RT and a 117% increase over the baseline condition.	13
3.1	An axial view of where deep roll samples (Figure 3.7) were machined out of the as received bars. All mechanical test samples were machined from the same radius as the deep roll samples. C38M was received in 7.62 cm (3 in) bars (a) and C38N2 was received as 10.8 cm (4.25 in) bars (b). (All units are shown in inches)	15
3.2	Tensile test sample geometry used for room temperature temperature tests and the strain aging study, all units are in inches.	16
3.3	A graphical representation of the calculation of $\Delta\sigma$ from strain aging curves of C38N2 aged at 100 °C for 35 minutes	16
3.4	Bauschinger effect test sample as developed by Richards [8] according to ASTM E 606-4 low cycle fatigue specimen guide [9]. All dimensions are in inches.	17
3.5	A typical Bauschinger effect test conducted in this study of the C38M material conducted at room temperature. The compressive portion of the test is also shown in the tensile region of the graph for ease of representation.	17
3.6	The 100 kip MTS servo-hydraulic frame with woodsmetal alignable grips and heat lamps in place for elevated temperature Bauschinger effect testing. The matte black paint to improve heating from the lamps is visible on the surface of the sample as well as the thermocouple wires from the spot welded k-type thermocouple for temperature control.	18
3.7	Deep Rolling fatigue sample developed by Richards [8]. (All dimensions are shown in inches)	19
3.8	Strain gage set up for calibration of SF-1U fatigue machines showing the strain gaged bar with one gage on top and another on the bottom in the grips.	19
3.9	A top view of the strain gaged bar in the grips for bending fatigue tests on the SF-1U fatigue machines.	20
3.10	Deep Rolling Device (DRD) developed and built by Richards [8] at CSM. The tripod load roller arrangement can be seen as well as the load cell and the hydraulic actuator.	21
4.1	Light optical micrographs of C38M (a) and C38N2 (b) etched with a 4% nital solution. Both microstructures consist of ferrite and pearlite with manganese sulfide (MnS) stringers also present in the microstructure. These micrographs are taken from the same radius in the as received bars as the deep rolling samples were sectioned from and viewed radially.	23
4.2	Example engineering stress strain curves for C38M and C38N2 at room temperature.	24
4.3	Two distinct yield behaviors were observed in the tensile testing and prestrain portion of the strain aging study in the C38N2 material. The difference in the two yielding behaviors is the amount of yield point elongation. After yield point elongation C38N2 exhibited the same uniform elongation and work hardening behavior independent of the amount of yield point elongation exhibited.	24
4.4	$\Delta\sigma$ versus temperature for C38M and C38N2. The effect of temperature on the strain aging index, $\Delta\sigma$, for C38M and C38N2 steels prestrained to 2.5% and aged for 35 minutes at the indicated temperatures.	26

4.5	Elevated temperature stress strain curves for the tensile portion of the stress reversal tests for C38M (a) and C38N2 (b). Each curve on (a) and (b) represent one test performed at the temperature listed to a value of 3% strain.	27
4.6	Flow stresses plotted versus temperature for yield stress (a), 1% plastic strain (b), and 2% plastic strain for C38N2 and C38M.	28
4.7	Engineering stress versus engineering strain curves for C38M (a) and C38N2 (b) tested at 150 °C. The compressive portion of the test is also represented in the tensile region of the plot for ease of representation. The flow curve for C38M is smooth, whereas the C38N2 flow curve is serrated which is a result of dynamic strain aging taking place during the test.	29
4.8	A plot of BEF versus temperature from 20 °C to 300 °C. An isotropically hardening material will have a BEF of 1, so as the BEF increases this means the Bauschinger effect is less prevalent. At least two tests were run at each temperature shown, each data point represents an individual test.	29
4.9	SN curve representing the as received fatigue performance of C38M (a) and C38N2 (b). Open symbols represent samples that failed and filled symbols represent run out samples. The nominal endurance limits of C38M and C38N2 are 310 MPa and 241 MPa, respectively.	30
4.10	Optimization curve with the number of cycles to failure at stress plotted versus deep rolling load. The C38M was tested at 552 MPa (80 ksi) and C38N2 was tested at 483 MPa (70 ksi). The optimized rolling load was chosen to be 10.5 kN (denoted with an arrow) for both C38M and C38N2. Not only was the increase in fatigue life taken into consideration but also the appearance of surface damage due to the deep rolling process.	31
4.11	Light optical images of C38N2 rolled at 12.5 kN (a) and 20 kN (b). Small cracks were observed in the fillet when rolled at 12.5 kN (marked with arrow) with much more extensive damage visible on the surface when deep rolled at 20 kN.	32
4.12	SN curves for C38M (a) and C38N2 (b) deep rolled at a rolling load of 10.5kN at room temperature. The deep rolled endurance limits for C38M and C38N2 are 483 MPa and 379 MPa, respectively.	33
4.13	SN curves for C38M (a) and C38N2 (b) after being deep rolled at 10.5 kN at room temperature and aged at 100 °C for 35 minutes. The aged endurance limits of C38M and C38N2 are 483 MPa and 414 MPa, respectively.	33
4.14	SN curves for C38M (a) and C38N2 (b) when deep rolled at 10.5 kN at a temperature of 150 °C with endurance limits of 483 MPa and 448 MPa, respectively.	34
4.15	Fracture surfaces of as received condition material (a) C38M tested at 339 MPa (50 ksi) for 616,848 cycles before failure and (b) C38N2 tested at 275 MPa (40 ksi) for 2,304,272 cycles before failure.	34
4.16	Fracture surfaces of (a) C38M tested at 552 MPa (80 ksi) for 30,646 cycles before failure and (b) C38N2 tested at 483 MPa (70 ksi) for 38,715 cycles before failure in the as received condition. . .	35
4.17	Fracture surfaces of (a) C38M tested at 509 MPa (75 ksi) for 5,224,261 cycles before failure and (b) C38N2 tested at 416 MPa (60 ksi) for 1,538,816 cycles before failure after being deep rolled at 10.5kN at room temperature.	36
4.18	Fracture surfaces of (a) C38M tested at 690 MPa (100 ksi) for 41,423 cycles before failure and (b) C38N2 tested at 552 MPa (80 ksi) for 46,923 cycles before failure in the room temperature deep rolled condition.	36
4.19	Fracture surfaces of (a) C38M tested at 509 MPa (75 ksi) for 1,618,563 cycles before failure and (b) C38N2 tested at 449 MPa (65 ksi) for 1,355,459 cycles before failure after being deep rolled at 10.5kN and aged at 100 °C for 35 min.	37
4.20	Fracture surfaces of (a) C38M tested at 509 MPa (75 ksi) for 9,851,000 cycles before failure and (b) C38N2 tested at 482 MPa (70 ksi) for 594,193 cycles before failure after being deep rolled at 10.5kN at 150 °C.	37

5.1	SN curves for C38M (a) and C38N2 (b) when deep rolled at 10.5 kN at a temperature of 150 °C (HT) with nominal endurance limits of 483 MPa and 448 MPa. Also presented are the as received (Baseline) and room temperature (RT) deep rolled conditions.	42
5.2	Light optical micrographs of C38M (a), C38M* (b), and C38N2 (c) etched with a 4% nital solution. All three microstructures consist of ferrite and pearlite with manganese sulfide (MnS) stringers also present in the microstructure. These micrographs are taken from the same radius in the as received bars as the deep rolling samples were sectioned from and viewed radially.	44
5.3	Strength enhancements (and contributions of individual strengthening mechanisms) to a 20MnSi (<i>i.e.</i> 0.0 V) base reinforcing bar steel resulting from additions of V (0.11 V, 0.0085 N; wt pct) or both V and N (0.12 V, 0.018 N; wt pct). Figure attributed to Gladowaski as reported in [10]. . .	45
A.1	Bright field TEM micrograph of C38M* after being deep rolled at 10.5 kN at room temperature showing a high dislocation density in the ferrite.	52
A.2	Bright field TEM micrograph of C38M* after being deep rolled at 10.5 kN at room temperature showing a high dislocation density in the pearlitic ferrite. The dark laths are cementite and the lighter colored areas are ferrite. The cementite laths appear to be cleaved at a characteristic angle with dislocation coming off of the tips of the cleaved lamellae in the ferrite.	53
A.3	A closer view of the TEM micrograph presented in Figure A.2. Dislocations are evident in the pearlitic ferrite. The cementite lamellae appear to be sheared at a characteristic angle related to the angle most of the dislocations are oriented in the ferrite.	53
A.4	Bright field TEM micrograph of C38M* after being deep rolled at 10.5 kN at room temperature. A characteristic angle at which the cementite laths appear to be sheared at can be seen in this micrograph.	54
A.5	Bright field TEM micrograph of C38M* after being deep rolled at 10.5 kN at room temperature. Straight cementite lamellae with a "kink" at a characteristic angle can be seen in this image. . .	54
B.1	Crystallite sizes for C38N2 deep rolled at room temperature then aged from the modified Williamson-Hall approach. The as rolled sample was tested before undergoing fatigue testing, the 90 ksi interrupted sample underwent 19,994 cycles at 90 ksi before x-ray diffraction, 60 ksi interrupted underwent 5,135,18 cycles at 60 ksi, and 60 ksi run-out underwent 10,000,000 cycles at 60 ksi. 60 ksi is the endurance limit of C38N2 deep rolled at room temperature then aged condition. . .	57
B.2	Strains calculated using Equation B.2 for the (110) (a) (200) (b) and (211) (c) planes for C38N2 in the deep rolled at room temperature then aged condition. The as rolled sample was tested before undergoing fatigue testing, the 90 ksi interrupted sample underwent 19,994 cycles at 90 ksi before x-ray diffraction, 60 ksi interrupted underwent 5,135,18 cycles at 60 ksi, and 60 ksi run-out underwent 10,000,000 cycles at 60 ksi. 60 ksi is the endurance limit of C38N2 deep rolled at room temperature then aged condition.	58
C.1	Surface profiles before deep rolling for C38M in the polished condition (a) and in the as machined condition (b).	59
C.2	Surface profiles after deep rolling for C38M in the polished condition (a) and in the as machined condition (b).	60
D.1	Microhardness traverses of C38N2 deep rolled with a rolling force of 10.5 kN at room temperature (a) and at 150 °C (b). 0 represents the surface of the fillet in the root.	62
D.2	Microhardness traverses of C38M deep rolled with a rolling force of 10.5 kN at room temperature (a) and at 150 °C (b). 0 represents the surface of the fillet in the root.	63

LIST OF TABLES

3.1	Compositions of Steels Used in Deep Rolling Project (wt pct)	14
4.1	Ferrite-Pearlite fractions and grain sizes of C38M and C38N2	23
4.2	Room temperature mechanical properties of C38M and C38N2	25
4.3	Nominal endurance ($\sigma_{e-nominal}$) limits of all conditions tested	32
5.1	The different amounts of nitrogen and microalloying elements present in C38M and C38N2 in wt pct.	38
5.2	Comparison of as received and room temperature rolled endurance limits (σ_e) with k_t taken into account.	40
5.3	Endurance limits for all conditions tested with the stress concentration factor k_t of 1.5 taken into account.	42
5.4	Compositions of Steels Used in Deep Rolling Project, with C38M* used previously by Richards [8] listed in (wt pct)	43
5.5	Ferrite-Pearlite fractions and grain sizes of C38M and C38N2	43
5.6	Mechanical Properties of C38M and C38N2 compared with reported data from Richards C38M* [8]	44
5.7	Predicted yield stresses and experimental yield stresses	45
B.1	Calculated depth of penetration for Cr $k\alpha_1$ x-rays in ferrite.	57
C.1	Surface roughness parameters R_a and R_q for the polished and as machined conditions before and after deep rolling with the cylinder and tilt terms removed from the analysis using Vision32 software.	59

ACKNOWLEDGEMENTS

I would like to thank my mother, Lorna Barlow, for always being supportive of me in whatever I do and especially in my education. To my mentor Shawn Fitzgerald, thank you for your support and advice over all of the years, and the beer brewing sessions. I would also like to thank my brothers Daniel and Aaron for pretending to listen to me when I get excited about my research, well for a few seconds anyway.

I would like to thank the Advanced Steel Product and Processing Research Center for providing me with the opportunity to continue my education. I thank my advisor Dr. Matlock for his insight and support on this project. I would also like to thank Dr. De Moor and Dr. Findley for their assistance throughout my time here at Colorado School of Mines. Elaine Sutton is also owed a large debt of gratitude, for if it were not for her constant efforts no work would be accomplished within the steel center.

Thank you to my colleagues in the Steel Center for sharing your knowledge when necessary, and I would like to specifically thank Julian Stock, Paul Gibbs, Caryn Homsher, Patrick Kramer, Stephanie Miller, and Shane Kennett. I also would like to thank my fellow metallurgy students Steven Klimowicz, Cody Miller, and Matthew Hayne for any insight, distractions, or otherwise that you may have provided.

CHAPTER 1

INTRODUCTION

Fatigue is a common failure mechanism resulting from a varying stress state with a tensile component that is less than the tensile strength of the material. In a part such as a crankshaft that experiences such cyclic loading in service this can be a problem. This problem is exacerbated by the presence of fillets in the part design that will serve to concentrate stress leading to a reduction in its resistance to fatigue failure. Deep rolling is a process in which the surface of a notched part is plastically deformed creating a work hardened surface layer and compressive residual stress at the surface. This effect increases the fatigue performance of a part as evaluated through the endurance limit versus the unrolled condition.

In the present work further improvement from deep rolling is sought through the use of strain aging and dynamic strain aging. Strain aging is achieved when interstitial atoms such as carbon or nitrogen are present in solution, and are able to diffuse to and pin dislocations. Two steels with different amounts of solute nitrogen were used in this study to achieve different aging responses especially at lower temperatures between 100 °C and 200 °C. The different amounts of solute nitrogen were achieved by not only varying the amount of nitrogen in the composition but also by changing the amount of nitride formers such as titanium, aluminum, and vanadium.

A strain aging study and elevated temperature mechanical testing were used to evaluate the strain aging responses of the two materials used. Based upon these strain aging responses the temperature was chosen to age deep rolled samples at for static strain aging and the elevated temperature at which to deep roll at was selected such that strain aging would be active in one material and not the other. Fatigue responses of the two materials were evaluated using fully reversed cantilever beam load control fatigue testing.

CHAPTER 2

BACKGROUND

2.1 Fatigue

Fatigue is considered to be one of the most serious types of failures because it can happen under normal operating conditions without the existence of extreme loads [11]. Fatigue is defined as the "phenomenon leading to fracture or cracking under fluctuating stresses having a maximum value less than the ultimate tensile strength of the material [12]." There are three stages in fatigue crack growth: initiation, propagation, and final rupture [11]. A parameter useful for describing fatigue crack behavior is ΔK and is defined in Equation 2.1. In Equation 2.1 σ_{max} and σ_{min} are the maximum and minimum applied stresses (σ_{min} is taken to be 0 if loading goes compressive) and a is the crack length [1, 13]. Equation 2.1 is a simplified presentation of the fracture mechanics to predict fatigue crack growth.

$$\Delta K = K_{max} - K_{min} = \sigma_{max}\sqrt{\pi a} - \sigma_{min}\sqrt{\pi a} \quad (2.1)$$

The initiation stage involves very small microstructural changes that occur due to shear stresses and damage is accumulated over a very large number of cycles. Fatigue crack initiation generally occurs at free surfaces because stresses at surfaces are higher and imperfections on the surface can act as stress risers for initiation points [12]. This stage has been studied extensively because if fatigue crack initiation can be prevented then fatigue failure will not occur [11]. There is a threshold stress intensity value, ΔK_{th} , below which there is no measurable fatigue crack propagation or growth so at this low applied stress value fatigue failure will not occur [1]. The crack propagation stage in fatigue occurs perpendicular to the maximum tensile stress. The growth rate of a crack in this stage of fatigue can be defined as da/dN , the change in crack length per loading cycle, in Equation 2.2, where a is crack length and N is the number of cycles.

$$\frac{da}{dN} = A(\Delta K)^p \quad (2.2)$$

The values of A and p are empirical fit parameters. The third stage of fatigue is final rupture. As the fatigue crack propagates in the second stage the load bearing area of the part is slowly being reduced. At a certain point the applied load will exceed the strength of the material giving rise to the final rupture [11].

There are two basic ways to improve the fatigue performance of a part, increase the strength or decrease the applied stress [11]. To increase the strength of the part different materials could be used or higher quality materials with fewer inclusions that may act as nucleations sites. A decrease in stress can be achieved through a redesign of parts, larger cross sections, larger fillet radii, etc. One method to improve the fatigue performance of a part that fits into both strengthening the part and decreasing the applied stress is to induce a compressive residual stress into the surface [11]. Introducing compressive stresses into the surface can be accomplished through thermochemical means such as carburizing, phase transformations through heat treating, or prestressing the surface among others. Prestressing the surface gives rise to tensile yielding at the surface, and when the prestress is removed a surface compressive residual stress remains at the surface, which has to be balanced by tensile stresses below the surface [11]. The effect of residual stresses on the overall stress state is illustrated in Figure 2.1. This residual stress profile effectively reduces the

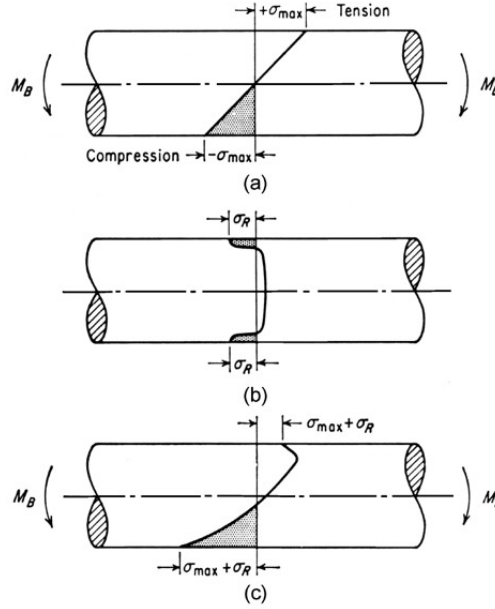


Figure 2.1 (a) shows the applied stress in a bending bar with no residual stresses present, (b) shows the residual stress profile typical of a shot peened part, and (c) shows the two stress profiles superimposed on one another [1]. Notice that the maximum tensile stress at the surface is reduced by the residual stress profile.

applied stress at the surface of the part, and can in fact lead to subsurface fatigue crack initiation depending on material strength and loading conditions.

2.2 Strain Aging

Strain aging is a phenomenon that occurs after a metal has been cold worked and heated to a relatively low temperature and an increase in flow stress as well as the return of a yield point is observed when reloaded [1, 14]. A schematic of this process is shown in Figure 2.2. In this schematic a sample is loaded to point X and immediately reloaded with no intermediate heating step, and the flow curve returns to point X upon reloading. At point Y the sample is unloaded again and there is an intermediate heating step before reloading the sample. After this heating step there is an increase in the flow stress as well as a return of the yield point observed. The kinetics of this process are controlled by long range diffusion of solute atoms to the strain fields produced by dislocations [15].

The initial stages of aging are described by the Cottrell-Bilby theory of strain aging based on the stress fields produced by dislocations and solute atoms interacting with one another. In order to relieve these strains in the lattice solute atoms will diffuse to dislocations [1, 14, 16]. It is most simple to consider the interaction of a substitutional solute atom with a positive edge dislocation, due to the fact that hydrostatic stresses produced by an edge dislocation can be relieved by a substitutional solute (unlike a pure screw dislocation which only produces shear stresses [14]) [16]. A substitutional atom has an interaction energy with a positive edge dislocation given by Equation 2.3.

$$V = \frac{4}{3} G \epsilon r_a^3 \lambda \frac{1 + \nu \sin \alpha}{1 - \nu} \frac{1}{r} \quad (2.3)$$

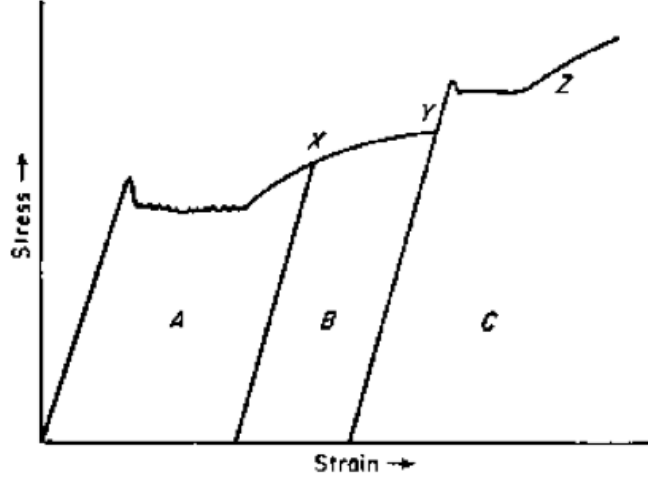


Figure 2.2 A schematic diagram showing the basic strain aging behavior of a low carbon steel. If a steel sample is loaded in tension to point X along the curve and unloaded (region A), then loaded again in tension immediately with no time to age it returns to point X with no discontinuous yielding. If a sample is loaded in tension to point Y and unloaded (region B) and aged before being reloaded in tension an increase in flow stress and a return of discontinuous yielding is seen in region C [1].

In Equation 2.3 r and α are the coordinates of the solute atom in relation to the dislocation (r is the radius and α is the angle measured from the slip direction), G is the rigidity modulus, ν is Poisson's ratio, λ is the slip distance in the dislocation, r_a is the solvent atomic radius, and $r_a(1 + \epsilon)$ is the atomic radius of the solvent. However, interstitial atoms such as N and C are able to interact with screw dislocations and edge dislocations because they do not uniformly distort the lattice like a substitutional atom. This non-uniform deformation of the lattice creates shear strains which allow the strain fields of the interstitial solutes to interact with the strain fields of screw dislocations [16]. Cottrell and Bilby [14–16] also stated that the number of atoms per unit length of dislocation in a dilute solution will be given by Equation 2.4.

$$n_t = n_0^3 \left(\frac{\pi}{2} \right)^{\frac{1}{3}} \left(\frac{ADt}{kT} \right)^{\frac{2}{3}} \quad (2.4)$$

In Equation 2.4 n_0 is the average number of solute atoms per unit volume, A is the interaction energy between a dislocation and solute atom, D is the diffusion coefficient of the solute atom, k is Boltzmann's constant, and T is temperature. This expression is only useful for the early stages of aging as it does not account for the depletion of solute atoms from the matrix near dislocations as well as saturation of the strain field near the dislocation by solute atoms. In order to apply Equation 2.4 to supersaturated solutions and to account for solute depletion near dislocations, Harper assumed that the amount of segregation would be proportional to the solute concentration remaining in the matrix and is given in Equation 2.5, where L is the dislocation line length per unit volume [15].

$$W = \left(\frac{n_t}{n_0} \right) = 1 - \exp \left[-3L \left(\frac{\pi}{2} \right)^{\frac{1}{3}} \left(\frac{ADt}{kT} \right)^{\frac{2}{3}} \right] \quad (2.5)$$

From Equation 2.5 it can be seen that the number of atoms at a dislocation after time t is dependent upon temperature as well as the diffusion coefficient D of the solute atom through the matrix. Only a small amount

of interstitial carbon or nitrogen is needed to provide atmospheres for all dislocations in the matrix, but the required amount depends on the dislocation density in the matrix. If it is assumed that one interstitial atom is needed per plane threaded by a dislocation to lock a dislocation, the amount of C (or N) needed to lock all dislocations is given by Equation 2.6 where ρ is the dislocation density given in m^{-2} [15].

$$[C]_{ppm} = 8.9 \times 10^{-15} \rho \quad (2.6)$$

If a relatively high dislocation density of $10^{14}/m^{-2}$ is substituted into Equation 2.6 only about 1 ppm of C or N is needed to lock all the dislocations.

Static strain aging can be quantified with measurements of the change in flow strength after aging. This is shown schematically in Figure 2.3. The parameter ΔY is measured as the difference between the flow stress at the end of prestraining and the yield stress after aging. The value of ΔY will be dependent upon the amount of prestrain, aging temperature, and aging time.

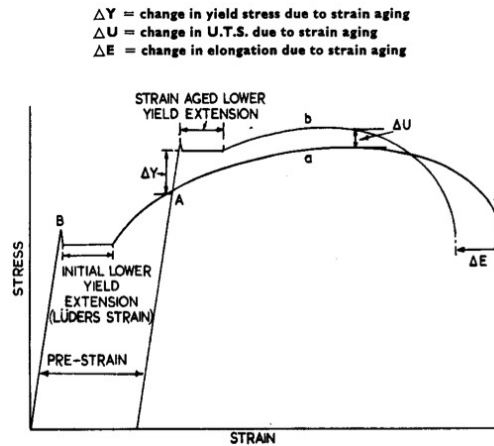


Figure 2.3 Stress strain curve from Baird [2] for a low carbon steel that is restrained to point A then unloaded and aged (curve b). This gives rise to a change in the flow stress shown as ΔY in this figure. This ΔY parameter can be used to quantify the strain aging response of a material at a given temperature and aging time. Curve a shows a sample that is loaded to point A then unloaded and loaded again immediately with no aging.

In order to control strain aging due to C or N, microalloying elements can be added [3, 17–19]. By adding microalloying elements such as vanadium (V), titanium (Ti), aluminum (Al), and niobium (Nb) interstitial C and N are combined with these elements to form carbides and nitrides [20]. By taking C and N out of solid solution and creating carbides and nitrides strain aging can be reduced or eliminated as only solute atoms in solid solution can contribute to strain aging. However, as presented earlier as little as 1 ppm N or C can cause significant strain aging [18]. N can also interact with manganese (Mn), but this interaction does not eliminate strain aging. N prefers interstitial sites near Mn atoms and forms Mn-N pairs [3, 4, 21]. The formation of these Mn-N pairs shifts the temperatures higher and times longer for N strain aging as Mn-N pairings slow the diffusion of N.

N behaves similarly to C in strain aging as it is also an interstitial atom that is similarly sized (radius of C=0.077 nm and N=0.071 nm [22]) and both occupy the octahedral interstitial site in α Fe [3]. N has a potential to contribute more to strain aging than C because of its higher solubility in α Fe. C has a

maximum solubility at 727 °C of 0.0218 wt pct and N has a maximum solubility of 0.093 wt pct at 585 °C [23]. At room temperature the solubilities of these interstitial atoms are lower, approximately 10^{-7} wt pct for C and 10^{-5} wt pct for N, but the solubility of N is still approximately 100 times greater than that of C. This additional solubility of N compared to C increases the value of n_0 from Equation 2.4 meaning that the strain aging response should be intensified due to N [4]. In addition to the increased solubility of N in α Fe, N has a higher diffusion coefficient with a lower activation energy than C. The diffusion coefficients of C and N in α Fe are:

$$D_C = 0.02 \exp \left[-\frac{88280}{RT} \right] \text{ cm}^2/\text{s} \quad (2.7)$$

$$D_N = 6.6 \times 10^{-3} \exp \left[-\frac{77820}{RT} \right] \text{ cm}^2/\text{s} \quad (2.8)$$

where $R = 8.314 \frac{\text{J}}{\text{molK}}$. The lower activation energy associated with the diffusion of N means that strain aging associated with N can occur at lower temperatures than C, and any aging that occurs below 100 °C is attributed to solute N [2, 3].

Dynamic strain aging (DSA) is a process where aging occurs concurrently with deformation. A serrated stress strain curve is usually observed with DSA, and is associated with the Portevin-Le Châtelier (PLC) effect [1, 14]. During deformation when the stress becomes high enough for the dislocations to break away from the solute atmospheres there is a load drop. At elevated temperature the solute atoms are mobile enough to catch and pin the dislocations again, which results in an increase load. This process is repeated several times giving rise to the serrated appearance of the stress strain curve at temperatures at which DSA occurs. A serrated stress strain curve is not the only way that DSA is manifested, in fact DSA can happen and serrations will not appear in the stress strain curve in some instances [18]. Other ways that DSA is manifested is an increase in flow stress and work hardening rate, as well as a loss of ductility. Figure 2.4 shows how varying N content can affect the amount of serrated yielding as well as how flow stress can vary with the amount of N in a steel [3]. In Figure 2.4a some serrated yielding can be seen in the 204 °C curves and the 260 °C curves. In a 1020 steel with higher N content such as that in Figure 2.4b more serrated yielding as well as an increase in flow strength in the temperature range from 204 °C to 316 °C can be seen showing that more DSA occurs at higher levels of N. Figure 2.5 also shows that with increasing N content a higher work hardening rate is observed at elevated temperatures [3]. The steel with the highest level of N has a spike in the work hardening rate in the temperature range of 204 °C to 316 °C showing that this is the temperature range in which DSA is active in this material.

The Mn content along with the N content can affect the strain aging response of steel. The formation of the Mn-N pairs slows the diffusion of N thus decreasing the strain aging response, as illustrated in Figure 2.6 which shows the effect of nitrogen content on strain aging index ($\Delta\sigma$ is the difference in stress between end of prestraining and reloading after aging) for a low carbon steel with three different Mn contents. In Figure 2.6 the strain aging index is defined as the change in flow stress after strain aging. For a given N content with increasing Mn content the strain aging index decreases, showing that strain aging is not as prominent with the addition of Mn. Figure 2.7 shows the effect of Mn and N content on the flow stress of a 0.1% C steel at various temperatures on the 10% strain flow stress. With 0% N the flow stress decreases with increasing temperature as expected. With the addition of 0.01% N there is an increase in flow stress at approximately 150 °C then a decrease at 400 °C. The region where there is an increase in strength is the

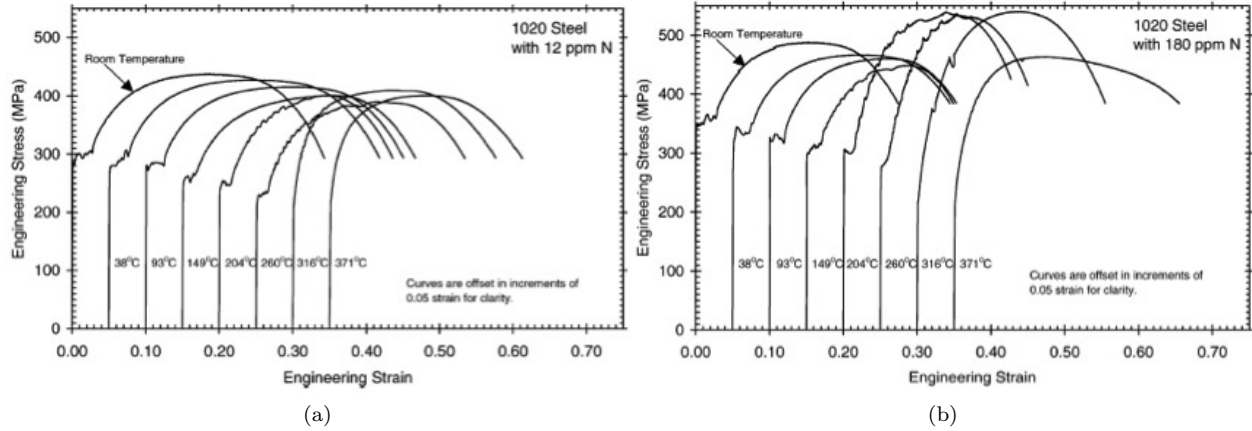


Figure 2.4 Engineering stress versus strain plots of two 1020 steels with different nitrogen contents [3]. The 1020 steel in (a) contains only 12 ppm N and even with this low amount DSA is observed at elevated temperatures. The 1020 has 180 ppm nitrogen and the serrated flow and flow stress is much higher in the 200 °C to 316 °C region due to the higher interstitial content.

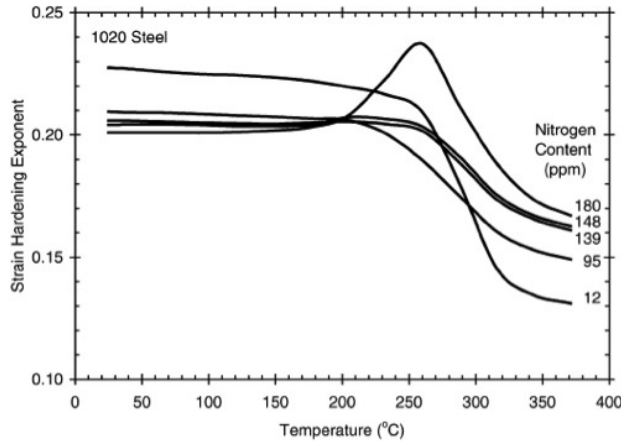


Figure 2.5 A plot of the strain hardening exponent versus temperature of a 1020 steel with different amounts of nitrogen [3]. The steel with the largest peak in strain hardening exponent is the one with the highest nitrogen content.

region in which DSA is active. A higher Mn content leads to a greater increase in flow stress as a result of more substitutional atoms being present as a part of the Mn-N pairs.

2.3 Bauschinger Effect

The Bauschinger effect, first observed by Bauschinger in 1881 [24], is characterized by a decrease in yield strength in a material when the strain direction is reversed after being plastically deformed in the opposite direction [1, 5, 25–29]. The magnitude of this yield drop can be more than a 50 pct reduction in some cases [25]. There are two accepted mechanisms that contribute to the Bauschinger effect. One being long-range back stresses generated during plastic prestrain that can assist dislocation motion upon strain reversal [1, 26–28]. These long-range back stresses are a result of dislocations interacting with and piling up at grain boundaries and at Orowan loops around hard particles in the microstructure. These back stresses are

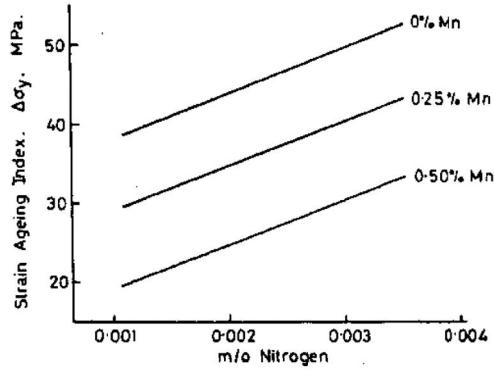


Figure 2.6 A plot of strain aging index versus wt pct N with different amounts of Mn. As the amount of Mn increases the strain aging index is decreased [4].

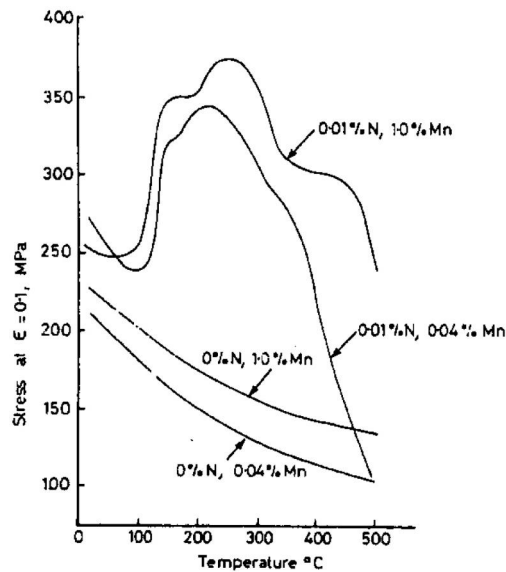


Figure 2.7 A plot of flow stress at 10% strain versus temperature of a 0.1 wt pct C steel with different amounts of N and Mn. In the curves with no N the flow stress decreases with increasing temperature. When N is present there is an increase in flow stress with temperature to a peak at approximately 250 °C which is indicative of DSA occurring [4].

more prominent in dual phase materials; thus, dual phase materials typically exhibit a larger Bauschinger effect than single phase materials. These long range stresses also only initially aid in the reversal of the motion of dislocations. As straining is continued in the opposite direction these back stresses will eventually be reversed [30]. The second mechanism is short-range effects related to a reduced resistance to motion in the reverse direction in which dislocations were generated [1, 26–28]. One way to describe this anisotropy in direction of dislocation motion is presented by Sleswyk and Kemerink [31]. They state that when the stress is reversed, dislocations that have been held up by barriers are free to move over free paths in reverse until again being held up by a new barrier. Another short range mechanism proposed is the fact that when stress is reversed dislocations of opposite sign are produced from the original source and dislocations of opposite sign attract and annihilate each other [32].

Several methods have been used to quantify the Bauschinger effect [5, 29] including:

1. The Bauschinger Strain β , defined as the strain required to reach the same stress as achieved in the preload.
2. The Bauschinger Strain Parameter (β_ϵ) is the Bauschinger strain divided by the plastic prestrain (ϵ_p).

$$\beta_\epsilon = \frac{\beta}{\epsilon_p} \quad (2.9)$$

3. The Bauschinger Effect Factor, where σ_{ft} is the stress at 3 pct strain in tension and σ_{yc} is the 0.2 pct offset yield strain calculated after the stress reversal.

$$BEF = \frac{\sigma_{yc}}{\sigma_{ft}} \quad (2.10)$$

4. The Bauschinger Energy Parameter, where E_P is the area under the tensile stress strain curve and E_S is the area above the compressive curve and under the Bauschinger strain load.

$$BEP = \frac{E_S}{E_P} \quad (2.11)$$

An illustration of how these parameters are measured is shown in Figure 2.8.

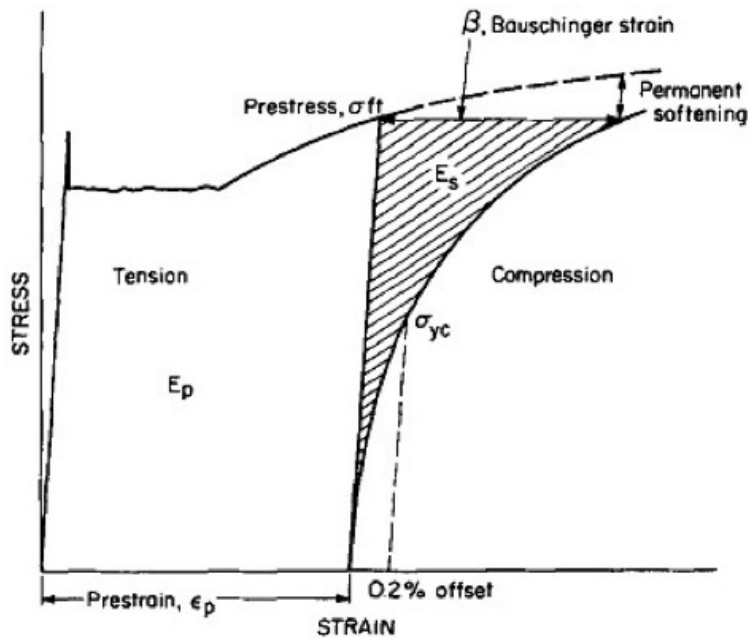


Figure 2.8 A schematic of a metal loaded in tension then compression from *Liet al.* illustrating the Bauschinger effect and showing the various parameters used to quantify the effect [5]. Both the tensile and compressive portions of the stress strain curve have been plotted in the tensile portion of the plot to simplify presentation. A clear drop in the yield stress is seen in the compressive part of the curve as well as permanent softening. Had the loading history been reversed (loaded in compression then tension) the curves would look the same.

2.3.1 Minimizing the Bauschinger Effect

Methods that have been explored to reduce the Bauschinger effect are heat treatment [27], strain aging [25, 26], and dynamic strain aging [5, 26, 28]. Aran [27] investigated the effect of increasing heat treatment temperatures after prestraining in tension then reloading in compression. With increasing heat treatment temperature the Bauschinger effect was reduced. In the temperature regime in which recrystallization occurs new strain free grains appeared thus eliminating dislocations and back stresses present in the microstructure, leading to the Bauschinger effect being almost completely eliminated [27]. At temperatures lower than the recrystallization temperature but high enough for strain aging to occur, a decrease in the Bauschinger effect is also seen [25, 27]. In the strain aging temperature regime, solute interstitial atoms such as carbon (C) and nitrogen (N) are able to move to the dislocations and pin them, thus increasing the stress required to move them in the reverse direction. The use of strain aging also leads to a return in the yield point in the reverse direction [25]. In order for dynamic strain aging to be active, the material must be deformed at elevated temperature during the prestraining step. By deforming materials at an elevated temperature, C and N are able to diffuse during the deformation process leading to a significant reduction in the Bauschinger effect upon strain reversal [5, 26]. This reduction has been attributed to the production of a more stable dislocation structure [26] and to the reduction of back stresses and pinning of mobile dislocations [5]. Okamoto [33] studied the deformation behavior of low carbon martensite, and found at a temperature and strain rate combination where serrated yielding took place there was an absence of dislocation cell formation. The dislocation structure that existed consisted of linear arrays of screw dislocations with irregularly shaped tangles. Concurrent with deformation, C atoms diffused to screw dislocations and pinned them reducing their ability to cross slip, so new dislocations were generated to sustain deformation [34]. Development of an array of relatively immobile screw dislocations may be responsible for the reduction of the Bauschinger effect due to dynamic strain aging.

2.4 Deep Rolling

Deep rolling is a surface mechanical treatment that is used to improve the fatigue performance of rotationally symmetric notched parts such as crankshaft crankpins and axle journals [6, 7, 35, 36]. Deep rolling is usually applied to the fillets in a crankshaft because the fillets are one of the most highly stressed areas of a crankshaft [37, 38]. Deep rolling, like other surface mechanical treatments such as shot peening, creates a work hardened layer through cold working the surface, induces a residual compressive stress in the surface, and additionally can improve the surface finish of the part [6, 7, 35, 39, 40]. An advantage of deep rolling compared to other purely mechanical surface treatments is the depth of the cold worked region and residual stresses. A schematic of typical "case" depths of various thermochemical, thermal, and mechanical surface treatments from Altenberger [6] is shown in Figure 2.9. It is generally accepted that the most beneficial effect of deep rolling on the improvement in fatigue performance of a part is the introduction of the surface compressive residual stresses.

In a deep rolling process, load rollers are pressed into the surface of a part under a controlled load [8]. There are several variables that make up the deep rolling process. Figure 2.10 illustrates some of these variables. The geometry of the rollers and the part will influence the contact area thus ultimately the contact stress. The materials from which the part and roller are made also influence the deep rolling process. The number of overrolls (the number of times a point on the surface of the part comes into contact with

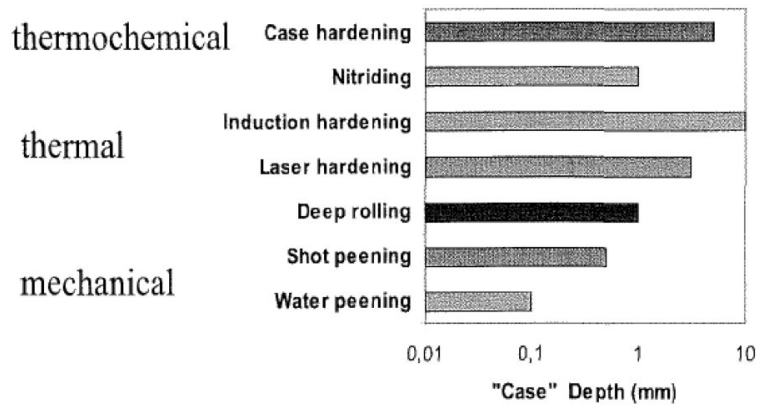


Figure 2.9 Schematic showing typical case depths of various surface treatments. Deep rolling shows the greatest case depth of the purely mechanical treatments [6].

a load roller) and the applied rolling force are important to the development of the the work hardened surface and the surface residual stresses. Parameters that are generally easily changed are the material used to manufacture the part, the number of overrollings, and the applied load through the load rollers to the surface of the part. In order to evaluate the fatigue performance and simulate loading conditions similar to that of the root of a fillet in a crankshaft fully reversed bending fatigue testing can be used [8, 36, 38].

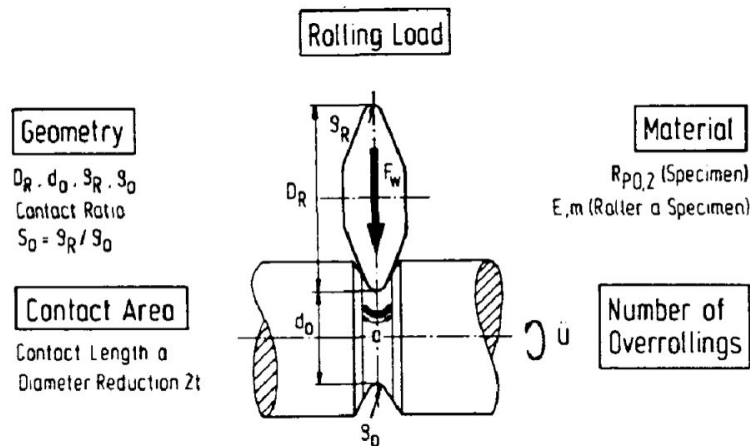


Figure 2.10 Diagram from Kloos et al. [7] showing parameters necessary to define a deep rolling process.

Deep rolling can significantly increase the fatigue performance of notched parts. It is not uncommon to gain up to a 50% increase in endurance limit from deep rolling. It has been observed that it is possible to obtain superior fatigue performance from a deep rolled notched part than a smooth part that has been deep rolled [7]. Richards [8] evaluated the effects of deep rolling on three steels with different microstructures (ferrite-pearlite, bainitic, and quenched and tempered martensite) and compositions and all had a 50% to 60% increase in endurance limit when deep rolled. For example, Figure 2.11 shows the S-N curves for the C38M material used in Richards' study with the baseline and deep rolled conditions tested.

The mechanism by which the endurance limit is improved may be by delaying or even completely arresting the second stage of fatigue, *i.e.* crack propagation. Evidence of this crack arrest was found by Richards in the form of non propagating fatigue cracks in deep rolled samples tested at their endurance

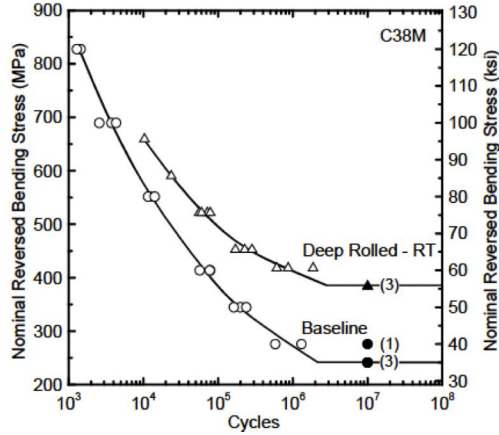


Figure 2.11 S-N curves for the baseline and deep rolled conditions for C38M (a sulfur modified and microalloyed 1038 ferrite pearlite steel). A baseline endurance limit of 241MPa (35 ksi) is observed with a deep rolled endurance limit of 386 MPa (56 ksi). This represents a 60% increase in endurance limit in the deep rolled conditioned versus the baseline condition [8].

limit [8]. It has been suggested that although the crack free life of a part is not greatly improved by deep rolling the fact that crack arrest can occur greatly improves the lifetime to rupture [6, 7, 35, 38, 41]. Crack arrest occurs when the applied stress superimposed with the residual compressive stress becomes less than the stress to propagate the crack. An illustration of this from Altenberger [6] is shown in Figure 2.12. This figure shows the effect of the residual stress on the effective applied stress is to slow or even completely arrests the crack depending on the applied load and residual compressive stresses present.

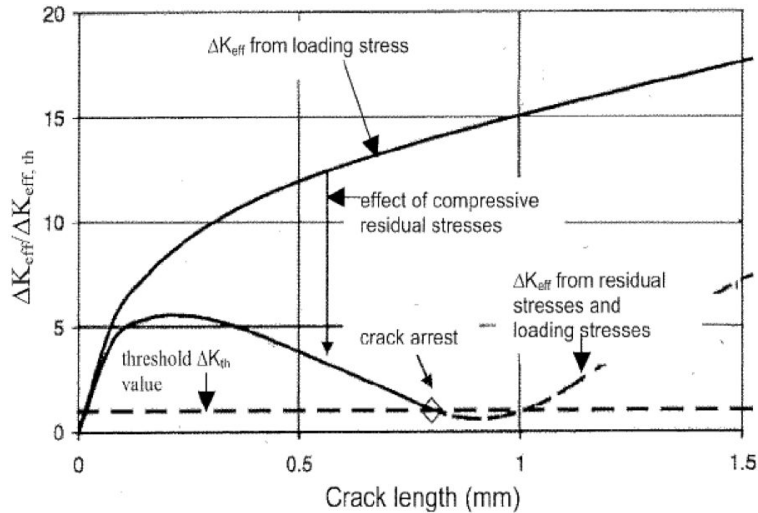


Figure 2.12 Effect of residual stresses on the crack propagation behavior of a AISI 4140 steel. The vertical axis is the value of ΔK as a function of crack length with a dashed line at the value of ΔK_{th} and the horizontal axis is the crack depth with 0 being the surface. The compressive residual stresses decrease the effective applied stress to slow or even completely arrest the crack [6].

As stated earlier the compressive residual stresses contribute most to increased fatigue performance resulting from the deep rolling process. Therefore it is important to consider the stability of these residual stresses during cyclic loading. In the first half cycle it is possible that the superimposed residual stresses

and applied stress can exceed the yield stress of the material [38]. If the yield stress is exceeded in the compressive direction at the surface, the residual stresses can become tensile as a result of this plastic flow, leaving the surface unprotected from crack initiation. Tensile loading will also relax residual stresses due to plastic flow, but a complete relaxation of compressive residual stresses is not observed due to tensile loading [42]. The Bauschinger effect lowers the tensile yield strength of deep rolled components; deep rolling is a compressive prestrain, making materials more susceptible to stress relaxation through plastic flow [43].

2.4.1 Elevated Temperature Rolling

Further improvement over room temperature deep rolling is observed when specimens are deep rolled at elevated temperatures. Figure 2.13 illustrates this improvement in the C38M alloy presented earlier [8]. The RT S-N curve represents the deep rolling process at room temperature under an applied load of 10.5 kN (2,360 lbf) and the HT curve represents the deep rolling process carried out at 260 °C under an applied rolling load of 15 kN (3,370 lbf). In this study conducted by Richards [8] samples were also aged after deep rolling at room temperature, but did not give rise to as great an increase in fatigue performance as deep rolling at elevated temperatures. The improvement in fatigue performance seen from deep rolling (or shot peening) at elevated temperatures has been attributed to dynamic strain aging being active [6, 39, 43, 44]. As discussed in Section 2.3.1 dynamic strain aging is capable of reducing the Bauschinger effect. By reducing the Bauschinger effect residual stresses become more stable as the tensile yield strength is increased after deep rolling making the material less susceptible to plastic flow leading to relaxation of residual stresses. Dynamic strain aging leads to a greater improvement in fatigue performance over static strain aging because it produces a more stable and diffuse dislocation structure [44].

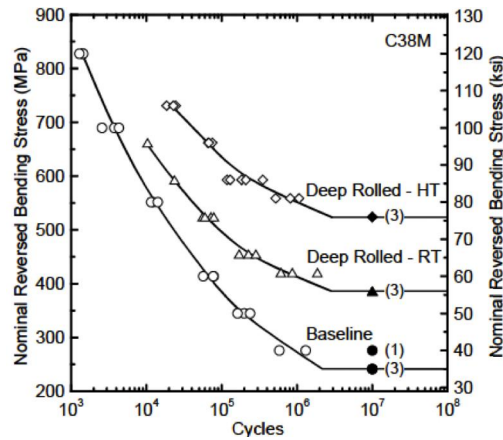


Figure 2.13 S-N curves for the baseline, room temperature rolled (RT), and elevated temperature rolled (HT) C38M from Richards [8]. The baseline endurance limit is 241 MPa (35 ksi), RT endurance limit is 386 MPa (56 ksi), and the HT endurance limit is 524 MPa (76 ksi). The HT endurance limit is a 36% improvement over RT and a 117% increase over the baseline condition.

CHAPTER 3

EXPERIMENTAL METHODS

3.1 Materials Selection

The specific focus of this study was to further evaluate the application of elevated temperature rolling and post rolling aging to enhance the fatigue performance of deep rolled steels through strain aging and dynamic strain aging. The steels selected for this study were two ferrite-pearlite steels, C38M and C38N2 both provided by The Timken Company. The compositions of the two materials are listed in Table 3.1. The main difference between the two alloys is the content of microalloying. The C38N2 material contains lower amounts of nitride forming elements such as titanium (Ti), vanadium (V), and aluminum (Al). The lower content of these elements in the C38N2 alloy compared to the C38M material results in a higher interstitial nitrogen (N) content in the C38N2 material. This difference in interstitial N between the two alloys was desired because of the different aging responses the two materials would have. Both materials were supplied as hot rolled and air cooled bars, the C38M was provided as 7.62 cm (3 in.) diameter bar and the C38N2 material was provided as 10.8 cm (4.25 in.) diameter bar. Figure 3.1 illustrates an axial view of where mechanical test samples were machined out of the as received bars. The samples were machined out of a radius 2.22 cm (0.875 in) from the center in the case of C38M and 3.5 cm (1.375 in) from the center of the case of C38N2. This was done in order to avoid any center line segregation that still may have existed after the rolling process.

Table 3.1 – Compositions of Steels Used in Deep Rolling Project (wt pct)

Alloy	C	Mn	Si	Ni	Cr	Mo	Ti	Nb	V	Al	N	S
C38M	0.38	1.38	0.55	0.08	0.13	0.02	0.010	-	0.09	0.020	0.0138	0.057
C38N2	0.37	1.34	0.52	0.08	0.13	0.03	0.002	0.001	0.002	0.016	0.017	0.056

3.2 Metallography

Upon receipt of the material, metallographic coupons were taken from the same location in the bars as the mechanical test specimens (shown in Figure 3.1) for microstructural evaluation. Samples were polished to a 1 μm finish before being etched in a 4% nital solution to reveal the microstructural features. The fractions of pearlite and ferrite present in the microstructures were determined using the point counting method according to ASTM E 562 [45] with a circular grid. The phase present at each grid point was determined and volume fractions of pearlite, f_p , and ferrite, f_f , were calculated based on these point counts. Grain size was determined using the linear intercept method for duplex microstructures [46]. Three concentric circles of known length, L , were overlaid on several micrographs and the number of ferrite-pearlite, n_p , and ferrite-ferrite, n_α , boundaries along the length of the circles were counted in each micrograph. The average size of the pearlite colonies, d_p , and ferrite grains, d_f , could then be calculated according to Equations 3.1 and 3.2. The standard error in the measurements was calculated as the standard deviation, s , divided by the population size, N , giving standard error to be equal to $\frac{s}{\sqrt{N}}$.

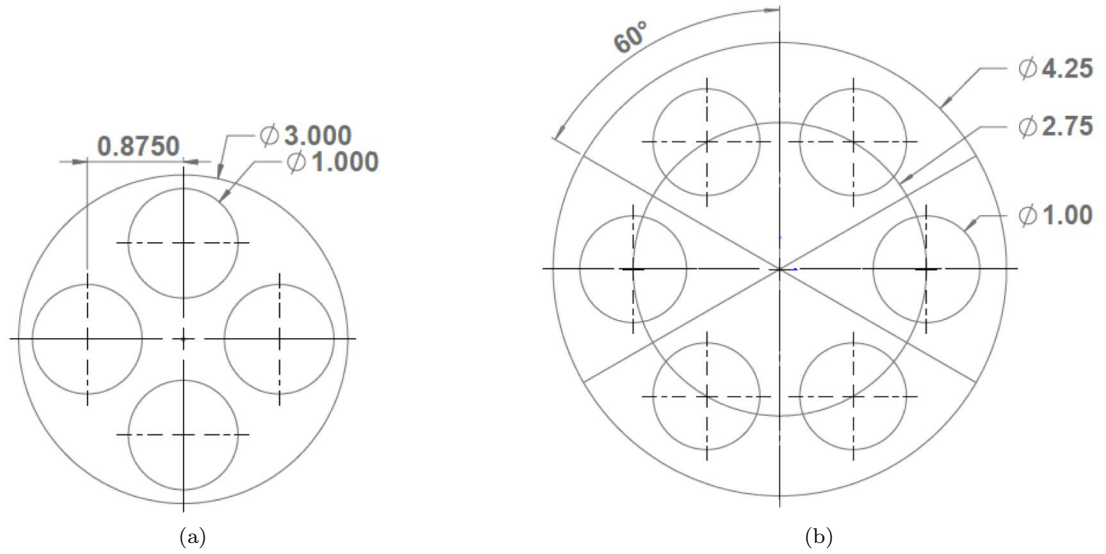


Figure 3.1 An axial view of where deep roll samples (Figure 3.7) were machined out of the as received bars. All mechanical test samples were machined from the same radius as the deep roll samples. C38M was received in 7.62 cm (3 in) bars (a) and C38N2 was received as 10.8 cm (4.25 in) bars (b). (All units are shown in inches)

$$d_p = \frac{f_p L}{\frac{1}{2}n_p} \quad (3.1)$$

$$d_f = \frac{f_f L}{n_\alpha + \frac{1}{2}n_p} \quad (3.2)$$

3.3 Mechanical Testing

Various mechanical testing was performed to evaluate the initial mechanical properties of the as received materials as well as to evaluate the strain aging and dynamic strain aging responses of the two materials.

3.3.1 Tensile Testing

Room temperature tensile tests were conducted using an MTS electro-mechanical test frame with a load limit of 89 kN (20,000 lbf). The sample geometry used is shown in Figure 3.2. A 25.4 mm (1 in) Shepic \pm 50% extensometer was used to measure strain during the tensile tests. A constant engineering strain rate of $1.6 \times 10^{-3} \text{ s}^{-1}$ was used for all tensile tests. The yield strengths of the two materials were calculated using the 0.2% offset method and the ultimate tensile strengths were also calculated from room temperature tensile tests according to ASTM E8 [47].

3.3.2 Strain Aging

A strain aging study was conducted in order to determine the strain aging responses of the two materials used in this study. Samples pre strained to 2.5% using the same parameters and sample geometry as used

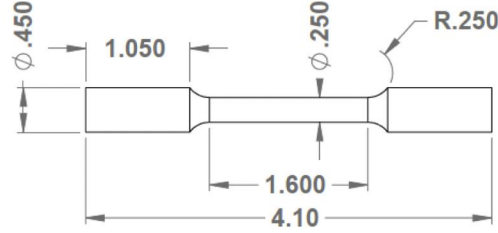


Figure 3.2 Tensile test sample geometry used for room temperature temperature tests and the strain aging study, all units are in inches.

for the room temperature tensile testing. The materials were then aged for 35 minutes at temperatures ranging from 100 °C to 260 °C. For temperatures up to 150 °C, an oil bath of Paratherm was used and for temperatures above 150 °C, molten salt baths were used. After aging the tensile samples for 35 minutes, they were water quenched to room temperature before being tested in tension to failure.

To evaluate the strain aging response a parameter to quantify the strength change as a result of strain aging the aging index, $\Delta\sigma$, was used. The value of $\Delta\sigma$ was calculated by subtracting the maximum value of the flow stress during prestraining from the yield stress of the material after aging for 35 minutes at a given temperature. A typical strain aging test from this study is shown in Figure 3.3.

3.3.3 Bauschinger Effect Testing

Bauschinger effect testing and low cycle fatigue testing were performed on a 445 kN (100 kip) servo-hydraulic frame with a woodsmetal alignable grip at CSM. The Bauschinger effect testing sample was previously developed by Richards [8] and is shown in Figure 3.4. A 12.7 mm (0.5 in) \pm 15% shepic extensometer was used to measure strain as well as control the actuator motion of the servo-hydraulic frame. The samples were deformed in tension to 3% strain before the stress was reversed and the samples were then compressed to minus 3%. A constant engineering strain rate of 10^{-3} s^{-1} was used for all Bauschinger effect testing. In order to evaluate the Bauschinger effect, the Bauschinger effect factor (BEF) was used as described in Section 2.3. A typical test is shown in Figure 3.5.

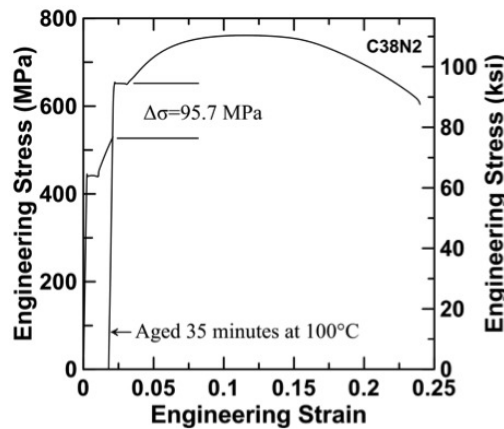


Figure 3.3 A graphical representation of the calculation of $\Delta\sigma$ from strain aging curves of C38N2 aged at 100 °C for 35 minutes

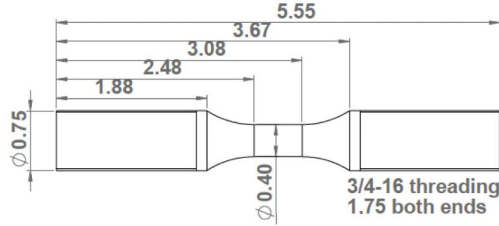


Figure 3.4 Bauschinger effect test sample as developed by Richards [8] according to ASTM E 606-4 low cycle fatigue specimen guide [9]. All dimensions are in inches.

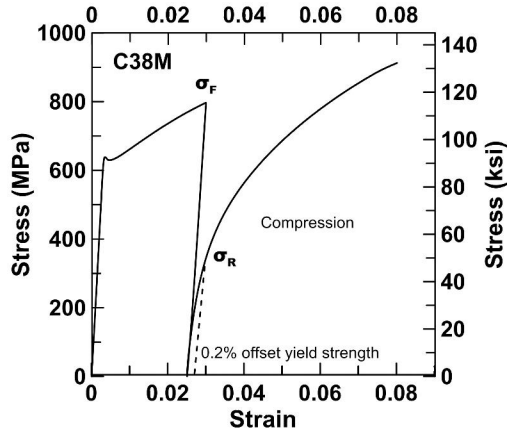


Figure 3.5 A typical Bauschinger effect test conducted in this study of the C38M material conducted at room temperature. The compressive portion of the test is also shown in the tensile region of the graph for ease of representation.

Bauschinger effect testing was also conducted at elevated temperatures using two Spot IR heat lamps as the heat source. In order to more efficiently heat the samples in the grips a matte black high temperature spray paint was applied to the surface of the samples. A K-type thermocouple was spot welded to the surface of the samples to monitor temperature and for use with an OMEGA cn79000 PID controller attached to the heat lamps for temperature control. A view of the sample in the grips of the frame with the heat lamps in place can be seen in Figure 3.6. In order to evaluate the temperature range at which dynamic strain aging was most active in each material, the BEF versus temperature over the test temperature range of 100 °C to 300 °C was plotted as well as flow stresses at yielding, 1% plastic strain, and 2% plastic strain. Dynamic strain aging will reduce the BEF and increase the flow stress at increasing temperature when it is expected that flow stress would decrease at increasing temperature [48]. The temperature at which dynamic strain aging was determined to be most active in the C38N2 material but not in the C38M was identified and used for elevated temperature deep rolling.

3.4 Fatigue Testing

All fatigue testing was performed using Baldwin SF-1-U load controlled universal fatigue machines with a load limit of 4448 N (1000 lbf) operating at a rate of 30 Hz. Fatigue tests were performed in fully reversed cantilever bending ($R = -1$). The sample geometry used (illustrated in Figure 3.7) was the same used for the deep rolling project previously conducted at Colorado School of Mines by Richards [8]. Prior to fatigue testing or deep rolling the fillet region of each deep roll sample was polished to a 6 μm finish after



Figure 3.6 The 100 kip MTS servo-hydraulic frame with woodmetal alignable grips and heat lamps in place for elevated temperature Bauschinger effect testing. The matte black paint to improve heating from the lamps is visible on the surface of the sample as well as the thermocouple wires from the spot welded k-type thermocouple for temperature control.

being machined. This was accomplished using a lathe to turn the samples while using progressively finer grits of sandpaper (240, 320, 400, 600, and 800 grit) in the fillet to 800 grit then polished with 6 μm diamond suspension. Samples were initially tested at 827 MPa (120 ksi), subsequent sample groups of three were tested at stress levels decreased by 138 MPa (20 ksi) until a stress level was identified where at least one of the three samples experienced 10^5 cycles. Once a stress level was reached where a sample experienced 10^5 cycles before failure the stress level was then decreased by 69 MPa (10 ksi) until a run out was achieved. The bending stress was calculated using the minimum radius of the fillet and ignoring the stress concentration factor to come up with a nominal bending engineering stress. A run out was defined as a sample that survived 10^7 cycles without failure. After a run out was achieved the stress level was increased by 34.5 MPa (5 ksi) for the next test. The highest stress level achieved with three run out samples and no failures was determined to be the endurance limit. The inherent error in this procedure for determining the endurance limit is ± 17.2 MPa (2.5 ksi).

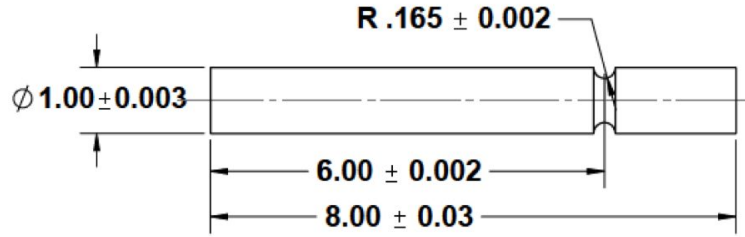


Figure 3.7 Deep Rolling fatigue sample developed by Richards [8]. (All dimensions are shown in inches)

3.4.1 Fatigue Machine Calibration

In order to calibrate the Baldwin SF-1-U fatigue machines used for this study a 30.5 cm (1 in) long 2.54 cm (1 in) diameter steel bar was obtained and fitted with two linear Micro-Measurements CEA-06-125UN-350 strain gages. The two strain gages were fixed opposite of each other on the bar 15.2 cm (6 in) from the loaded end of the bar. A Vishay 6100 data acquisition system was used with a 6010A strain gage card and a wiring adapter. A half bridge was wired to the card with the two strain gages. This set up can be seen in Figures 3.8 and 3.9. Strain was measured at a rate of 1000 points per second. Mathematica[®] was then used to fit a sine function to the data in the form of $a + b \sin(\omega t + \phi)$. The amplitude of the sine function, b , was used to calculate the applied stress. The modulus of elasticity for the steel rod was taken to be 206.8 GPa (30000 ksi) [49], which was used to convert the calculated strain amplitude to a stress. The stress on a bar loaded in cantilever bending was calculated as shown in Equation 3.3 [50].

$$\sigma = \frac{4PL}{\pi r^3} \quad (3.3)$$

In Equation 3.3 σ is the stress, P is the applied load, L is the length from the applied load to the strain gage, and r is the radius of the bar. Equation 3.3 was used to calculate the actual applied load to the sample, and this value was compared to the set point. A calibration curve of set point versus measured load was developed for each test unit used in this study.

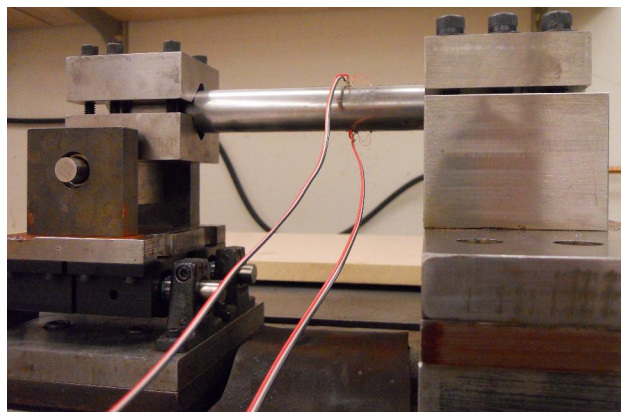


Figure 3.8 Strain gage set up for calibration of SF-1U fatigue machines showing the strain gaged bar with one gage on top and another on the bottom in the grips.

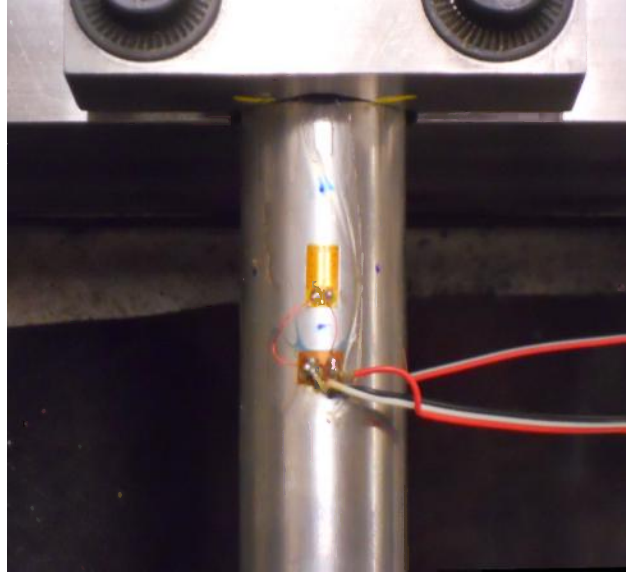


Figure 3.9 A top view of the strain gaged bar in the grips for bending fatigue tests on the SF-1U fatigue machines.

3.5 Deep Rolling

For this study the deep rolling device used at Colorado School of Mines was developed for a previous deep rolling study performed by Richards [8]. The device consists of three load rollers arranged in a tripod configuration for stability under load. The load roller geometry was designed to fit into the fillet of the deep roll sample (Figure 3.7). A hydraulic actuator was used to generate the force applied to the surface of the sample through the load rollers and was measured using a load cell in line with the load rollers, which are mounted on linear bearings on a rail system in order to create near frictionless linear motion of the load rollers towards the sample. The system was controlled using a MTS 458 microprofiler. A 1.12 kW (1.5 hp) motor was used to rotate the sample in a three jaw chuck while it was being loaded with the load rollers.

The loading sequence for a deep rolled sample after the sample was rotating included a preload period, ramp to the rolling load, and a hold at the rolling load in order to achieve 33 overrollings of the deep rolled sample. The samples were preloaded to 890 N (200 lbf) in order assure that the load rollers were not "rammed" into the surface of the fillet when going to the full deep rolling load. The hold time for the deep rolling process was set to 49.5 s in order to give 11 revolutions of the sample when the motor was set to a speed of 1.2 giving a rotational speed of 13.3 rpm. The number of overrollings was held constant for this study and chosen to be 33 (11 revolutions of the sample times three load rollers) according to Richards [8] previous work. The deep rolling device at CSM also dictates that the load roller geometry and sample geometry remain fixed, leaving only the rolling force and material as variables.

3.5.1 Optimization of Rolling Load

In order to determine the rolling load which would provide the greatest increase in fatigue performance an optimization procedure previously developed at Colorado School of Mines was performed [8]. It has been documented that an increase in the applied rolling force leads to an improvement in the fatigue performance

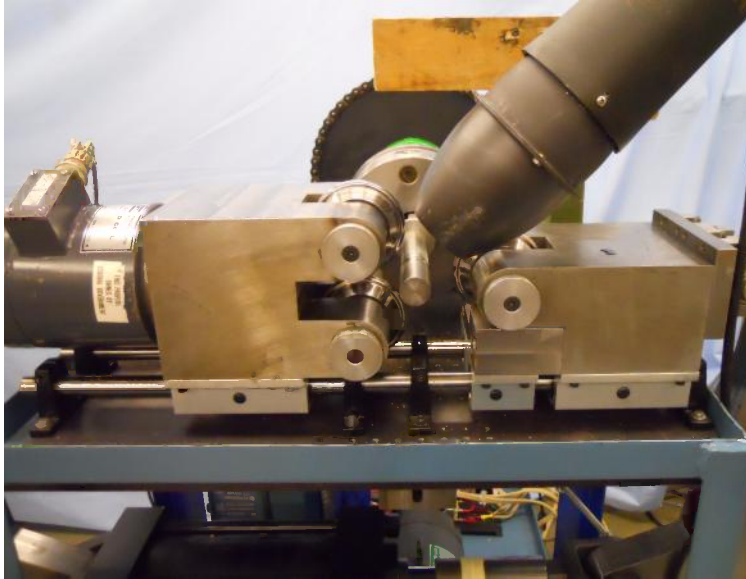


Figure 3.10 Deep Rolling Device (DRD) developed and built by Richards [8] at CSM. The tripod load roller arrangement can be seen as well as the load cell and the hydraulic actuator.

of deep rolled samples [7, 8, 35]. Eventually a peak performance was achieved and an increase in rolling load eventually leads to a decline in fatigue performance [35]. With the number of over-rollings being held constant at 33, the rolling load was varied between 3 kN (674 lbf) and 20 kN (4496 lbf) (the limits of the deep rolling device at Colorado School of Mines) for each alloy. The samples were then tested as described in Section 3.4. A constant stress amplitude was used for each sample chosen based on a stress amplitude at which the as received material survived approximately 20,000 cycles before failure. The number of cycles to failure (life at stress) was then plotted versus rolling load in order to generate an optimization curve. In order to determine an optimal rolling load for the material not only was the peak in the optimization curve considered but also the load at which damage became visible in the fillet of the sample under low magnification (5X to 10X). If cracks became visible on the surface of the fillet a lower rolling load was chosen as surface damage is considered to be detrimental to fatigue performance.

3.5.2 Elevated Temperature Rolling and Aging

After the optimal rolling load had been identified as described in Section 3.5.1, samples were deep rolled at room temperature and aged or rolled at elevated temperature. The temperature for aging after deep rolling was determined from the strain aging study described in Section 3.3.2. The aging temperature selected for the deep rolled samples was chosen such that the difference in strain aging index between the two materials was maximized. This was done in order to isolate the effect of static strain aging on the fatigue performance of deep rolled samples. Samples were then aged in an oil bath at the appropriate temperature following room temperature deep rolling, and were then fatigue tested to determine the endurance limit according to the previously outlined procedure.

In order to determine the temperature for elevated temperature rolling the curves for BEE, yield stress, 1% plastic flow stress, and 2% plastic flow stress versus temperature as described in Section 3.3.3 were considered. The goal was to maximize the dynamic strain aging effect in the C38N2 material while limiting

the effect in the C38M material. Once this temperature had been determined the samples were preheated in an ambient atmosphere furnace before being deep rolled. Before deep rolling at elevated temperature a furnace was used to preheat the samples to 100 °C. Two Spot IR heat lamps were used to heat the samples to the rolling temperature and maintain temperature during the deep rolling process. A K-type thermocouple in contact with the shoulder of the fillet was used to monitor the temperature of the sample during the deep rolling process. A sample with a thermocouple in contact with the fillet of the sample was used to compare the shoulder temperature to the temperature in the fillet so a set point for the heat lamps could be established in order to maintain the proper test temperature.

3.6 Fractography

Samples were chosen that failed 34 MPa (5 ksi) above the endurance limit for each condition for fractography. The fracture features were large enough that light optical fractography was employed. A Cannon EOS 60D camera with a Cannon 50 mm lens and a 31 mm extension tube were used to document the selected fracture surfaces.

CHAPTER 4

RESULTS

4.1 Metallography

Metallographic coupons of both C38M and C38N2 were polished to a 1 μm finish then etched with a 4% nital solution. These metallographic coupons came from the same portion of the as received bar as the mechanical test samples were machined from and viewed radially. Representative light optical micrographs are shown in Figure 4.1. The microstructures of both materials consist of ferrite and pearlite with elongated manganese sulfide (MnS) stringers. From these micrographs the ferrite fraction, pearlite fraction, ferrite grain size, and pearlite colony size were calculated and a summary of these values is presented in Table 4.1. The ferrite grain size and pearlite colony size in the C38M material is finer than that of C38N2.

Table 4.1 – Ferrite-Pearlite fractions and grain sizes of C38M and C38N2

	Ferrite Fraction	Pearlite Fraction	Ferrite Grain Size (μm)	Pearlite Colony Size (μm)
C38M	0.249 ± 0.009	0.751 ± 0.009	6.19 ± 0.23	29.8 ± 0.92
C38N2	0.266 ± 0.009	0.734 ± 0.009	11.6 ± 0.44	35.0 ± 1.35

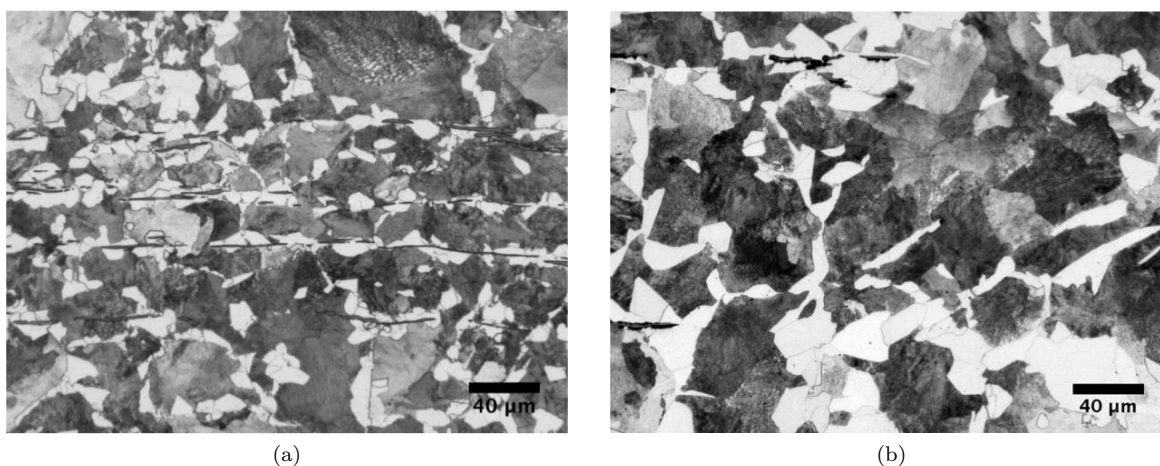


Figure 4.1 Light optical micrographs of C38M (a) and C38N2 (b) etched with a 4% nital solution. Both microstructures consist of ferrite and pearlite with manganese sulfide (MnS) stringers also present in the microstructure. These micrographs are taken from the same radius in the as received bars as the deep rolling samples were sectioned from and viewed radially.

4.2 Mechanical Testing

Basic material properties such as yield strength and ultimate tensile strength were determined using room temperature tensile testing in accordance with Section 3.3.1 with a minimum of three replicates tested for each material at a constant engineering strain rate of $1.6 \times 10^{-3} \text{ s}^{-1}$. Room temperature yield strengths

and ultimate tensile strengths are listed in Table 4.2. Figure 4.2 shows representative engineering stress strain curves for C38M and C38N2. The C38M material displayed a significantly higher yield and ultimate tensile strength than C38N2, but also displayed less uniform elongation. Both materials displayed yield point elongation (YPE), but two distinctly different behaviors were observed in the C38N2 material seen in Figure 4.3. In both cases there is YPE and after YPE occurs the work hardening rate and amount of uniform elongation is independent of the amount of YPE present.

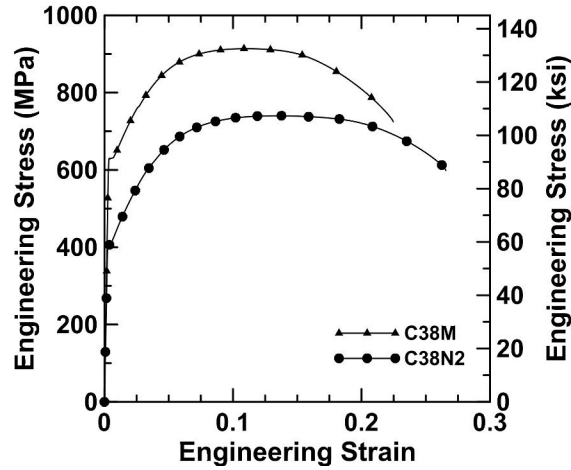


Figure 4.2 Example engineering stress strain curves for C38M and C38N2 at room temperature.

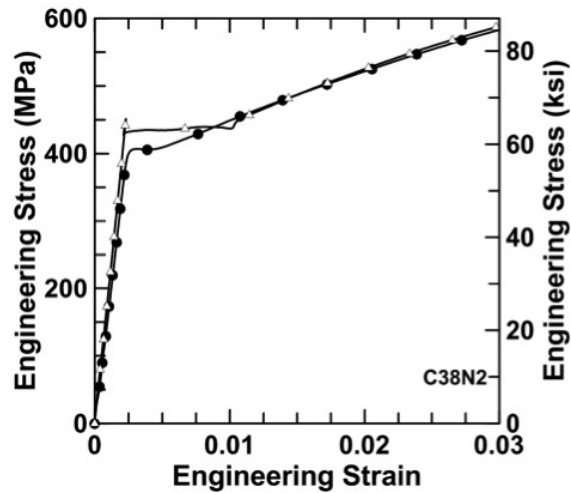


Figure 4.3 Two distinct yield behaviors were observed in the tensile testing and prestrain portion of the strain aging study in the C38N2 material. The difference in the two yielding behaviors is the amount of yield point elongation. After yield point elongation C38N2 exhibited the same uniform elongation and work hardening behavior independent of the amount of yield point elongation exhibited.

From Table 4.2 it is evident that there is a significant difference in the yield strength and ultimate tensile strength between the two steels. The microstructures of the two steels are very similar and while the ferrite grain size in C38M is finer than in C38N2. However, the observed grain size difference is not enough to explain the difference in strength levels between the two materials. The largest difference between the

two materials is the microalloying content. C38M contains significantly higher amounts of Al, Ti, and V compared to C38N2. Al, Ti, and V are all strong carbide and nitride formers in steel. Ti(N or C) and AlN typically precipitate at high temperatures in austenite or in the molten steel (especially Ti(N or C) which forms very stable precipitates at high temperatures), thus contributing to microstructural refinement and V(C or N) forms at lower temperatures and contributes to strengthening via precipitation strengthening [51]. In fact even modest additions of V (0.10 wt pct) in a medium carbon ferrite-pearlite steel can result in significant strengthening [52]. Even in an Al killed steel where there isn't as much solute N available for precipitation of VN there are significant strength increases associated with V(C,N) precipitation [53]. The effect of V(C,N) precipitation and the grain refinement together can explain the difference in strength levels between C38M and C38N2. The addition of V can also have an adverse effect on ductility, which may also be a factor explaining the decreased ductility of C38M when compared to C38N2.

Table 4.2 – Room temperature mechanical properties of C38M and C38N2

	Yield Strength (MPa)	Ultimate Tensile Strength (MPa)	YPE (%)	UE (%)
C38M	635	918	0.41	11.8
C38N2	430	745	1	12.5

4.2.1 Strain Aging

Tensile samples were prestrained to 2.5% in order to go beyond any discontinuous yielding that was present at room temperature. After prestraining samples were aged in oil or salt baths for 35 minutes at temperatures ranging from 100 °C (212 °F) to 260 °C (500 °F). After aging the aging index ($\Delta\sigma$) was calculated as described in Section 3.3.2 and illustrated in Figure 3.3.

The results of this aging study are shown in Figure 4.4. Three tests were conducted at each temperature and individual data points in Figure 4.4 represent each one of these tests. A clear difference in the aging response between the two materials is seen, especially in the low temperature region. The C38N2 material has a constant aging index at all temperatures tested whereas the C38M exhibits low $\Delta\sigma$ values at the lower temperatures and an increase in $\Delta\sigma$ with an increase in temperature. After aging at 220 °C (228 °F) both materials have approximately the same increase in strength from strain aging. The difference in $\Delta\sigma$ values at low temperatures is expected when the amount of nitride formers present in C38M compared to C38N2 is considered. The increased nitride formers in C38M limit the amount of interstitial N present to contribute to strain aging. As presented in Section 2.2, N is more mobile than C in ferrite meaning that a higher interstitial N content will lead to greater strain aging at lower temperatures. At higher temperatures the values of $\Delta\sigma$ are nearly the same in both materials due to the fact that C more mobile at higher temperatures meaning aging due to C diffusion can occur in C38M. The difference in aging response was greatest at 100 °C, therefore this temperature was chosen for the aging of deep rolled samples after being rolled at room temperature.

4.2.2 Bauschinger Effect Testing

Elevated temperature mechanical testing was performed at temperatures ranging from 100 °C (212 °F) to 300 °C (572 °F). In order to evaluate the Bauschinger effect tests were run in tension to 3% strain using strain gage control then the load was reversed and the test was terminated once a 3% compressive

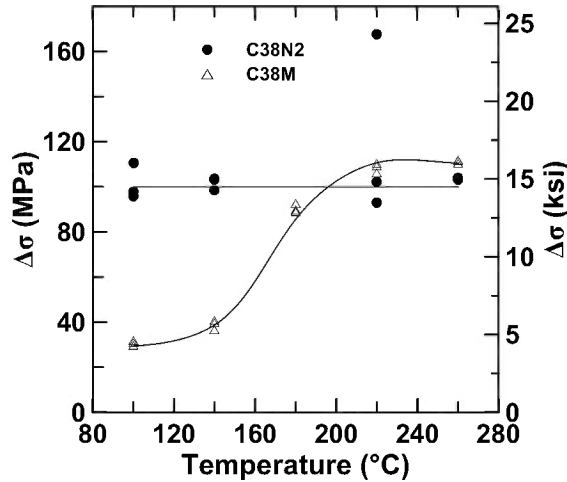
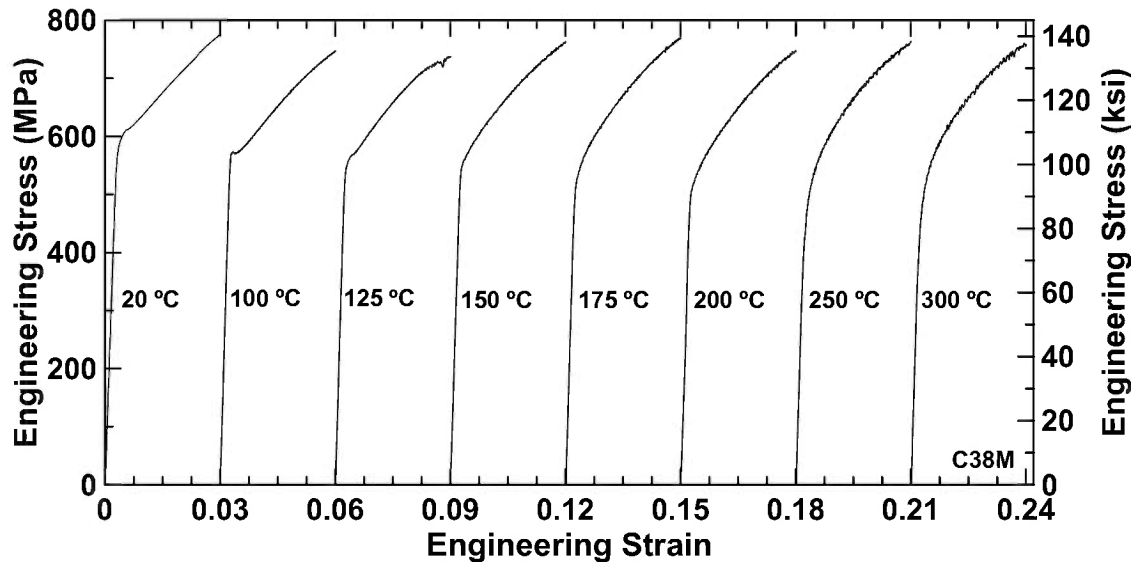


Figure 4.4 $\Delta\sigma$ versus temperature for C38M and C38N2. The effect of temperature on the strain aging index, $\Delta\sigma$, for C38M and C38N2 steels prestrained to 2.5% and aged for 35 minutes at the indicated temperatures.

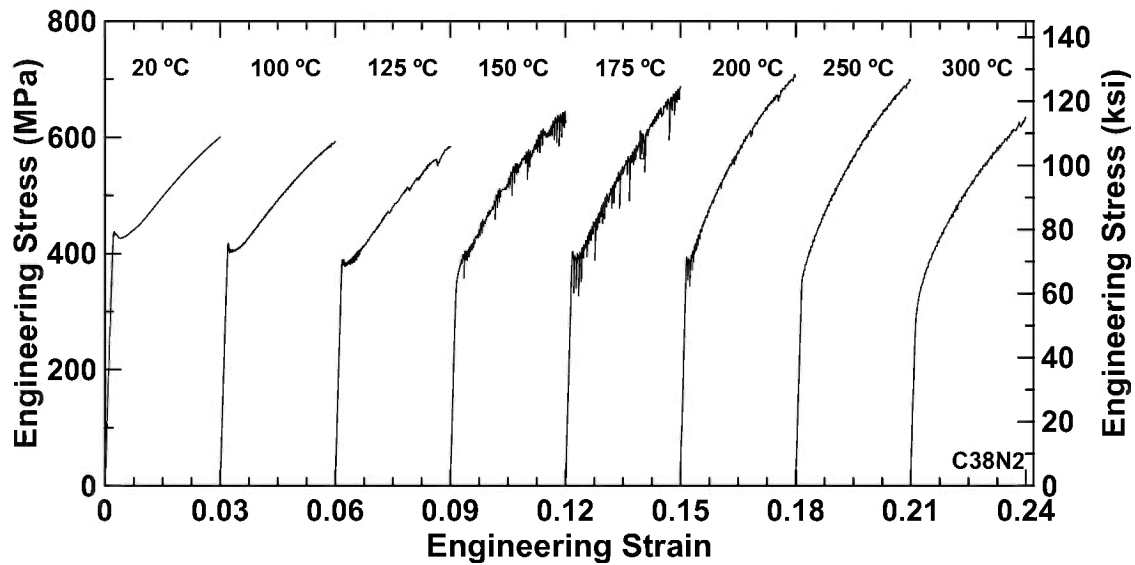
strain was reached at a constant engineering strain rate of 10^{-3} s^{-1} . Figure 4.5 shows the tensile portion of these tests for C38M (Figure 4.5a) and C38N2 (Figure 4.5b). From these figures it is evident that the deformation behavior of C38N2 is influenced more by the test temperature in the range tested than C38M. Serrations are apparent in the stress strain curves for C38N2 at the test temperatures of 150 °C and 175 °C, whereas the stress strain curves are relatively smooth in C38M for all temperatures tested. In addition to the transition from smooth to serrated flow with temperature a change in the work hardening behavior in the C38N2 material is seen with temperature. The work hardening rate increases with increasing temperature to 200 °C then decreases again.

The flow stresses at yielding, 1% true plastic strain, and 2% true plastic strain are shown in Figure 4.6. As test temperature increases C38M demonstrates the expected behavior in the absence of dynamic strain aging in that as temperature increases flow stress decreases [1]. When dynamic strain aging is active an increase in flow stress can be observed as it is for C38N2 especially in Figures 4.6b and 4.6c. The serrated yielding, work hardening differences, and the increase in flow stress with increased test temperature are all evidence of dynamic strain aging being active [48]. The dynamic strain aging response in C38N2 is expected with the increased solute N content compared to C38M due to the lack of Al, Ti, and V present.

Figure 4.7 shows typical stress reversal curves for C38M (4.7a) and C38N2 (4.7b) at 150 °C, again it is evident that at this temperature serrated flow occurs in C38N2 but not C38M indicative of dynamic strain aging being active in C38N2. From these stress reversal curves the BEF was calculated at each temperature tested using Equation 2.10 (shown in Figure 3.5). Figure 4.8 shows the effect of temperature on the BEF in C38M and C38N2. An isotropically hardening material will have a BEF of 1, meaning that the closer to 1 the BEF is, the less prevalent the Bauschinger effect becomes. In Figure 4.8 the BEF increases with increasing temperature in both C38M and C38N2. In the case of C38N2 the BEF increases more rapidly with temperature than it does in C38M. The decrease in the Bauschinger effect is attributed to dynamic strain aging. In this process solute atoms are able to diffuse to dislocations and hinder reverse motion upon stress reversal compared to the unpinned state.



(a)



(b)

Figure 4.5 Elevated temperature stress strain curves for the tensile portion of the stress reversal tests for C38M (a) and C38N2 (b). Each curve on (a) and (b) represent one test performed at the temperature listed to a value of 3% strain.

Based upon the flow curves with temperature, the flow stress values versus temperature, and the effect of temperature on the BEF a temperature of 150 °C was chosen for elevated temperature deep rolling. This temperature was chosen such that dynamic strain aging would be active in the C38N2 material and not in C38M in order to determine the effect of dynamic strain aging coupled with deep rolling on fatigue performance.

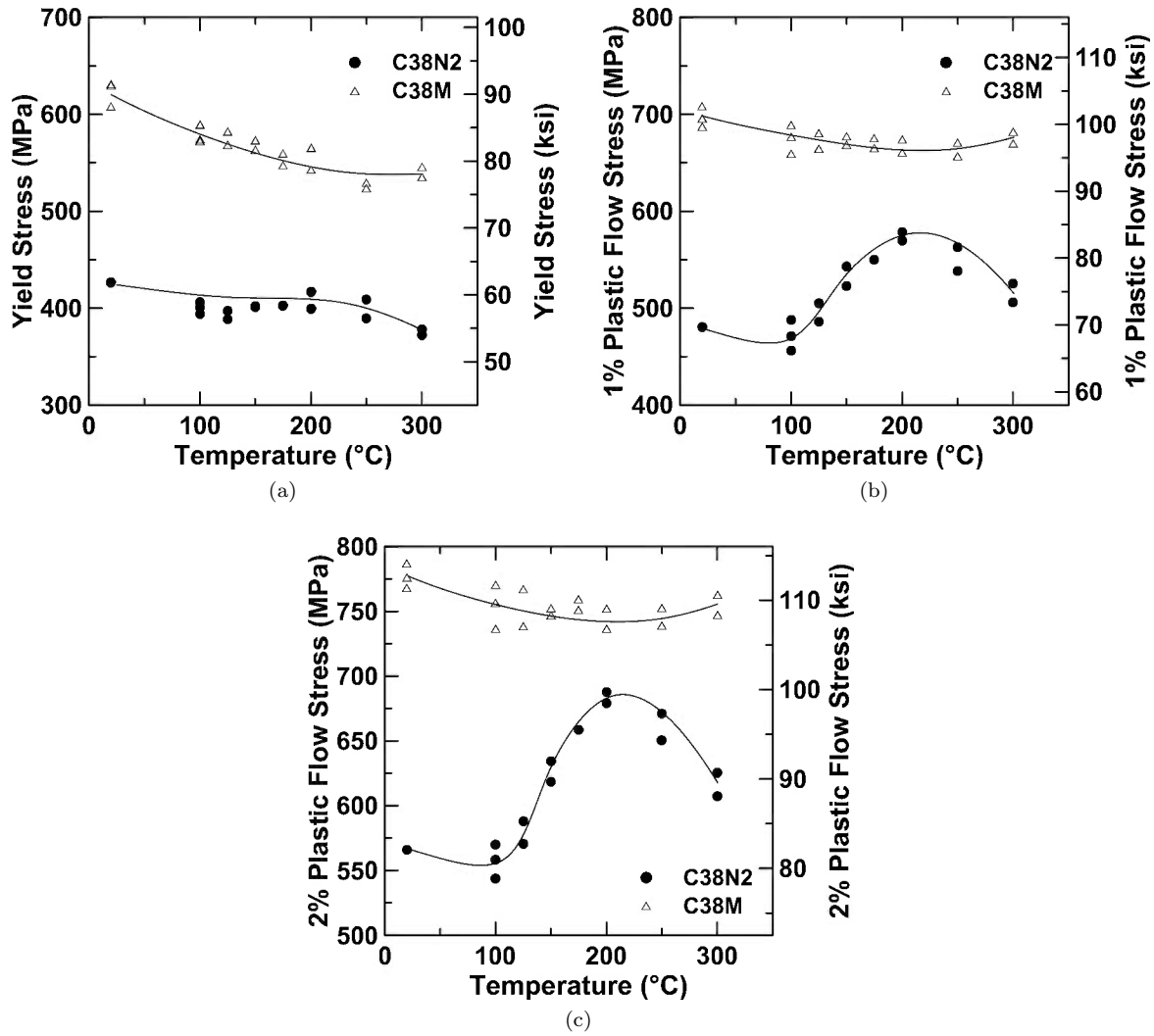


Figure 4.6 Flow stresses plotted versus temperature for yield stress (a), 1% plastic strain (b), and 2% plastic strain for C38N2 and C38M.

4.3 Fatigue Testing and Deep Rolling

In order to establish the as received fatigue performance of C38M and C38N2 fatigue tests were performed on the as received materials with the fillet polished to a 6 μm finish. Figure 4.9 shows the nominal applied stress (stress without stress intensity factor k_t being considered) versus the number of cycles to failure for the as received materials. Three samples were tested at each stress level and showed excellent reproducibility. A horizontal line was used to represent the endurance limit and an approximate fit for the high cycle data is shown as a curved spline line. The as received endurance limits of C38M and C38N2 are 310 MPa (45 ksi) and 241 MPa (35 ksi) respectively. C38M is expected to have a higher endurance limit than C38N2 due to the higher yield strength and UTS presented in Table 4.2.

After establishing the as received fatigue performance, a study was performed to establish the optimal deep rolling load. For this study a constant stress was chosen for fatigue testing and the deep rolling load was varied. Based on the data in Figure 4.9 the fatigue test stress level was chosen such that the as received

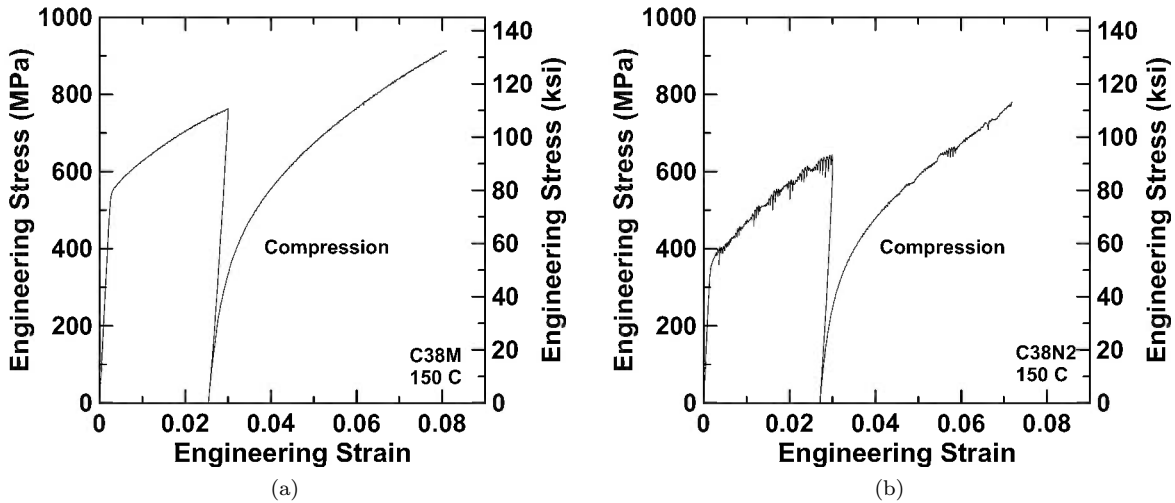


Figure 4.7 Engineering stress versus engineering strain curves for C38M (a) and C38N2 (b) tested at 150 °C. The compressive portion of the test is also represented in the tensile region of the plot for ease of representation. The flow curve for C38M is smooth, whereas the C38N2 flow curve is serrated which is a result of dynamic strain aging taking place during the test.

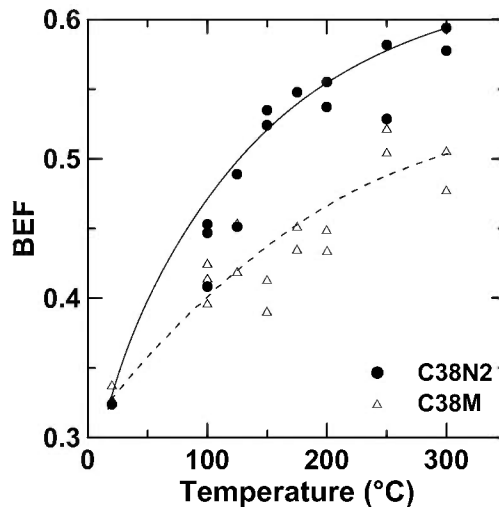


Figure 4.8 A plot of BEF versus temperature from 20 °C to 300 °C. An isotropically hardening material will have a BEF of 1, so as the BEF increases this means the Bauschinger effect is less prevalent. At least two tests were run at each temperature shown, each data point represents an individual test.

material would survive approximately 20,000 to 30,000 cycles. C38M was tested at 552 MPa (80 ksi) and C38N2 was tested at 483 MPa (70 ksi) and the results of the rolling load optimization are shown in Figure 4.10. In Figure 4.10 three samples were tested at each rolling load, and an increase in the number of cycles to failure is seen with an increase in the rolling load in both materials. With increased rolling load there eventually is a drop in the fatigue performance. At higher rolling loads this drop is apparent in the C38N2 material. In C38M with an increase in rolling load the number of cycles becomes more variable. For C38M the upper limit of the number of cycles to failure continues to increase for all rolling loads but if the lower limit of the data is observed there is a decrease in the number of cycles to failure. In addition to considering

the optimization curves for determining the rolling load surface damage was also considered. For both materials small cracks in the fillet were observed when rolled at 12.5 kN (2810 lbf). At higher deep rolling loads spalling of material off of the surface of the fillet was eventually observed. Examples of the damage observed in the fillet are shown in Figure 4.11 for C38N2 deep rolled at 12.5 kN and 20 kN. The rolling load chosen for deep rolling of both materials was 10.5 kN (2,360 lbf) based upon the surface damage at 12.5 kN and the shape of the optimization curves. Above this load the cycles to failure for C38N2 decreased and the variability in the cycles to failure for C38M increased. The increase in variability in the cycles to failure for C38M is thought to be a result of the dependence of the orientation of surface defects to the planes of maximum stress during fatigue testing.

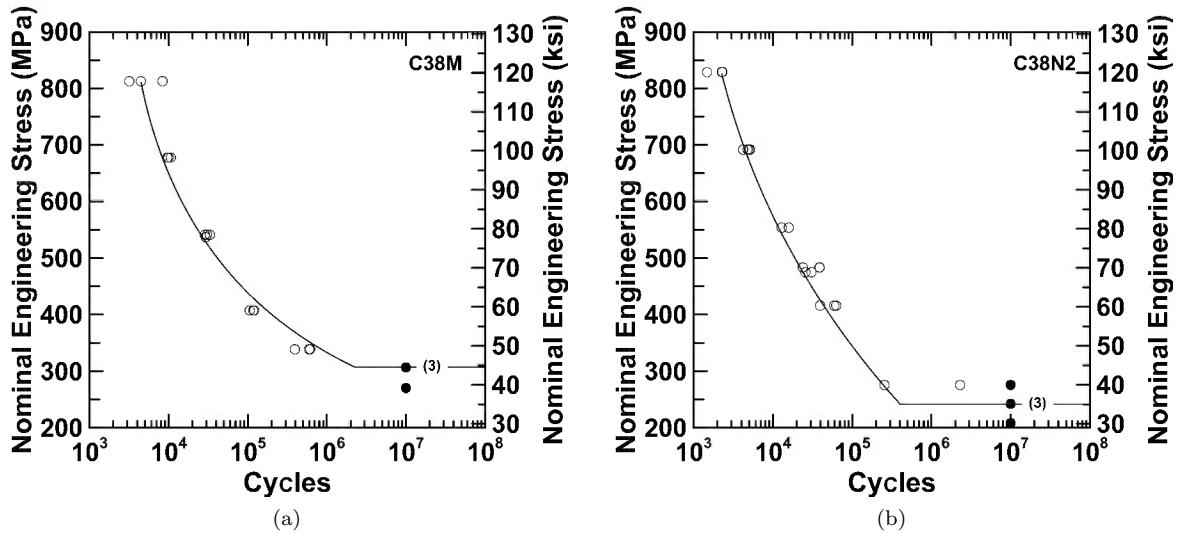


Figure 4.9 SN curve representing the as received fatigue performance of C38M (a) and C38N2 (b). Open symbols represent samples that failed and filled symbols represent run out samples. The nominal endurance limits of C38M and C38N2 are 310 MPa and 241 MPa, respectively.

After the optimization study samples for each material were deep rolled at room temperature and fatigue tested according to Section 3.4. In the case of C38N2 care was taken to deep roll the samples and start fatigue tests within 15 minutes of rolling to avoid room temperature strain aging. Figure 4.12 shows SN curves for the room temperature deep rolled (RT) condition and the baseline conditions for C38M and C38N2. In the low cycle fatigue region there is only a small increase in fatigue performance. As the fatigue load is decreased there is a greater improvement in the fatigue performance resulting from deep rolling. The behavior can be explained by the fact that at higher applied stresses the superposition of the compressive residual stress with the compressive cycle of bending fatigue can cause yielding and plastic flow leading to a relaxation of the residual stresses. The nominal endurance limits of the room temperature deep rolled C38M and C38N2 were found to be 483 MPa (70 ksi) and 379 MPa (55 ksi), respectively, as shown in Figure 4.12. This is a 56% increase in endurance limit over the as received condition for C38M and a 57% increase for C38N2.

In order to evaluate the effects of static strain aging and dynamic strain aging on the fatigue performance of deep rolled samples temperatures for strain aging and elevated temperature rolling were chosen based upon the strain aging study in Section 4.2.1 and the Bauschinger effect study in Section 4.2.2. For the static strain

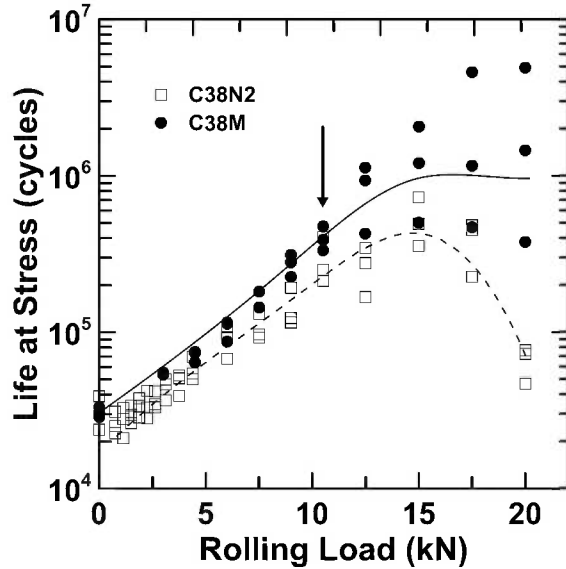
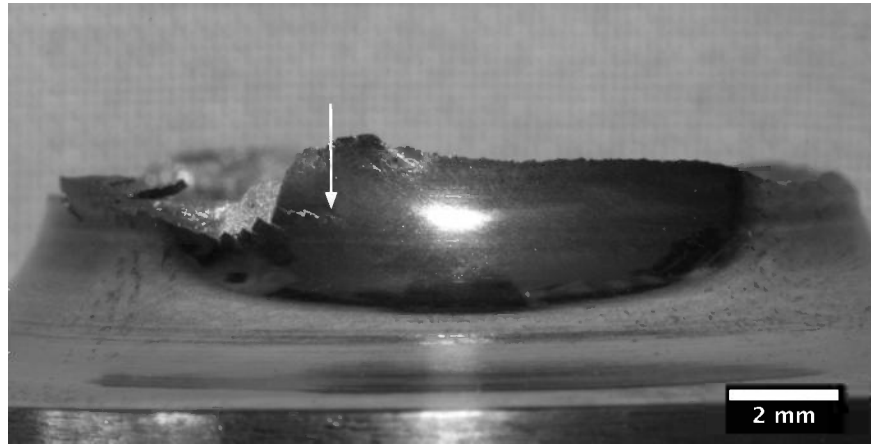


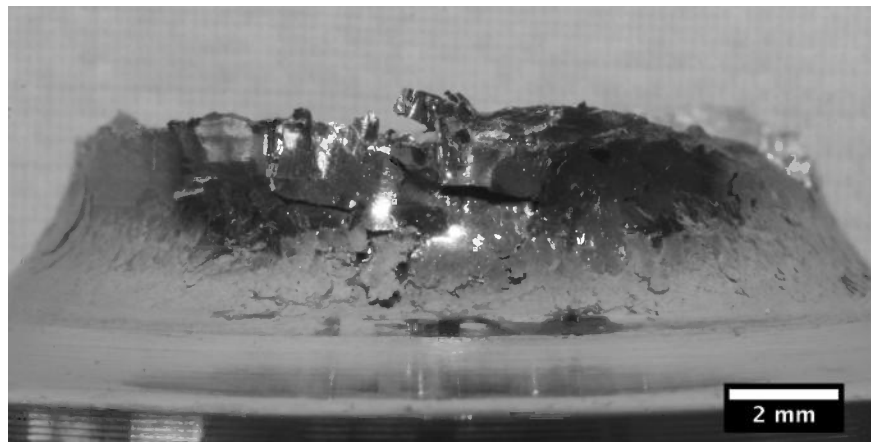
Figure 4.10 Optimization curve with the number of cycles to failure at stress plotted versus deep rolling load. The C38M was tested at 552 MPa (80 ksi) and C38N2 was tested at 483 MPa (70 ksi). The optimized rolling load was chosen to be 10.5 kN (denoted with an arrow) for both C38M and C38N2. Not only was the increase in fatigue life taken into consideration but also the appearance of surface damage due to the deep rolling process.

aging study samples were deep rolled at 10.5 kN at room temperature then aged for 35 minutes at 100 °C in an oil bath, a temperature selected where the strain aging response difference between the materials was at a maximum as shown in Figure 4.4. Figure 4.13 shows SN curves for the deep rolled then aged samples. The behavior of the aged samples is similar to the room temperature rolled samples in the way that at higher applied stress there is less improvement in fatigue performance than at lower applied fatigue loads due to stress relaxation at higher applied stresses. The aged nominal endurance limits of C38M and C38N2 are 483 MPa (70 ksi) and 414 MPa (60 ksi) compared to 483 MPa (70 ksi) and 379 MPa (55 ksi) for non-aged specimens. This is the same endurance limit for C38M in the room temperature deep rolled condition, and a 34 MPa (5 ksi) increase in the endurance limit for C38N2. This result is expected as the temperature for aging was chosen such that strain aging would be more prevalent in C38N2 compared to C38M.

The temperature chosen for elevated temperature deep rolling based upon Bauschinger effect testing and other elevated temperature properties was 150 °C based upon the results in Section 4.2.2. Samples were preheated to 100 °C in a furnace before being put in the deep rolling device. Once in the deep rolling device, infrared heat lamps were used to heat the samples to 150 °C and maintain the test temperature during the rolling process. Only an average 4 °C drop in temperature was observed during the deep rolling process, and it was found that after 5 minutes at temperature, the reading at the shoulder of the fillet was the same as the temperature in the fillet. Figure 4.14 shows the SN curves for the elevated temperature rolled samples. These curves are again similarly shaped to the room temperature rolled curves with greater improvement in performance realized at lower applied fatigue loads. The nominal endurance limits for the elevated temperature rolled condition are 483 MPa (70 ksi) for C38M and 448 MPa (65 ksi) for C38N2. The endurance limit for C38M is the same as observed in the room temperature deep rolled condition. An increase in the endurance limit of 69 MPa (10 ksi) for C38N2 was achieved through the use of elevated temperature deep rolling compared to the room temperature rolled condition. This again is expected as



(a)



(b)

Figure 4.11 Light optical images of C38N2 rolled at 12.5 kN (a) and 20 kN (b). Small cracks were observed in the fillet when rolled at 12.5 kN (marked with arrow) with much more extensive damage visible on the surface when deep rolled at 20 kN.

the temperature for rolling was chosen so dynamic strain aging would occur in C38N2 but not C38M. A summary of the endurance limits of C38M and C38N2 at the various deep rolling treatments applied is given in Table 4.3. Additionally, microhardness profiles of samples deep rolled at room temperature and those deep rolled at 150 °C were evaluated with Vicker's microhardness and are presented in Appendix D.

Table 4.3 – Nominal endurance ($\sigma_{e-nominal}$) limits of all conditions tested

	As-Received (MPa)	Deep Rolled (MPa)	Deep Rolled and Aged (MPa)	Elevated Temperature Deep Rolled (MPa)
C38M	310	483	483	483
C38N2	241	379	414	448

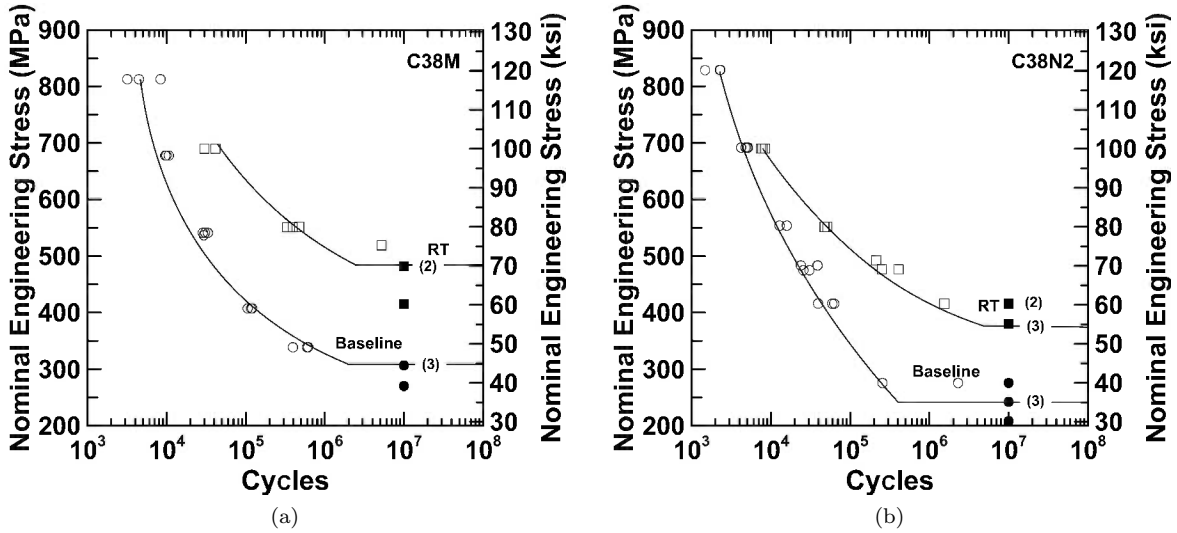


Figure 4.12 SN curves for C38M (a) and C38N2 (b) deep rolled at a rolling load of 10.5kN at room temperature. The deep rolled endurance limits for C38M and C38N2 are 483 MPa and 379 MPa, respectively.

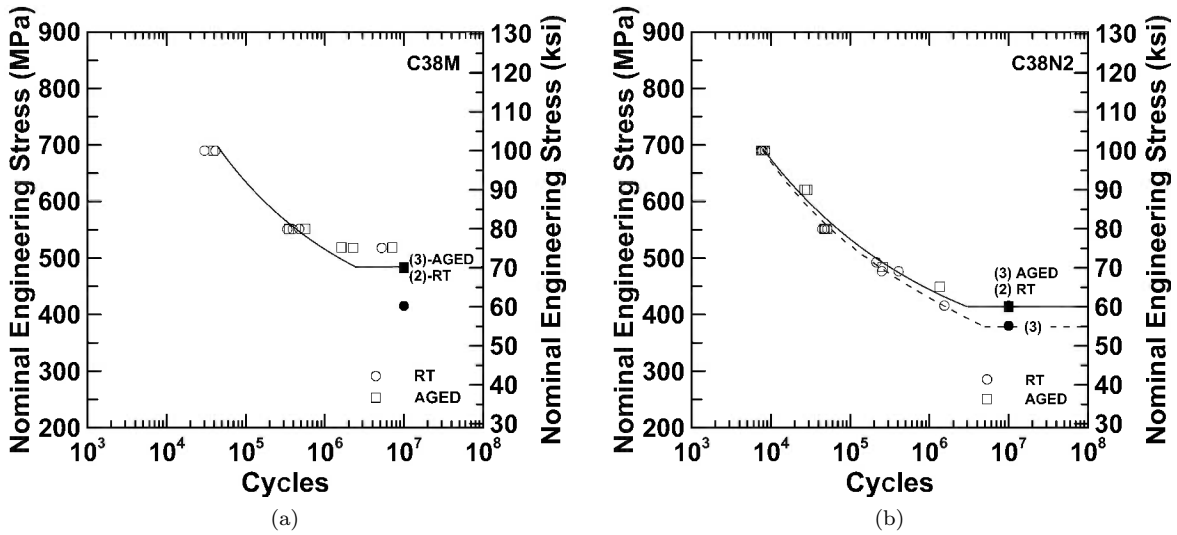


Figure 4.13 SN curves for C38M (a) and C38N2 (b) after being deep rolled at 10.5 kN at room temperature and aged at 100 °C for 35 minutes. The aged endurance limits of C38M and C38N2 are 483 MPa and 414 MPa, respectively.

4.4 Fractography

For each condition of C38M and C38N2 tested fracture surfaces tested at 34 MPa (5 ksi) above the nominal endurance limit were observed. Figure 4.15 shows the as received fracture surfaces. Both fracture surfaces are similar with an overload zone that is offset from the center of the sample. The top region of both fracture surfaces in Figure 4.15 have no visible ratchet marks and the region below the overload zone there are visible ratchet marks. The region above the overload zone is much larger than the region below suggesting that the first crack to nucleate was in this region, and the lack of ratchet marks suggests one

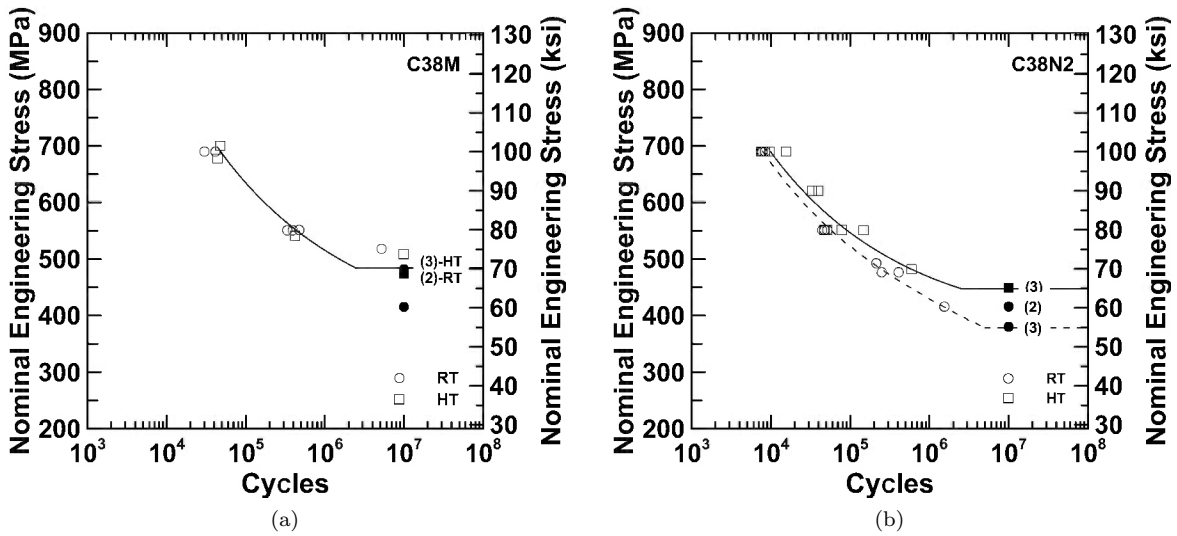


Figure 4.14 SN curves for C38M (a) and C38N2 (b) when deep rolled at 10.5 kN at a temperature of 150 °C with endurance limits of 483 MPa and 448 MPa, respectively.

initiation site. The change in initiation behavior in the bottom region (the appearance of multiple initiation sites) is likely due to an increase in the stress state caused by the reduction in area caused by the growth of the first fatigue crack. The samples were tested in fully reversed cantilever beam bending fatigue, which should produce an overload zone in the center of the sample. In fact, when samples were tested at higher stress levels the overload zone was in the center of the sample and the higher stress state also gave rise to an increase in the number of initiation sites evidenced by a higher number of ratchet marks. Figure 4.16 shows samples that were tested at 241 MPa (35 ksi) above the endurance limit.

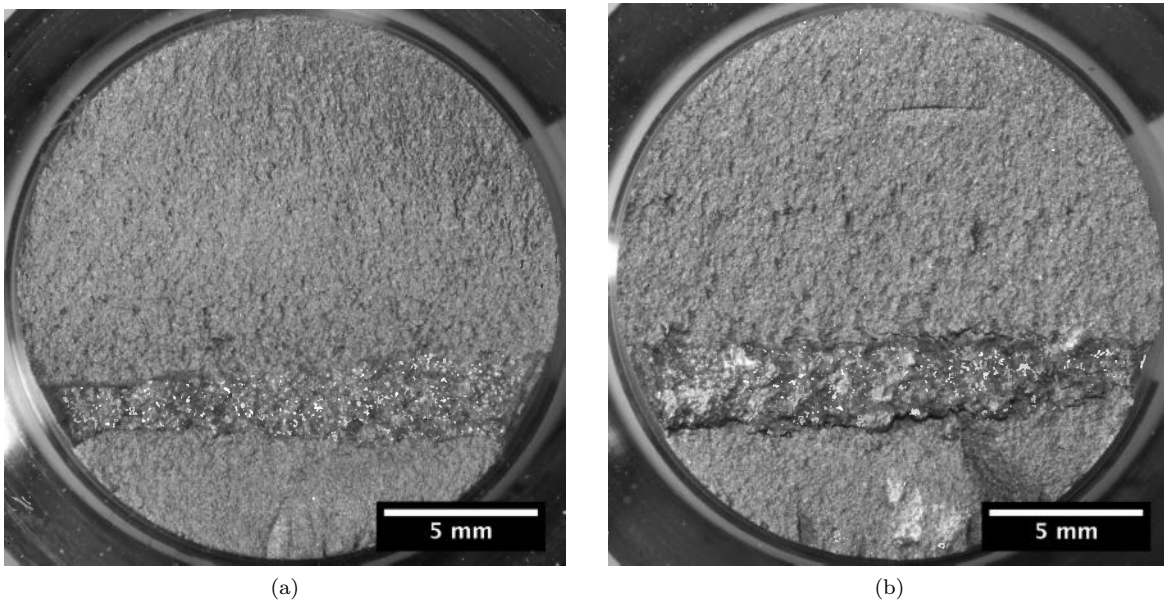


Figure 4.15 Fracture surfaces of as received condition material (a) C38M tested at 339 MPa (50 ksi) for 616,848 cycles before failure and (b) C38N2 tested at 275 MPa (40 ksi) for 2,304,272 cycles before failure.

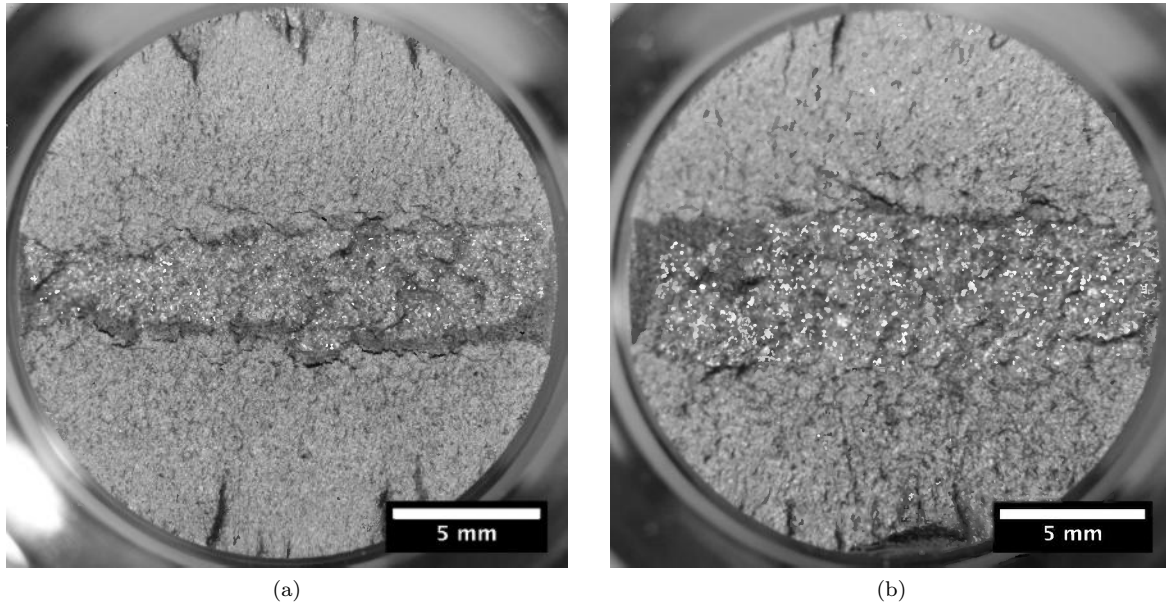


Figure 4.16 Fracture surfaces of (a) C38M tested at 552 MPa (80 ksi) for 30,646 cycles before failure and (b) C38N2 tested at 483 MPa (70 ksi) for 38,715 cycles before failure in the as received condition.

Figure 4.17 shows fracture surfaces of samples that were deep rolled at room temperature and tested at 34 MPa above the endurance limit. In Figure 4.17b an area around the outer region of the fracture surface appears to have been worn differently than the rest of the fracture surface. This outer "shiny" region is from the crack being arrested temporarily and the fracture surfaces being rubbed together before the crack is able to continue through the cross section of the sample (this region is also visible in Figure 4.17a but not as prevalent). This work hardened layer or case appears to be more visible and deeper in the softer C38N2 material in all treatments when compared to the fracture surfaces of C38M. The appearance of this region of crack arrest along with evidence of non propagating fatigue cracks found in a previous study [8] suggests that the main improvement in fatigue life due to deep rolling is through retardation of crack growth rather than preventing crack initiation. Also apparent in Figures 4.17a and 4.17b are the appearance of ratchet marks pointing to several initiation sites. The increase in initiation sites may be due to damage incurred during the deep rolling process. The overload zone in the samples deep rolled at room temperature is also offset from the center of the sample. Figure 4.18 shows room temperature deep rolled samples tested at 207 MPa (30 ksi) above the endurance limit for C38M and 172 MPa (25 ksi) for C38N2. Like the case for the as received tests at this higher level the overload region developed in the center of the sample.

The fracture surfaces for the deep rolled then aged and the deep rolled at elevated temperatures and tested 34 MPa above the endurance limits (shown in Figures 4.19 and 4.20) appear very similar to those of samples deep rolled at room temperature. Samples for both of these conditions tested at higher stress levels also exhibited overload in the center of the sample.

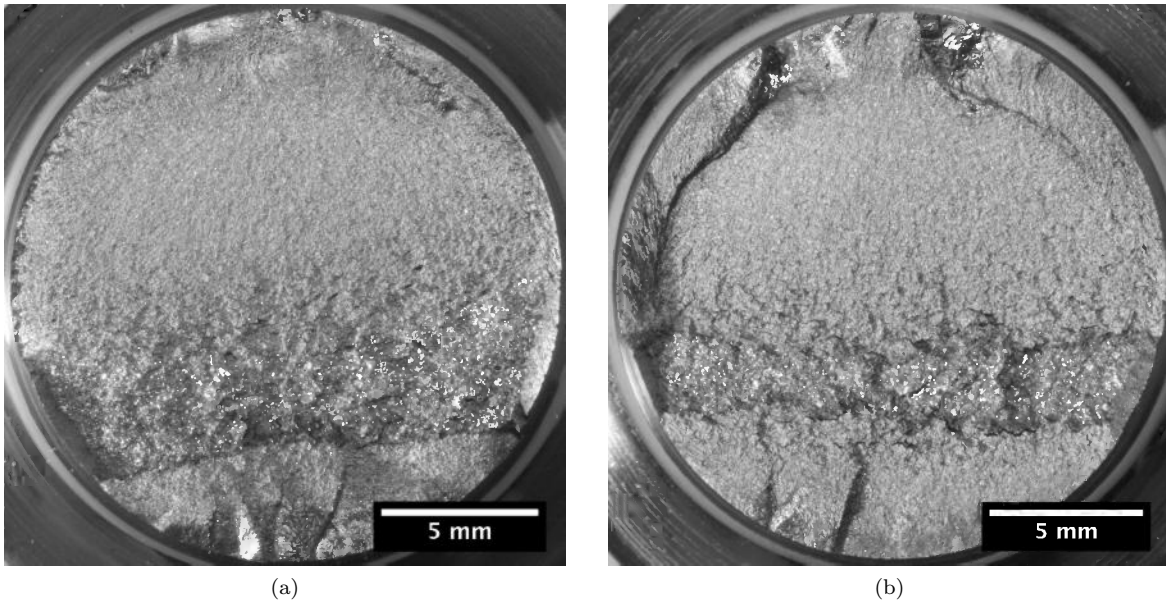


Figure 4.17 Fracture surfaces of (a) C38M tested at 509 MPa (75 ksi) for 5,224,261 cycles before failure and (b) C38N2 tested at 416 MPa (60 ksi) for 1,538,816 cycles before failure after being deep rolled at 10.5kN at room temperature.

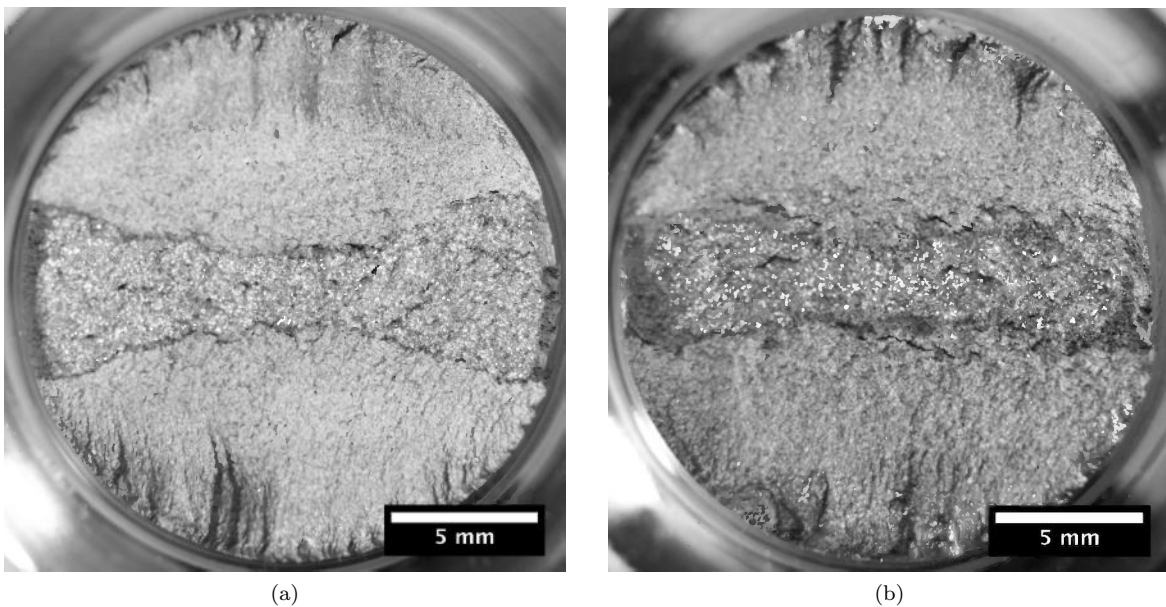


Figure 4.18 Fracture surfaces of (a) C38M tested at 690 MPa (100 ksi) for 41,423 cycles before failure and (b) C38N2 tested at 552 MPa (80 ksi) for 46,923 cycles before failure in the room temperature deep rolled condition.

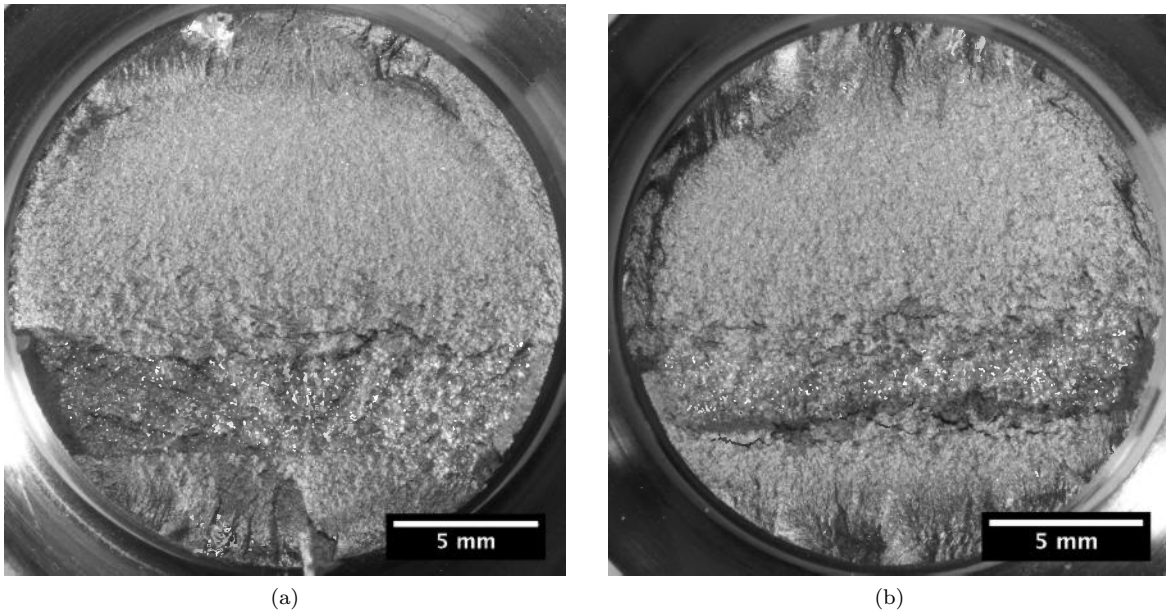


Figure 4.19 Fracture surfaces of (a) C38M tested at 509 MPa (75 ksi) for 1,618,563 cycles before failure and (b) C38N2 tested at 449 MPa (65 ksi) for 1,355,459 cycles before failure after being deep rolled at 10.5kN and aged at 100 °C for 35 min.

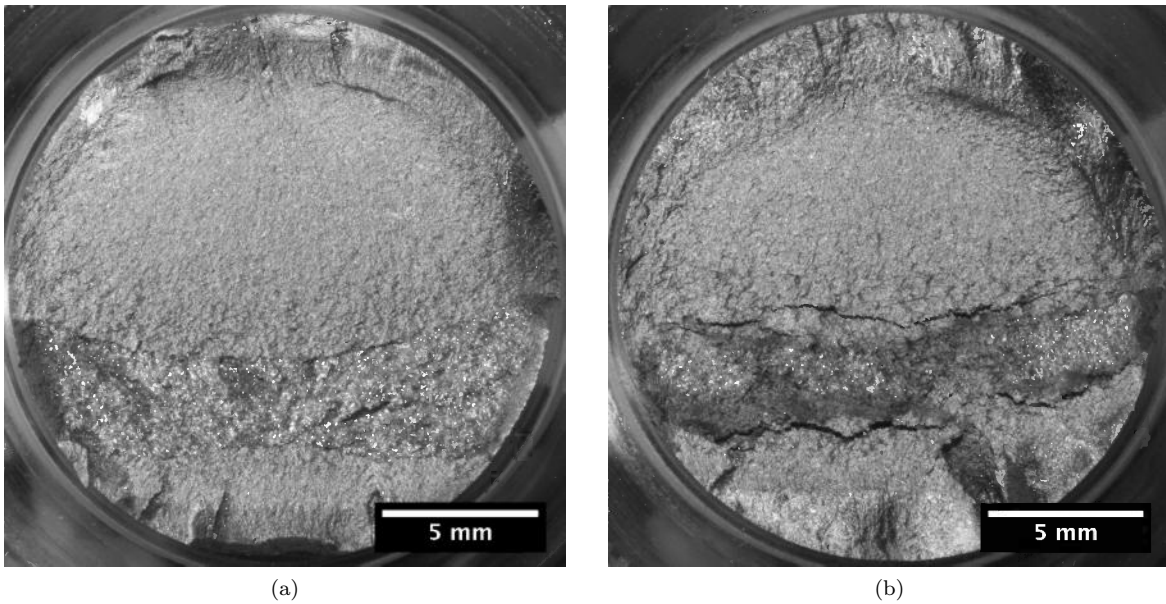


Figure 4.20 Fracture surfaces of (a) C38M tested at 509 MPa (75 ksi) for 9,851,000 cycles before failure and (b) C38N2 tested at 482 MPa (70 ksi) for 594,193 cycles before failure after being deep rolled at 10.5kN at 150 °C.

CHAPTER 5
DISCUSSION

5.1 Strain Aging Responses

From the strain aging study and the elevated temperature mechanical testing results, it is apparent that the strain aging responses of the two materials C38M and C38N2 is markedly different especially at lower temperatures (between 100 °C (212 °F) and 200 °C (392 °F)). In the static strain aging study C38N2 had a constant strain aging index of approximately 100 MPa (14.5 ksi) whereas C38M had a strain aging index of 35 MPa (5 ksi) at 100 °C which increased to a maximum of 105 MPa (15.2 ksi) at 220 °C (428 °F) (see Figure 4.4). This difference in strain aging response at lower temperatures is brought about by the lower amount of interstitial N in C38M, brought about by the difference in the N content as well as the difference in the content of microalloying elements present in C38N2 and C38M. The different amounts of N and microalloying elements present in the two materials are highlighted in Table 5.1.

Table 5.1 – The different amounts of nitrogen and microalloying elements present in C38M and C38N2 in wt pct.

	N	V	Ti	Al
C38M	0.0138	0.09	0.01	0.02
C38N2	0.0170	0.002	0.002	0.016

In order to obtain an understanding of approximately how much solute nitrogen remains in C38M and C38N2 at room temperature, equilibrium thermodynamic calculations were performed. The following analysis is based upon work performed by Speer *et al.* regarding vanadium carbonitride precipitation in austenite [54]. Equations 5.1 - 5.7 give the amount of Ti, V, Al, and N in solution and the amounts of TiN, VN, and AlN precipitated.

$$\log([Ti_m][N_m]) = \log(K_{TiN}) \quad (5.1)$$

$$\log([Al_m][N_m]) = \log(K_{TiN}) \quad (5.2)$$

$$\log([V_m][N_m]) = \log(K_{TiN}) \quad (5.3)$$

$$[Ti_s] = 0.7736f_{TiN} + [Ti_m] \quad (5.4)$$

$$[Al_s] = 0.6583f_{AlN} + [Al_m] \quad (5.5)$$

$$[V_s] = 0.7843f_{VN} + [V_m] \quad (5.6)$$

$$[N_s] = 0.2264f_{TiN} + 0.3417f_{Al} + 0.2157f_V + [N_m] \quad (5.7)$$

In Equations 5.1 - 5.7 $[X_m]$ is the concentration in wt pct of element X in the matrix, $[X_s]$ is the total concentration in wt pct of element X in the steel, K_{XN} is the solubility product of a specific nitride, and f_{XN} is the precipitate fraction of the specified nitride.

The solubility products (K) of TiN, AlN, and VN in ferrite come from Turkdogan [55] and are listed in Equations 5.8 - 5.10 where T is temperature in Kelvin.

$$\log(K_{TiN}) = -\frac{18,420}{T} + 6.40 \quad (5.8)$$

$$\log(K_{AlN}) = -\frac{8,790}{T} + 2.05 \quad (5.9)$$

$$\log(K_{VN}) = -\frac{9,720}{T} + 3.90 \quad (5.10)$$

Calculations for both C38M and C38N2 were first made by assuming equilibrium in ferrite with TiN, AlN, and VN. Equations 5.1-5.7 only take into account thermodynamic equilibrium and do not take into account any kinetics of formation. The system of seven equations was solved at room temperature (293 K (68 °F)) for both C38M and C38N2 with the aid of Mathematica[®]. In the equilibrium room temperature case for C38N2 there is 0.0076 wt pct solute N remaining. At room temperature there is no real numerical solution for the amounts of Ti, Al, and V in relation to the amount of N present in the steel. In order to be solved numerically in this fashion there needs to be excess N in relation to the microalloying elements present. In order to gain an understanding of how much N is present in C38M the thermodynamic calculations were performed using only Ti and Al. This was considered because in the austenite Ti and Al form much more stable nitrides than V meaning they would precipitate out of solution first [55]. In this case there is 0.00049 wt pct solute N remaining in solution. This would however most likely not remain in solution and would be precipitated out as V(C,N) leaving essentially no N in solution for C38M. This would support the difference in strain aging (Section 4.2.1) and dynamic strain aging (Section 4.2.2). The greater presence of V(C,N) precipitates also explains the increase in strength that is observed in C38M compared to C38N2 [52].

The difference in the amount of solute N in the two materials gives rise to the very different aging responses observed in the two materials. C38N2 demonstrates a greater static strain aging response at lower temperatures (100 °C to 200 °C) than C38M. Strain aging at these lower temperatures is typically attributed to solute N [2, 3]. Once strain aging due to C diffusion becomes more active, at approximately 220 °C, an increase in the strain aging index in C38M is observed (See Figure 4.4). At the higher temperatures tested for static strain aging (220 °C to 260 °C) the strain aging response was nearly equal for the two materials due to the fact that the strain aging response is now carbon controlled.

The difference in dynamic strain aging response between C38N2 and C38M is also likely due to the different solute nitrogen values. Through the evaluation of the BEF as a function of temperature it was observed that there was a greater reduction in the Bauschinger effect at lower temperatures in the C38N2 material. In fact, there was a greater reduction in the Bauschinger effect in the C38N2 material compared to the C38M material from 150 °C (302 °F) to 300 °C (572 °F) as evidenced by an increase in the BEF (see

Figure 4.8). This reduction of the Bauschinger effect comes from interstitial atoms moving to dislocations and increasing their resistance to motion in the reverse direction. Other evidence of dynamic strain aging in the C38N2 material in the temperatures tested were an increase in flow stress at 1% and 2% plastic strains. It is expected that as temperature increases flow stress will decrease, but if dynamic strain aging is active an increase in flow is observed. At 150 °C the flow curves for C38N2 were serrated (Portevin-Le Châtelier effect) giving further evidence of dynamic strain aging occurred at this temperature, while the flow curve for C38M is smooth (see Figure 4.7). The serrated flow curve is a result of dislocations becoming pinned by solute atmospheres then being able to break away with decreased flow stress then locked again by the mobile solute atmospheres.

5.2 Deep Rolling

Room temperature deep rolling significantly improved the fatigue performance of both materials. The values of the nominal endurance limits reported earlier do not take into account the stress concentration factor produced by the geometry of the notch in the deep rolling sample (Figure 3.7). The stress concentration factor k_t was calculated to be 1.5 [56]. The endurance limit with the stress concentration accounted for was calculated by multiplying the nominal endurance limit $\sigma_{e-nominal}$ by k_t and are shown in Table 5.2 along with percent increases over the as received condition.

Table 5.2 – Comparison of as received and room temperature rolled endurance limits (σ_e) with k_t taken into account.

	As Received (MPa)	Room Temperature Deep Rolled (MPa)	Percent Increase
C38M	465	724	56%
C38N2	362	569	57%

Both materials exhibited approximately the same percent increase in endurance limit resulting from deep rolling at 10.5 kN over the as received endurance limit. This similarity in improved performance is despite the higher strength of the C38M material over that of C38N2. Both materials have microstructures consisting of ferrite and pearlite with pearlite fractions of 0.73 (C38M) and 0.75 (C38N2) (see Table 4.1). This similarity in microstructure and differences in yield stress, UTS, and as received endurance limit yet the same improvement in fatigue performance due to deep rolling may point to the microstructure being very important to room temperature deep rolling response. In the case of the materials tested, the amount of ferrite and pearlite present appear to dictate the room temperature deep rolling response, not the ferrite grain size or pearlite colony size.

5.3 Aging Effects on Deep Rolling

In connection with the strain aging study conducted a set of samples from each material was deep rolled at room temperature then aged. The temperature chosen to age room temperature deep rolled samples at was chosen based upon the results of the static strain aging study presented in Section 4.2.1. The objective was to choose a temperature at which the strain aging response between the two materials was at a maximum and to use the lowest temperature possible and still have strain aging active in order to suppress any other

diffusional processes that may be present. The temperature that was selected was 100 °C for 35 minutes based upon the strain aging index of the two materials at this temperature. The strain aging index of C38M at 100 °C for 35 minutes was 43 MPa (6.2 ksi) and was 100 MPa (14.5 ksi) for C38N2 at the same temperature and time. This difference in the aging response was discussed in Section 5.1. When the deep rolled samples were aged the endurance limit of C38N2 increased from 569 MPa (82.5 ksi) to 621 MPa (90 ksi) (when the nominal endurance limit is multiplied by k_t) which represents an increase of 52 MPa (7.5 ksi). When C38M was aged after deep rolling the endurance limit was 724 MPa (105 ksi), which was the same as the room temperature deep rolled condition. The endurance limit of C38N2 increased when aged at 100 °C as a result of static strain aging being active whereas strain aging was not as prevalent in C38M at the same temperature. A summary of the endurance limits of all conditions tested once k_t has been applied is presented in Table 5.3. Residual stresses are the most beneficial effect of the deep rolling process meaning that the pinning of the dislocations generated during deep rolling by strain aging is likely stabilizing these residual stresses and prolonging the number of cycles crack growth is retarded or in the case of the endurance limit increasing the stress at which a crack becomes arrested.

Elevated temperature mechanical testing was performed to determine the temperature at which dynamic strain aging was active in the C38N2 material and not C38M as well as to assess how well dynamic strain aging reduced the Bauschinger effect. It was expected that dynamic strain aging would be more active at lower temperatures in C38N2 than C38M again due to the increased solute N content in C38N2. A number of factors were used to assess whether dynamic strain aging was active including, BEF, plastic flow stress, and the shape of the stress strain curves. Dynamic strain aging has been shown to increase the BEF, thus reducing the Bauschinger effect [5, 26]. In the room temperature state the BEF of both materials was between 0.33 and 0.34. In both materials as the temperature was increased the BEF also increased, but at 150 °C the BEF in C38N2 had increased to 0.54 and had only increased to 0.4 in C38M. In addition to evaluating the BEF the plastic flow stresses at 1% and 2% plastic flow were evaluated. In the absence of dynamic strain aging it is expected that as testing temperature increases the resistance to plastic flow will decrease. When dynamic strain aging is active an increase in flow stress can be observed as well. When plastic flow stress was plotted versus temperature (Figure 4.6) in the temperature range of 100 °C to 300 °C the plastic flow stress at 1% and 2% plastic strain in C38M decreases slightly. In C38N2 an increase is seen in flow stress between 100 °C and 200 °C, at which point the flow stress starts to drop again. This is further evidence of dynamic strain aging being active at lower temperature in C38N2 than in C38M. Finally when the stress versus strain curves for the two materials were evaluated it was noticed that at 150 °C the curve for C38N2 was serrated while C38M had a smooth curve (Figure 4.7). Serrated flow is a manifestation of the Portevin-Le Châtelier effect, which is a result of dynamic strain aging. As a result of the BEF, plastic flow stress, and observation of serrated flow around 150 °C, this temperature was chosen for the elevated temperature rolling portion of the test.

Elevated temperature rolling was conducted at 150 °C in order that dynamic strain aging would be more active in C38N2 and not C38M. When rolled at elevated temperature the endurance limit of C38M was 724 MPa (105 ksi), which again was the same as the room temperature rolled condition. Deep rolling at 150 °C increased the endurance limit of C38N2 from 569 MPa (82.5 ksi) in the room temperature rolled condition to 672 MPa (97.5 ksi), and Table 5.3 presents a summary of all endurance limits for the conditions tested. Figure 5.1 shows the as received SN curves and room temperature deep rolled SN curves with the elevated temperature rolled curves. The increase in endurance due to deep rolling at 150 °C in C38N2 due to

dynamic strain aging is also likely due to the stabilization of residual stresses. It was demonstrated that the BEF was increased by dynamic strain aging, which represents an increased resistance to plastic flow upon strain direction reversal. This resistance to plastic flow is important as deep rolling preloads the surface in compression and when fatigue tested it experiences tensile forces. If plastic flow occurs during fatigue testing relaxation of the residual stresses can take place and in extreme cases compressive residual stresses which are beneficial to fatigue performance can be reversed to create detrimental tensile residual stresses. Thus the increased resistance to plastic flow upon strain direction reversal should aid in the stabilization of the residual stresses.

Based upon the observation that C38M experienced no increase in endurance limit when aged at 100 °C for 35 minutes or when deep rolled at 150 °C, and C38N2 did and also based upon the different aging responses of the two materials it can be concluded that strain aging and dynamic strain aging are beneficial to the fatigue performance of deep rolled ferrite pearlite bar steels.

Table 5.3 – Endurance limits for all conditions tested with the stress concentration factor k_t of 1.5 taken into account.

	As Received (MPa)	Room Temperature Rolled (MPa)	Room Temperature Rolled and Aged (MPa)	Elevated Temperature Rolled (MPa)
C38M	465	724	724	724
C38N2	362	569	621	672

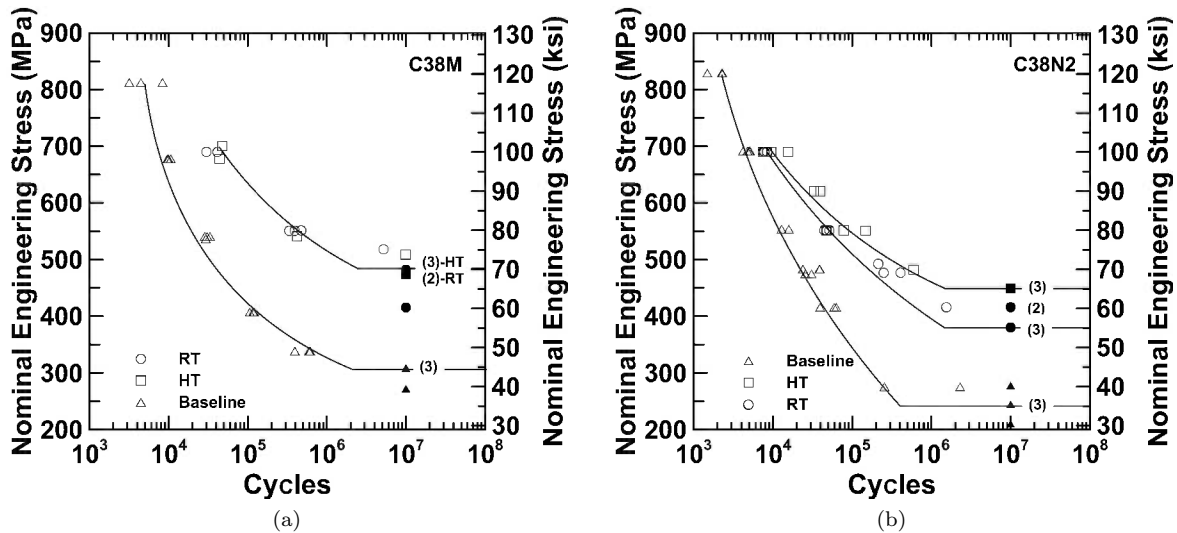


Figure 5.1 SN curves for C38M (a) and C38N2 (b) when deep rolled at 10.5 kN at a temperature of 150 °C (HT) with nominal endurance limits of 483 MPa and 448 MPa. Also presented are the as received (Baseline) and room temperature (RT) deep rolled conditions.

5.4 Comparison to Previous Results

Richards previously completed a study on deep rolling using three materials, one of which was also C38M from the Timken Company. This material was provided as 12.7 cm (5 in) hot rolled air cooled bars. The composition of this material is listed in Table 5.4, and is denoted as C38M*, along with the compositions

of C38M and C38N2 for comparison purposes. The composition of C38M* is very similar to that of C38M used in this study. The only significant differences in the compositions of the two steels are C38M* has a 0.010 wt pct Nb addition, 0.010 wt pct higher levels of V and Al, and has a slightly higher amount of N and S than C38M.

Table 5.4 – Compositions of Steels Used in Deep Rolling Project, with C38M* used previously by Richards [8] listed in (wt pct)

Alloy	C	Mn	Si	Ni	Cr	Mo	Ti	Nb	V	Al	N	S
C38M*	0.36	1.37	0.56	0.07	0.13	0.02	0.010	0.010	0.100	0.030	0.016	0.069
C38M	0.38	1.38	0.55	0.08	0.13	0.02	0.010	-	0.09	0.020	0.0138	0.057
C38N2	0.37	1.34	0.52	0.08	0.13	0.03	0.002	0.001	0.002	0.016	0.017	0.056

Light optical micrographs of C38M*, C38M, and C38N2 etched with 4% nital to reveal the microstructure are shown in Figure 5.2. Like the C38M and C38N2 the microstructure of C38M* consists of ferrite and pearlite with some MnS stringers present in the microstructure. The C38M* was received as a much larger diameter air cooled bar than C38M (12.7 cm versus 7.62 cm). As a result of this size difference a lower cooling rate is expected for C38M* and thus a coarser microstructure. The microstructure of C38M* was evaluated according to Section 3.2, and the microstructural details of all three materials are listed in Table 5.5. When comparing the ferrite grain size, C38M* in fact does have a larger grain size than C38M and a similar grain size to that of C38N2. In addition to light optical microscopy a brief transmission electron microscopy study was carried out on the C38M* material which had been room temperature deep rolled at 10.5 kN. The results of this study are presented in Appendix A.

Table 5.5 – Ferrite-Pearlite fractions and grain sizes of C38M and C38N2

	Ferrite Fraction	Pearlite Fraction	Ferrite Grain Size (μm)	Pearlite Colony Size (μm)
C38M*	0.344 ± 0.011	0.656 ± 0.011	12.4 ± 0.33	30.7 ± 0.89
C38M	0.249 ± 0.009	0.751 ± 0.009	6.19 ± 0.23	29.8 ± 0.92
C38N2	0.266 ± 0.009	0.734 ± 0.009	11.6 ± 0.44	35.0 ± 1.35

Yield stress, ultimate tensile strength, as received endurance limit, and room temperature deep rolled endurance limit data reported for C38M* by Richards [8] are reported in Table 5.6 along with values from C38M and C38N2. The yield stress and ultimate tensile strength values for C38M* are intermediate compared to C38M and C38N2. The same sample geometry for fatigue testing was used in Richards [8] study as the current study and the optimized deep rolling load for C38M* was also found to be 10.5kN. The as received endurance limit for C38M* was 241 MPa (35 ksi), the same as C38N2 despite C38M* have a 122 MPa (18 ksi) greater yield strength and 90 MPa (13 ksi) higher ultimate tensile strength.

In order to gain an understanding of how much strengthening in the C38M and C38M* is due to precipitation strengthening compared to C38N2, a ferrite pearlite strengthening model to predict yield stress presented by Pickering [57] was employed. Equation 5.11 shows the model used for this purpose:

$$\sigma_f = [16 + 0.27(\%pearlite) + 2.9(\%Mn) + 9.0(\%Si) + 60(\%P) + 11(\%Sn) + 244(\%N_f) + 0.97d^{-1/2}]1.57 \quad (5.11)$$

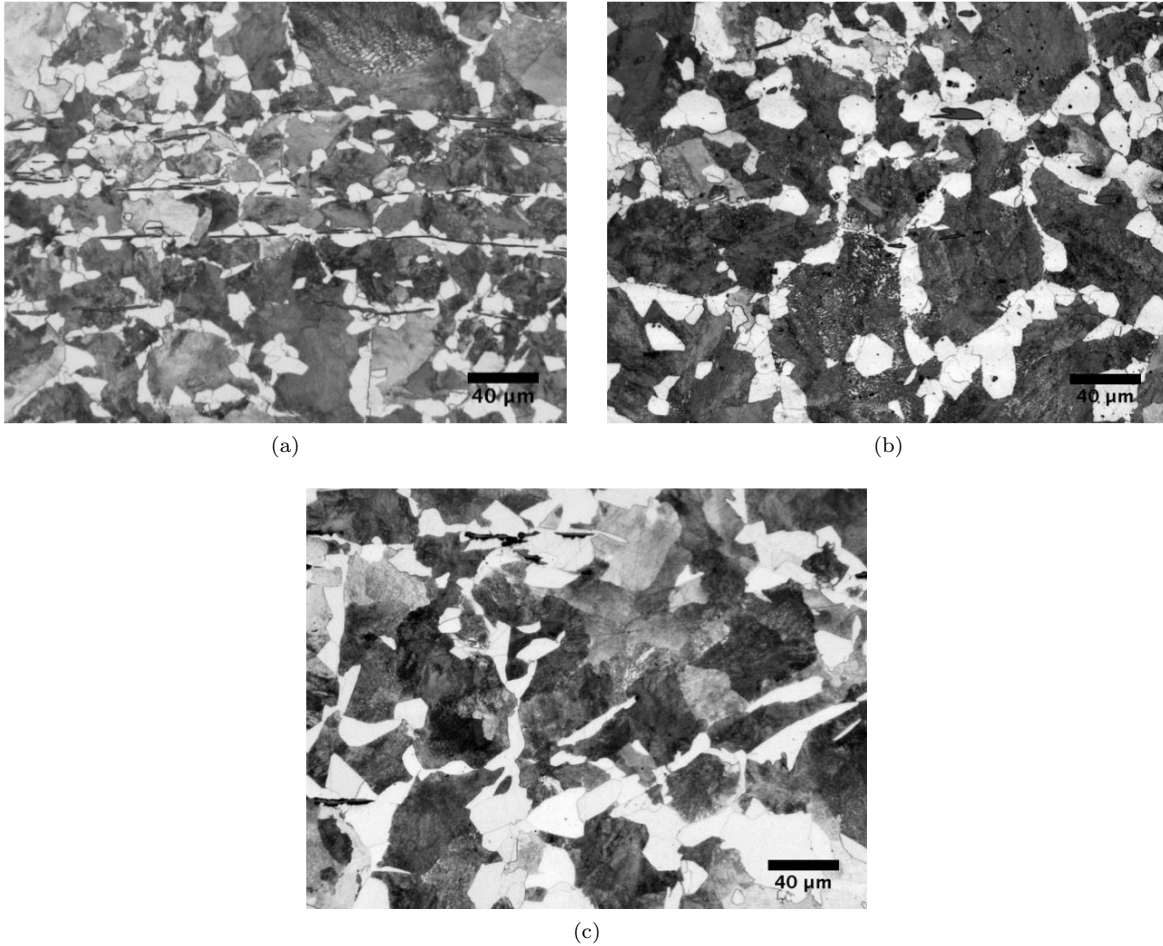


Figure 5.2 Light optical micrographs of C38M (a), C38M* (b), and C38N2 (c) etched with a 4% nital solution. All three microstructures consist of ferrite and pearlite with manganese sulfide (MnS) stringers also present in the microstructure. These micrographs are taken from the same radius in the as received bars as the deep rolling samples were sectioned from and viewed radially.

Table 5.6 – Mechanical Properties of C38M and C38N2 compared with reported data from Richards C38M* [8]

	Yield Strength (MPa)	UTS (MPa)	Nominal As Received Endurance Limit (MPa)	Nominal Room Temperature Deep Rolled Endurance Limit (MPa)	% Increase in Endurance Limit
C38M*	552	835	241	386	60.2%
C38M	635	918	310	483	56%
C38N2	430	745	241	379	57%

where σ_f is in (kg/mm^2) , d is ferrite grain size, and N_f is the amount of solute nitrogen present. Based upon previous thermodynamic calculations the value of N_f for C38M* and C38M used was 0, and for C38N2 0.0075 wt pct N_f was used. The results of these calculations of yield stress are shown in Table 5.7. It is important to note that this equation ignores precipitation strengthening and the interlamellar spacing within the pearlite which may contribute to strengthening as well. Table 5.7 shows that for the C38N2 material the model used predicts the yield strength within 16 MPa (*i.e.* 4%), where the predicted yield strengths

for C38M* and C38M are 161 to 241 MPa below the measured value. This result suggests significant precipitation strengthening present in both the C38M* and C38M. The magnitudes for strength increases attributed to precipitate strengthening are consistent with the value 165 MPa (24 ksi) in a high nitrogen V-containing steel reported by Gladowski in reference [10] and shown in Figure 5.3.

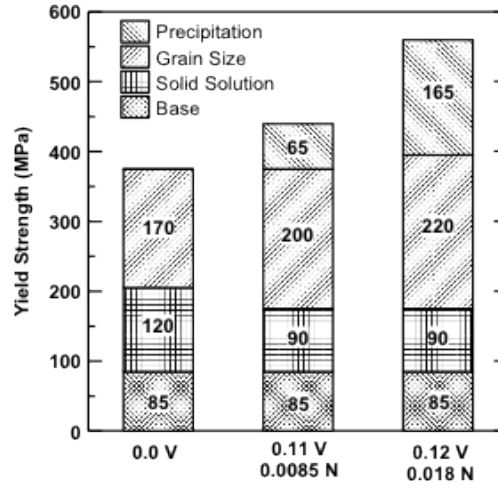


Figure 5.3 Strength enhancements (and contributions of individual strengthening mechanisms) to a 20MnSi (*i.e.* 0.0 V) base reinforcing bar steel resulting from additions of V (0.11 V, 0.0085 N; wt pct) or both V and N (0.12 V, 0.018 N; wt pct). Figure attributed to Gladowski as reported in [10].

In addition to precipitate strengthening, another potential microstructural difference between C38M* and C38M the pearlite interlamellar spacing, a value which depends in part on cooling rate. While not evaluated directly in this study it is predicted that the 12.7 cm (5 in) diameter C38M* hot rolled bar would have cooled at a slower rate than the 7.62 cm (3 in) diameter C38M bar leading to a finer pearlite spacing in the higher strength C38M.

Table 5.7 – Predicted yield stresses and experimental yield stresses

	Predicted yield stress (MPa)	Yield Stress (MPa)	Actual - Predicted
C38M*	391	552	161
C38M	394	635	241
C38N2	414	430	16

A comparison of the as received endurance limits for the three materials summarized in Table 5.6 shows that the endurance limits of C38N2 and C38M* are the same with C38M having the highest as received endurance limit. This suggests that the precipitation strengthening that is present in C38M* due to the additions of Al, Ti, and V does not contribute to an increase in fatigue performance. C38M has the highest as received endurance limit (310 MPa) and suggests that the strength improvement due to a refined microstructure (interlammellar spacing and ferrite grain size) improve the fatigue performance of the material. In all cases the the percentage improvement in endurance limit from room temperature deep rolling is nearly the same, giving more credence to the argument that room temperature deep rolling response reflects the microstructurally dependent strain hardening of the material.

CHAPTER 6

SUMMARY

The objective of this project was to determine the effects of aging on deep rolled medium carbon steels. Two steels that were used for this study contained different amounts of N, Ti, V, and Al. The result was that the C38N2 steel which contained low amounts of nitride formers had solute N present at the temperatures tested. A summary of the important observations and conclusions from this study are listed below.

1. Thermodynamic equilibrium calculations at room temperature illustrate that C38N2 should have interstitial N in solution and C38M will have a significantly reduced amount of N in solution if any at all.
2. The difference in solute N between the two materials led to a much different strain aging response. The C38N2 material had a constant aging index of 100 MPa from 100 °C to 260 °C when aged for 35 minutes at these temperatures. C38M had an aging index of 43 MPa at 100 °C and a maximum aging index of 105 MPa at 260 °C. The low temperature aging in C38N2 is attributed to the presence of solute N in the matrix. From these results the temperature of 100 °C was chosen to age deep rolled samples.
3. The dynamic strain response of the two materials was evaluated through the BEF, plastic flow stress, and the shape of the flow curves from elevated temperature uniaxial mechanical testing. For both C38M and C38N2 the BEF increased with increasing temperature but was more pronounced for C38N2 than C38M. For C38N2 in the temperature range of 100 °C to 200 °C the flow stress at a given plastic strain value in tension increased with increasing temperature and the flow curve was serrated at 150 °C. Both the increasing flow stress and serrated flow curves are evidence of dynamic strain aging being active. From these observations, 150 °C was chosen as the temperature at which to conduct elevated temperature deep rolling.
4. Samples from each material were deep rolled at room temperature then aged at 100 °C for 35 minutes and deep rolled at 150 °C to evaluate the effects of aging on the fatigue performance. For C38M there was no change in the endurance limit from static or dynamic strain aging over the room temperature deep rolled condition. For C38N2 an increase of 52 MPa in the endurance limit over the room temperature rolled condition was achieved by aging at 100 °C for 35 minutes. An increase of 103 MPa over the room temperature rolled condition was achieved by deep rolling at 150 °C. Both materials were treated in the same manner but only C38N2 achieved an improvement in fatigue performance as a result of strain aging being active in this material at the temperatures chosen.

CHAPTER 7

FUTURE WORK

The focus of the current study was to explore the effects of aging on the fatigue performance of deep rolled components. There are several opportunities that remain to improve the deep rolling process as well as gain a further understanding of the mechanisms operating during the elevated temperature deep rolling process. The following points are areas of further interest to understand the process of deep rolling and the interaction of aging with the deep rolling process.

1. It is thought that deep rolling at elevated temperature will produce a more stable dislocation structure leading to the improvement in fatigue life. There is opportunity to assess the difference in the dislocation structure between the deep rolled at room temperature and the structure produced by deep rolling at temperatures at which dynamic strain aging is active. Transmission electron microscopy can be used to evaluate the dislocation structures.
2. Predicting the optimized rolling load based on parameters such as microstructure, yield strength, ultimate tensile strength, etc. could be investigated as a potentially useful tool in the deep rolling process.
3. Further evaluation of the evolution of residual stresses from deep rolling through fatigue testing could be investigated using depth profiles taken for various rolling treatments and at different intervals throughout fatigue testing in order to determine whether or not aging or dynamic strain aging stabilize residual stresses more than merely deep rolling at room temperature.
4. The interplay of increasing the temperature of rolling and the rolling load is an area worth further investigation. With an increase in deep rolling temperature there is a possibility of increased ductility, decreasing the chance of surface damage from the rolling process. This decreased surface damage could result in the ability to roll at a higher load than possible at room temperature, thus being able to increase the fatigue performance with an increased rolling load and dynamic strain aging.
5. The effect of surface finish before the deep rolling process can also be investigated. In the current study all samples were polished to a 6 μm finish before being deep rolled. One beneficial effect of deep rolling is the burnishing of the surface that occurs because the load rollers are made to be smooth and harder than the part. A brief investigation of this is presented in Appendix C.

REFERENCES CITED

- [1] G. E. Dieter, *Mechanical Metallurgy*, 3rd ed., S. Rao, Ed. Boston, MA: McGraw Hill, 1986.
- [2] J. Baird, "Strain Aging A Critical Review," *Iron and Steel*, pp. 186–192, 1963.
- [3] T. Douthit and C. Tyne, "The effect of Nitrogen on the Cold Forging Properties of 1020 Steel," *Journal of Materials Processing Technology*, vol. 160, no. 3, pp. 335–347, Mar. 2005.
- [4] F. B. Pickering, "Some Beneficial Effects of Nitrogen in Steel," in *High Nitrogen Steels*, J. Foct and A. Hendry, Eds., vol. 36, no. 7. Lille, France: The Institute of Metals, 1988, pp. 10–31.
- [5] C. C. Li, J. D. Flasck, J. a. Yaker, and W. C. Leslie, "On Minimizing the Bauschinger Effect in Steels by Dynamic Strain Aging," *Metallurgical Transactions A*, vol. 9, no. 1, pp. 85–89, Jan. 1978.
- [6] I. Altenberger, "Deep Rolling The Past, the Present and the Future," in *Proceedings of 9th International Conference on Shot Peening*, Paris, France, 2005, pp. 144–155.
- [7] K. Kloos and J. Adelman, "Effect of Deep Rolling on Fatigue Properties of Cast Irons," *Journal of the Mechanical Behavior*, 1989.
- [8] M. D. Richards, "The Effects of Deformation Behavior on the Fatigue Performance of Deep Rolled Medium Carbon Bar Steels," Ph.D dissertation, Colorado School of Mines, Golden, CO, 2008.
- [9] *ASTM Standard E606/E606M-12, Standard Test Method for Strain-Controlled Fatigue Testing*. ASTM International, West Conshohocken, PA, 2012, ww.astm.org, 2012, vol. 92, no. 2004.
- [10] D. Matlock and J. G. Speer, "Microalloying Concepts and Application in Long Products," *Materials Science and Technology*, vol. 25, pp. 1118–1125, 2009.
- [11] D. J. Wulpi, *Understanding How Components Fail*, 2nd ed. Materials Park, OH: ASM International, 2000.
- [12] "ASM Handbook Volume 11: Failure Analysis and Prevention," Materials Park, OH, 2002.
- [13] T. Anderson, *Fracture Mechanics*, 3rd ed. Boca Raton, FL: CRC Press, 2005.
- [14] D. Hull and D. Bacon, *Introduction to Dislocations*, 5th ed. New York: Elsevier Ltd., 2011.
- [15] S. Vandeputte and B. C. D. Cooman, "Kinetics of Strain Aging in Bake Hardening Ultra Low Carbon Steel a Comparison with Low Carbon Steel," *Journal of Materials Engineering and Performance*, vol. 10, no. October, pp. 567–575, 2001.
- [16] A. Cottrell and B. Bilby, "Dislocation Theory of Yielding and Strain Ageing of Iron," *Proceedings of the Physical Society. Section A*, vol. 62, no. 1, pp. 49–62, Jan. 1949.
- [17] V. T. L. Buono, B. M. Gonzalez, and M. S. Andrade, "Kinetics of Strain Aging in Drawn Pearlitic Steels," *Metallurgical and Materials Transactions A*, vol. 29, no. 5, pp. 1415–1423, May 1998.
- [18] S. Gündüz, "Dynamic strain aging effects in niobium microalloyed steel," *Ironmaking & Steelmaking*, vol. 29, no. 5, pp. 341–346, Oct. 2002.
- [19] H. Karabulut and S. Gündüz, "Effect of Vanadium Content on Dynamic Strain Ageing in Microalloyed Medium Carbon Steel," *Materials & Design*, vol. 25, no. 6, pp. 521–527, Sep. 2004.
- [20] W. B. Morrison, "Nitrogen in the Steel Product," *Ironmaking & Steelmaking*, vol. 16, no. 2, pp. 123–128, 1989.

- [21] D. Wagner, N. Roubier, and C. Prioul, "Measurement of Sensitivity to Dynamic Strain Aging in CMn Steels by Internal Friction Experiments," *Materials Science and Technology*, vol. 22, no. 3, pp. 301–307, Mar. 2006.
- [22] J. F. Shackelford, *Introduction to Materials Science for Engineers*, 6th ed. Upper Saddle River, NJ: Prentice Hall, 2005.
- [23] G. Krauss, *Steels Heat Treatment and Processing Principles*. Materials Park, OH: ASM International, 1990.
- [24] I. Bauschinger, "Ueber die Veränderung der Elasticitätsgrenze und des Elasticitätsmoduls verschiedener Metalle," *Civilingenieur*, no. 5, pp. 289–348, 1881.
- [25] D. Williams, "Interaction Between the Bauschinger Effect and Strain Aging," *Metallurgical Transactions A*, vol. 11, no. 9, pp. 1629–1631, Jul. 1980.
- [26] M. Richards, C. Van Tyne, and D. Matlock, "The Influence of Dynamic Strain Aging on Resistance to Strain Reversal as Assessed Through the Bauschinger Effect," *Materials Science and Engineering A*, vol. 528, no. 27, pp. 7926–7932, Oct. 2011.
- [27] A. Aran and M. Demirkol, "Effect of Heat Treatment on the Bauschinger Effect for a Medium Carbon Steel," *Materials Science and Engineering*, vol. 47, no. 2, pp. 89–92, Feb. 1981.
- [28] M. Mataya, M. Carr, and G. Krauss, "The Bauschinger Effect in a Nitrogen-Strengthened Austenitic Stainless Steel," *Materials Science and Engineering*, vol. 57, no. 2, pp. 205–222, Feb. 1983.
- [29] A. Goel, R. Ray, and G. Murty, "Bauschinger Effect in a Dual-Phase Steel," *Scripta Materialia*, vol. 17, no. c, pp. 375–380, 1983.
- [30] D. V. Wilson, "Reversible Work Hardening in Alloys of Cubic Metals," *Acta Metallurgica*, vol. 13, no. July, pp. 807–814, 1965.
- [31] A. Sleswyk and G. Kemerink, "Similarity of the Bauschinger Effect in Cu, Al, and Ni," *Scripta Metallurgica*, vol. 19, pp. 471–476, 1985.
- [32] K. Han, C. Van Tyne, and B. S. Levy, "Effect of Strain and Strain Rate on the Bauschinger Effect Response of Three Different Steels," *Metallurgical and Materials Transactions A*, vol. 36A, no. September, pp. 2379–2384, 2005.
- [33] S. Okamoto, "Strain Rate and Temperature Effects on Deformation Behavior and Mechanical Properties of As-Quenched Low-Carbon Martensite," Master of Science, Colorado School of Mines, 1990.
- [34] G. Krauss, *Steels Processing, Structure, and Performance*. Materials Park, OH: ASM International, 2005.
- [35] K. Kloos, B. Fuchsbauer, and J. Adelman, "Fatigue Properties of Specimens Similar to Components Deep Rolled Under Optimized Conditions," *International Journal of Fatigue*, vol. 9, no. 1, pp. 35–42, Jan. 1987.
- [36] H. Michaud, J. M. Sprael, and F. Galzy, "The Residual Stresses Generated by Deep Rolling and their Stability in Fatigue & Application to Deep-Rolled Crankshafts," *Materials Science Forum*, vol. 524-525, pp. 45–50, 2006.
- [37] R. Gundlach, M. Semchyshen, and E. Whelan, "Notch Sensitivity and Fatigue in Austempered Ductile Iron," *SAE Technical Paper Series*, 1998.
- [38] F. Galzy, H. Michaud, and J. M. Sprael, "Approach of Residual Stress Generated by Deep Rolling Application to the Reinforcement of the Fatigue Resistance of Crankshafts," *Materials Science Forum*, vol. 490-491, pp. 384–389, 2005.

- [39] I. Altenberger, I. Nikitin, and B. Scholtes, “Static and dynamic strain ageing of deep-rolled plain carbon steel SAE 1045 for optimized fatigue strength,” in *Proceedings of 9th International Conference on Shot Peening*, Paris, France, 2005, pp. 253–260.
- [40] I. Altenberger, U. Martin, B. Scholtes, and H. Oettel, “Near Surface Microstructures In Mechanically Surface Treated Materials and Their Consequences on Cyclic Deformation Behaviour,” in *Proceedings of 7th International Conference on Shot Peening*, Warsaw, Poland, 1999, pp. 79–87.
- [41] M. Torres, “An Evaluation of Shot Peening, Residual Stress and Stress Relaxation on the Fatigue Life of AISI 4340 Steel,” *International Journal of Fatigue*, vol. 24, no. 8, pp. 877–886, Aug. 2002.
- [42] H. Holzapfel, V. Schulze, O. Vöhringer, and E. Macherauch, “Residual stress relaxation in an AISI 4140 steel due to quasistatic and cyclic loading at higher temperatures,” *Materials Science and Engineering: A*, vol. 248, no. 1-2, pp. 9–18, Jun. 1998.
- [43] R. Menig, V. Schulze, and O. Vohringer, “Optimized warm peening of the quenched and tempered steel AISI 4140,” *Materials Science and Engineering A*, vol. 335, no. 1-2, pp. 198–206, Sep. 2002.
- [44] A. Wick, “Effects of warm peening on fatigue life and relaxation behaviour of residual stresses in AISI 4140 steel,” *Materials Science and Engineering A*, vol. 293, no. 1-2, pp. 191–197, Nov. 2000.
- [45] *ASTM Standard E562, Standard Test Method for Determining Volume Fraction by Systematic Manual Point Count*. ASTM International, West Conshohocken, PA, 2012, ww.astm.org, 2013.
- [46] R. Higginson and C. Sellars, *Worked Examples in Quantitative Metallography*. London: Maney Publishing, 2003.
- [47] *ASTM Standard E8/E8M-11, Standard Test Methods for Tension Testing of Metallic Materials*. ASTM International, West Conshohocken, PA, 2011, ww.astm.org, 2011.
- [48] C. C. Li and W. C. Leslie, “Effects of Dynamic Strain Aging on the Subsequent Mechanical Properties of Carbon Steels,” *Metallurgical Transactions A*, vol. 9A, no. December, pp. 1765–1775, 1978.
- [49] W. D. Callister, *Materials Science and Engineering, An Introduction*, 7th ed. New York: John Wiley & Sons, Inc., 2007.
- [50] F. P. Beer, J. Johnston, E. Russell, and J. T. DeWolf, *Mechanics of Materials*, 4th ed. New York: McGraw Hill, 2006.
- [51] R. Lagneborg, T. Siwecki, S. Zajac, and B. Hutchinson, “The Role Of Vanadium In Microalloyed Steels,” *Reprinted from: The Scandanavian Journal of Mettallurgy*, no. October, 1999.
- [52] P. A. Parsons and D. V. Edmonds, “Microstructure and Mechanical Properties of Medium-Carbon Ferrite-Pearlite Steel Microalloyed with Vanadium,” *Materials Science and T*, vol. 3, no. November, pp. 894–904, 1987.
- [53] M. M. A. Bepari, “Effects of Precipitates on Strength and Toughness of Vanadium Structural Steels,” *Materials Science and Technology*, vol. 6, pp. 338–348, 1990.
- [54] J. G. Speer, S. Mehta, and S. S. Hansen, “Composition of Vanadium Carbonitride Precipitates in Microalloyed Austenite,” *Scripta Metallurgica*, vol. 18, no. 11, pp. 1241–1244, 1984.
- [55] E. Turkdogan, “Causes and Effects of Nitride and Carbonitride Precipitation During Continuous Casting.pdf,” *Iron and Steelmaker*, vol. 16, no. 9, pp. 61–75, 1989.
- [56] W. D. Pilkey, *Peterson’s Stress Concentration Factors*, 2nd ed. Hoboken, NJ, USA: John Wiley & Sons, Inc., Apr. 1997.
- [57] F. Pickering, “The Effect of Composition and Microstructure on Ductility and Toughness,” in *Toward Improved Ductility and Toughness*, 1971, pp. 9–31.

- [58] P. J. Withers and H. K. D. H. Bhadeshia, “Residual Stress Part 1 Measurement Techniques,” *Materials Science and Technology*, vol. 17, no. April, pp. 355–365, 2001.
- [59] B. Cullity and S. Stock, *Elements of X-Ray Diffraction*, third edit ed. Upper Saddle River, NJ: Prentice Hall, 2001.
- [60] C. Suryanarayana and M. G. Norton, *X-Ray Diffraction: A Practical Approach*. New York: Plenum Press, 1998.
- [61] A. Revesz, T. Ungar, A. Borgely, and J. Lendvai, “Dislocations and Grain Size in Ball-Milled Iron Powder,” *Acta Metallurgica*, vol. 7, no. 7, pp. 779–788, 1996.

APPENDIX A

TRANSMISSION ELECTRON MICROSCOPY

Limited transmission electron microscopy was conducted on C38M*, which was deep rolled at room temperature with a rolling load of 10.5 kN. Thin foils were sectioned from the root of the fillet such that the field of view was parallel to the bar axis. The sections from the bar were approximately 0.5 mm (0.02 in) thick and ground to a thickness of 150 μm (0.006 in). Once this thickness was achieved a 3 mm (0.12 in) diameter disc was punched out of the thin section as near to the surface of the fillet as possible. Samples were then electropolished in an electrolyte comprised of 95 pct acetic acid and 5 pct perchloric acid by volume until perforation in the middle of the disc occurred. If it is assumed that the perforation occurred near the center of the disc the TEM fields of view will be approximately 1.5 mm (0.06 in) below the surface of the fillet. A Phillips CM12 transmission electron microscope with a tungsten filament operating at 120 kV was used.

In the ferrite a high dislocation density was observed especially near grain boundaries. An example of this can be seen in Figure A.1. The dislocations in Figure A.1 appear to form parallel lines at a characteristic angle near the grain boundary. In the pearlitic ferrite a high dislocation density was also observed and is shown in Figures A.2 and A.3. Another characteristic observed in the deformed pearlite was that the cementite laths appeared to be sheared at a characteristic angle and is shown in Figures A.4 and A.5.

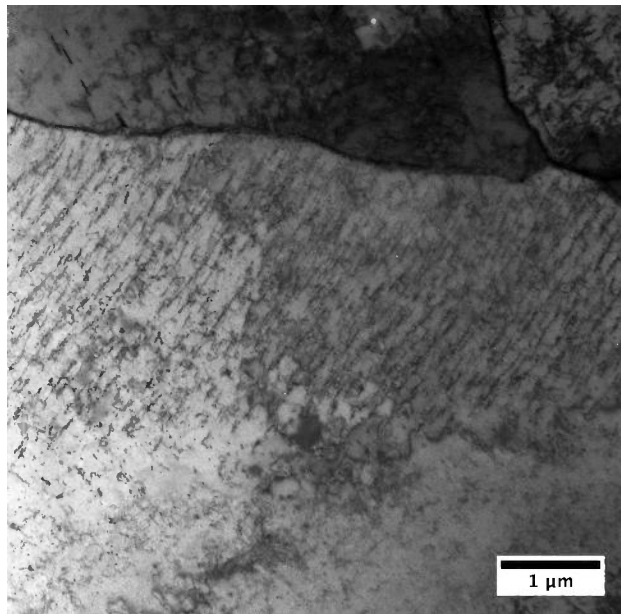


Figure A.1 Bright field TEM micrograph of C38M* after being deep rolled at 10.5 kN at room temperature showing a high dislocation density in the ferrite.

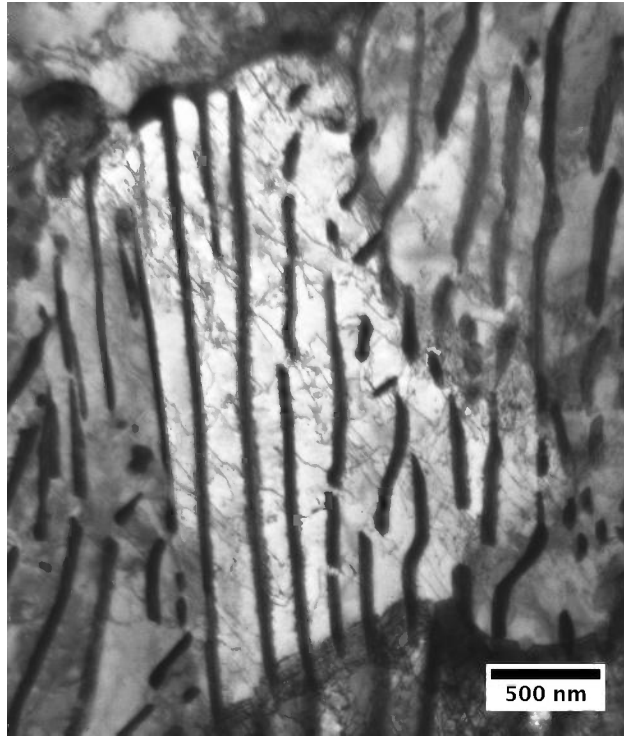


Figure A.2 Bright field TEM micrograph of C38M* after being deep rolled at 10.5 kN at room temperature showing a high dislocation density in the pearlitic ferrite. The dark laths are cementite and the lighter colored areas are ferrite. The cementite laths appear to be cleaved at a characteristic angle with dislocation coming off of the tips of the cleaved lamellae in the ferrite.

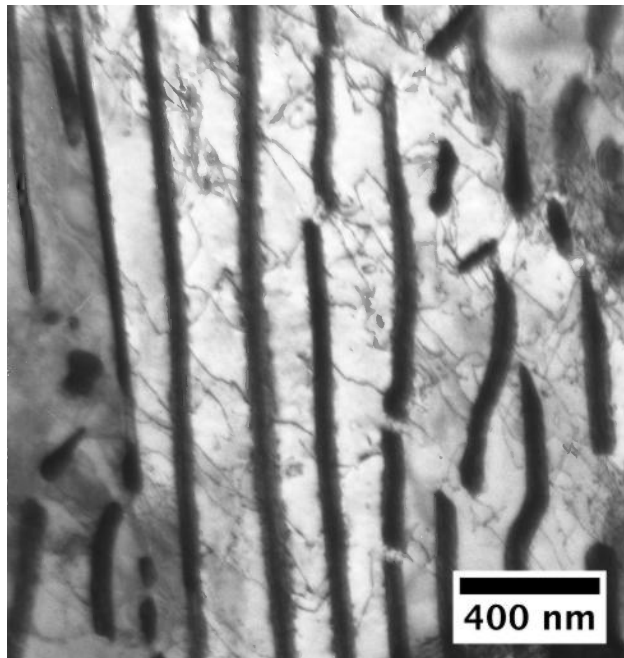


Figure A.3 A closer view of the TEM micrograph presented in Figure A.2. Dislocations are evident in the pearlitic ferrite. The cementite lamellae appear to be sheared at a characteristic angle related to the angle most of the dislocations are oriented in the ferrite.

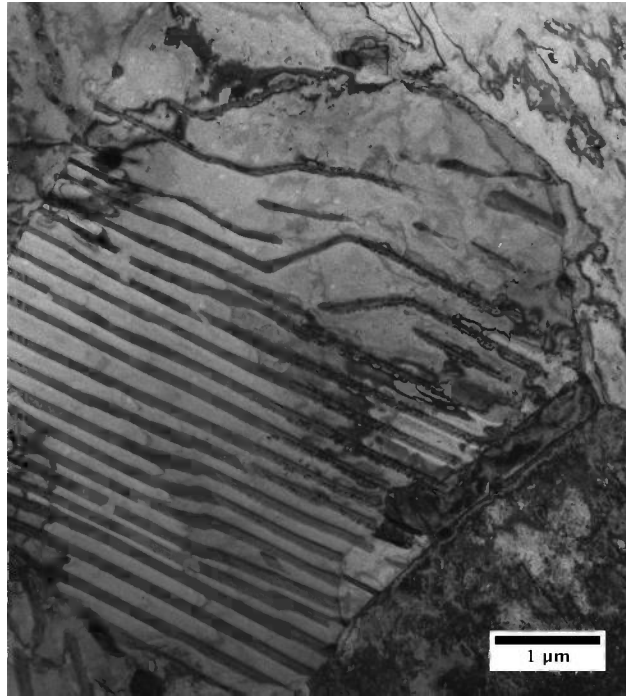


Figure A.4 Bright field TEM micrograph of C38M* after being deep rolled at 10.5 kN at room temperature. A characteristic angle at which the cementite laths appear to be sheared at can be seen in this micrograph.

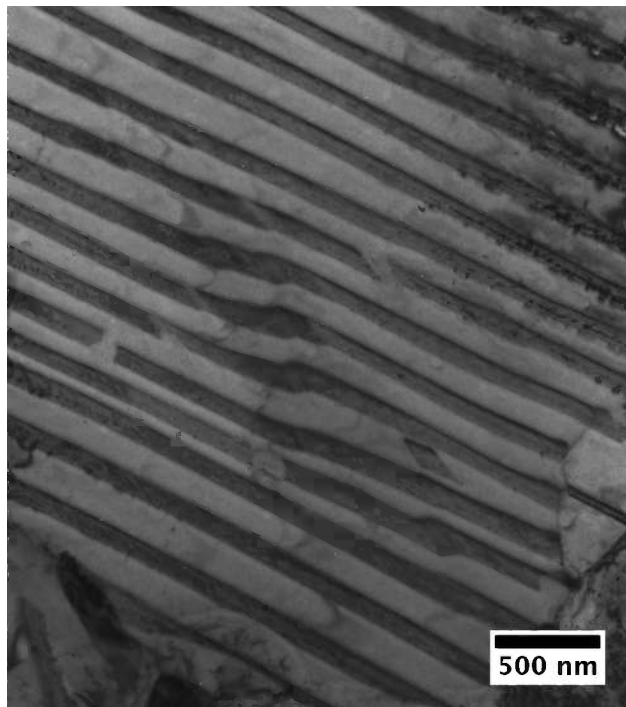


Figure A.5 Bright field TEM micrograph of C38M* after being deep rolled at 10.5 kN at room temperature. Straight cementite lamellae with a "kink" at a characteristic angle can be seen in this image.

APPENDIX B

X-RAY DIFFRACTION MEASUREMENT OF RESIDUAL STRESSES

B.1 X-Ray Diffraction Procedure

X-ray diffraction was performed at Colorado School of Mines using a Phillips X'Pert diffractometer and vanadium filtered Cr $k\alpha_1$ radiation source with a wavelength of 2.28970 Å. Samples selected for x-ray analysis from each deep rolled condition were in the as rolled condition, tested at the endurance limit for 5,000,000 cycles, run-out at the endurance limit, and tested for 20,000 cycles at a stress level such that failure was expected in 40,000 to 50,000 cycles. A sample from each material was also run in the polished state before deep rolling to establish a strain free baseline measurement.

Samples were positioned on the stage such that the incident x-rays were transverse to the length of the sample, in order that the fillet geometry would not shield the root of the fillet from x-rays. In this orientation the longitudinal residual stresses would not be measured directly but the hoop stresses present would be. The goal was to do non-destructive evaluation of residual stresses so fatigue tests could be interrupted then continued before further measurement. The stage height was set using a dial gage to align the root of the deep roll fatigue sample with the incident x-ray beam. Scans were run from $60^\circ 2\theta$ to $160^\circ 2\theta$ with a step size of $0.0040^\circ 2\theta$ and scan time per step of 6.985 s. After data collection, $k\alpha_2$ peaks were stripped from the data and peak positions and full width half max values were obtained using the X'Pert high score software package.

B.2 Analysis of X-Ray Diffraction Data

Evaluating the residual stresses resulting from the deep rolling process and how they evolve throughout fatigue testing will help to provide an understanding of the mechanisms operating in increasing the fatigue performance as a result of deep rolling. Residual stresses exist on different length scales within a material, type I stresses are macrostresses and are long range residual stresses spanning many grains, type II stresses are intergranular stresses resulting in property mismatches due to orientation mismatches between neighboring grains, and type III stresses are on the atomic scale and can result from coherency at interfaces and dislocation stress fields [58]. Long range macrostresses result in peak shifting in x-ray diffraction peaks and type II and type III stresses result in peak broadening [58, 59]. For residual macrostresses the change in the interplanar spacing for a set of planes can be evaluated using the Bragg equation, where d is interplanar spacing, λ is the incident x-ray wavelength, and θ is the peak position.

$$\lambda = 2d\sin\theta \tag{B.1}$$

From the interplanar spacings the residual strain can be calculated where ϵ is strain, d_0 is the initial spacing, and d_f is the final spacing measured [58].

$$\epsilon = \frac{d_f - d_0}{d_0} \tag{B.2}$$

It is possible to transform the residual strain measurements to residual stress measurements with suitable values of stiffness for the given plane [58].

In addition to measuring the peak position the width of the peaks can be useful in obtaining information about microstructural details. Three factors that can lead to peak broadening are crystallite size, non-uniform strain, and stacking faults [59, 60]. Peak broadening due to crystallite size and strain broadening can be separated by using a Williamson-Hall type plot [59–61]. A modified Williamson-Hall approach was presented by Revesz *et al.*, and in this analysis

$$\Delta K = \frac{2\cos\theta_B\Delta\theta}{\lambda} \quad (\text{B.3})$$

where $2\Delta\theta$ is the full width at half maximum of the peak measured in radians. The ΔK parameter can be divided into two parts that are due to small crystallite size and lattice strain (presence of dislocations), which are additive giving

$$\Delta K = \Delta K^S + \Delta K^D \quad (\text{B.4})$$

ΔK^S and ΔK^D are given by

$$\Delta K^S = \frac{0.9}{L} \quad (\text{B.5})$$

and

$$\Delta K^D = \left(\frac{\pi b^2}{2A}\right)^{1/2} \rho^{1/2} \left(\frac{2\sin\theta}{\lambda} C^{1/2}\right) \quad (\text{B.6})$$

where $(C^{1/2})$ is a geometrical correction factor relating to the reflection of dislocations, ρ is the dislocation density, b is the Burgers vector, L is the crystallite size, and A depends on the profile of the peak but can be taken as 10 in most cases. Substituting Equations B.3, B.5, and B.6 into B.4 gives

$$\Delta\theta\cos\theta = \left(\frac{0.9\lambda}{2L}\right) + \left(\frac{\pi b^2}{2A}\right)^{1/2} \rho^{1/2}\sin\theta C^{1/2} \quad (\text{B.7})$$

When $\Delta\theta\cos\theta$ is plotted versus $\sin\theta C^{-1/2}$ for a set of peaks from one scan a linear plot is generated and the y-intercept can be used to calculate the crystallite size L and the slope of the line can be used to calculate the dislocation density ρ . A more complete derivation of this modified Williamson-Hall approach is presented by Revesz *et al.* [61]. In a more general sense of the Williamson-Hall approach the crystallite size is still determined by the intercept of the line, but the slope is proportional to the strain in the lattice not just dislocations present.

B.3 Results and Discussion of X-Ray Diffraction

The data collected showed low reproducibility between duplicate runs on the same sample in many cases. When the modified Williamson-Hall analysis was applied to the data poor linear fits were obtained in some cases and in a few cases even a negative crystallite size was calculated (Figure B.1). The negative crystallite size is physically impossible pointing to either a problem in the analysis method or in the data. As an illustration of the variability in the data collected, data for C38N2 in the elevated temperature rolled condition will be presented. Figure B.2 shows the values of strain calculated for the C38N2 deep rolled then aged condition according to Equation B.2 for the as rolled condition, a fatigue test interrupted at 19,994 cycles at 621 MPa (90 ksi), a fatigue test interrupted at 5,135,518 cycles at 414 MPa (60 ksi), and stopped at 10,000,000 cycles at 414 MPa. This procedure was repeated for the (110) plane (Figure B.2a), (200) plane

(Figure B.2b), and the (211) planes (Figure B.2c) in ferrite. It is expected that the deep rolling process would induce a compressive residual stress at the surface of the deep rolled sample but in some cases tensile residual stresses are calculated and in many cases the value of the residual strains that are calculated are on the order of one hundredth of a percent. This may be due to the fact that near a free surface the residual strain tends toward 0 due to free surface effects. In fact the depth of penetration of x-rays can be calculated according to Equation B.8 [59]

$$x = \frac{K_x \sin \theta}{2\mu} \quad (\text{B.8})$$

where K_x is a function of the fraction of x-rays contributing to the total intensity taken to be 0.95 for this case giving $K_x = 3$, θ is the Bragg angle of the selected peak, and μ is the absorption coefficient which is 890.097 cm^{-1} for ferrite. These calculations were performed for the (110), (200), and (211) planes in ferrite and are presented in Table B.1. From Table B.1 it is obvious that most of the x-rays that are diffracted

Table B.1 – Calculated depth of penetration for Cr $k\alpha_1$ x-rays in ferrite.

	depth of penetration ($x \text{ } \mu\text{m}$)
(110)	9.52
(200)	13.5
(211)	16.5

come from the very near surface layers of the sample.

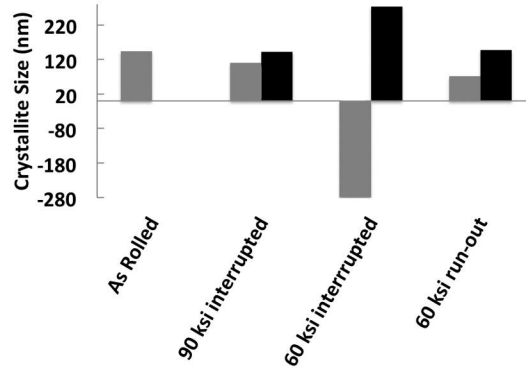


Figure B.1 Crystallite sizes for C38N2 deep rolled at room temperature then aged from the modified Williamson-Hall approach. The as rolled sample was tested before undergoing fatigue testing, the 90 ksi interrupted sample underwent 19,994 cycles at 90 ksi before x-ray diffraction, 60 ksi interrupted underwent 5,135,18 cycles at 60 ksi, and 60 ksi run-out underwent 10,000,000 cycles at 60 ksi. 60 ksi is the endurance limit of C38N2 deep rolled at room temperature then aged condition.

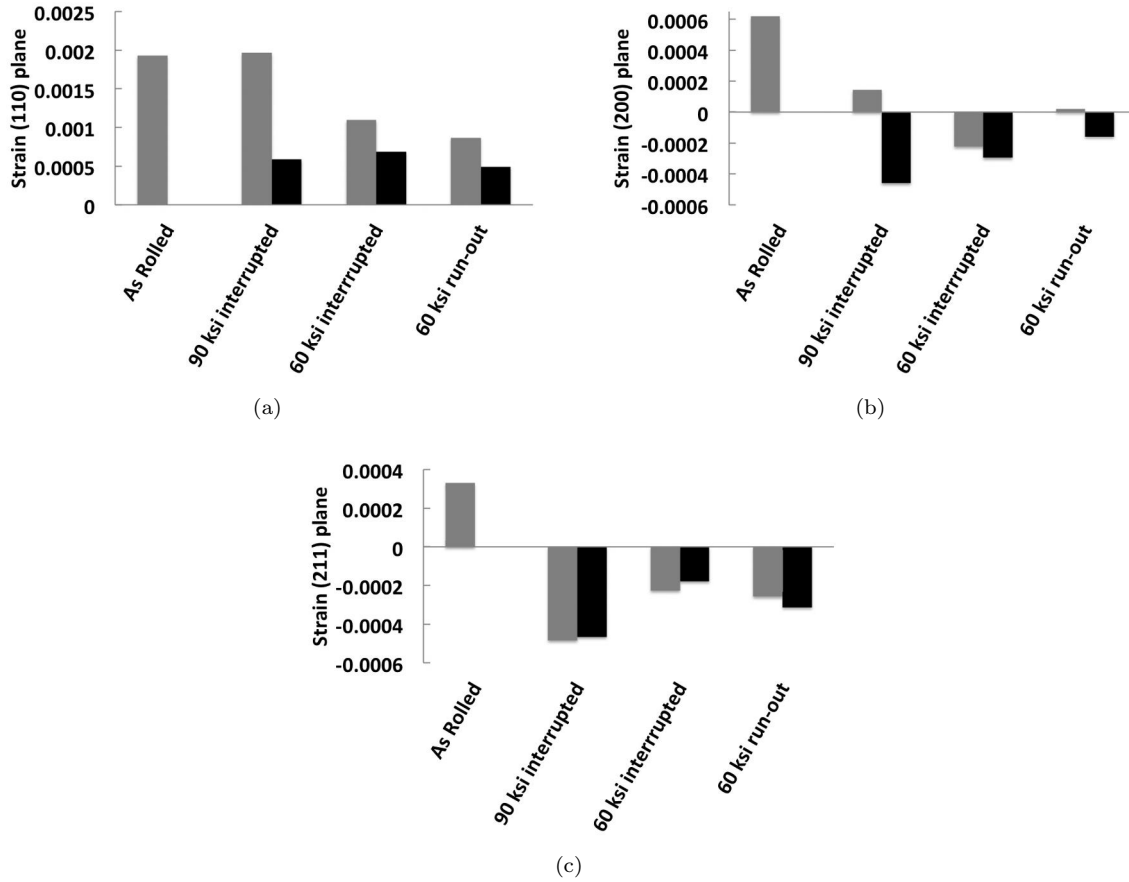


Figure B.2 Strains calculated using Equation B.2 for the (110) (a) (200) (b) and (211) (c) planes for C38N2 in the deep rolled at room temperature then aged condition. The as rolled sample was tested before undergoing fatigue testing, the 90 ksi interrupted sample underwent 19,994 cycles at 90 ksi before x-ray diffraction, 60 ksi interrupted underwent 5,135,18 cycles at 60 ksi, and 60 ksi run-out underwent 10,000,000 cycles at 60 ksi. 60 ksi is the endurance limit of C38N2 deep rolled at room temperature then aged condition.

APPENDIX C

SURFACE FINISH

Some preliminary work was initiated on the effects of surface finish prior to deep rolling on the fatigue performance of deep rolled samples. Surface roughness was measured using a WYKO optical profilometer and evaluated using Vision32 software. Parameters for quantifying surface roughness were R_a and R_q . R_a is the roughness average, which is the mean height over the measured array and R_q is the root mean square (rms) roughness and is the rms average of the measured height deviations taken within the evaluation length or area and measured from the mean linear surface. Both R_a and R_q are reported in μm and the smaller the number the smoother the surface.

Two samples of the C38M material were used, one being polished to the 6 μm finished used for the deep rolling study and one being evaluated in the as machined condition. The surface roughness for each condition was measured prior to deep rolling and again after deep rolling at room temperature. Table C.1 summarizes the values of R_a and R_q for the polished and unpolished conditions before and after deep rolling. Examples of the surface profiles taken before deep rolling are shown in Figure C.1 and after deep rolling is shown in Figure C.2.

Table C.1 – Surface roughness parameters R_a and R_q for the polished and as machined conditions before and after deep rolling with the cylinder and tilt terms removed from the analysis using Vision32 software.

	Before deep rolling		After deep rolling	
	R_a μm	R_q μm	R_a μm	R_q μm
C38M polished	0.077	0.167	0.116	0.151
C38M as machined	2.48	3.16	0.133	0.180

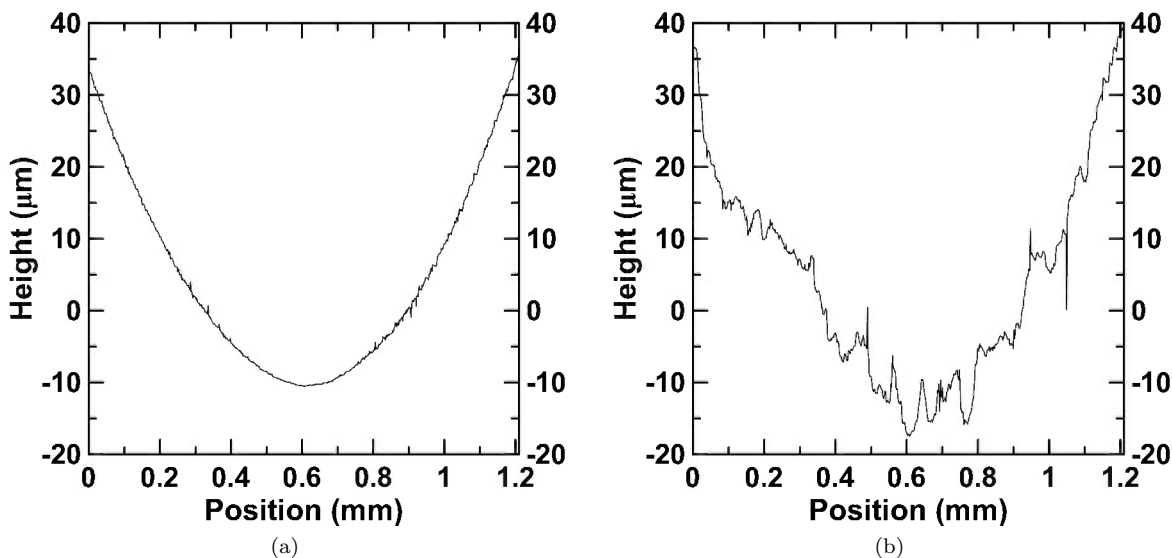


Figure C.1 Surface profiles before deep rolling for C38M in the polished condition (a) and in the as machined condition (b).

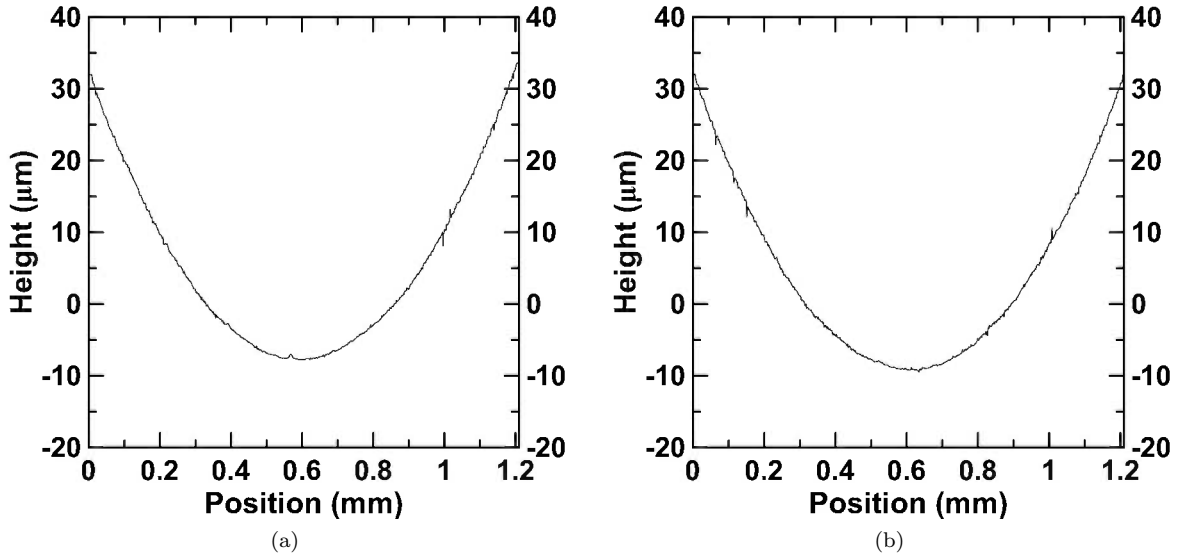


Figure C.2 Surface profiles after deep rolling for C38M in the polished condition (a) and in the as machined condition (b).

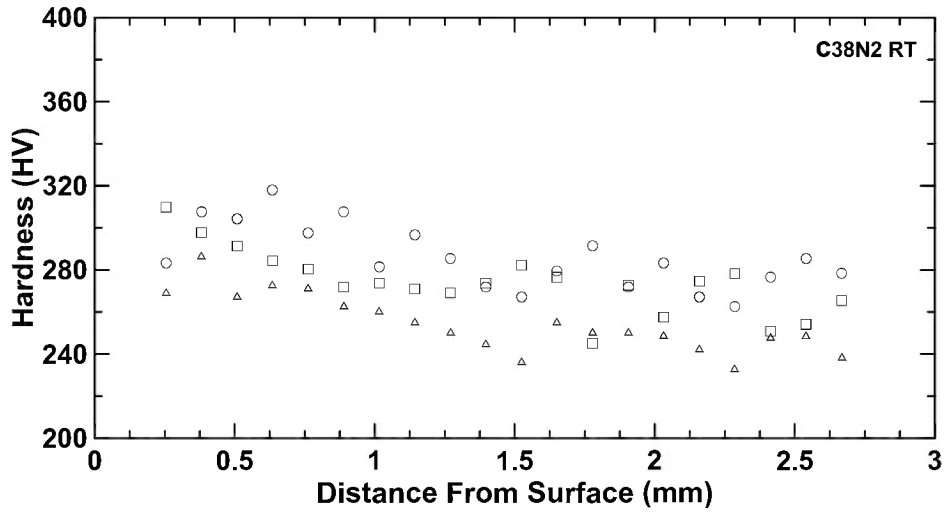
For the polished condition the surface finish stayed roughly the same before and after deep rolling, but the as machined surface finish was significantly improved by the deep rolling process. The R_a value for the as machined surface was $2.48 \mu\text{m}$ before deep rolling and after deep rolling it improved to $0.133 \mu\text{m}$. After being deep rolled both samples were tested at a fatigue load of 552 MPa (80 ksi). The polished then rolled sample survived $222,759$ cycles before failure and the as machined sample then deep rolled survived $202,056$ cycles before failure. This one set of samples is not enough to determine whether or not they have the same fatigue properties or if they are vastly different. In order to get a true perspective of surface finish on fatigue performance the endurance limit for the as machined then deep rolled condition would have to be established.

APPENDIX D

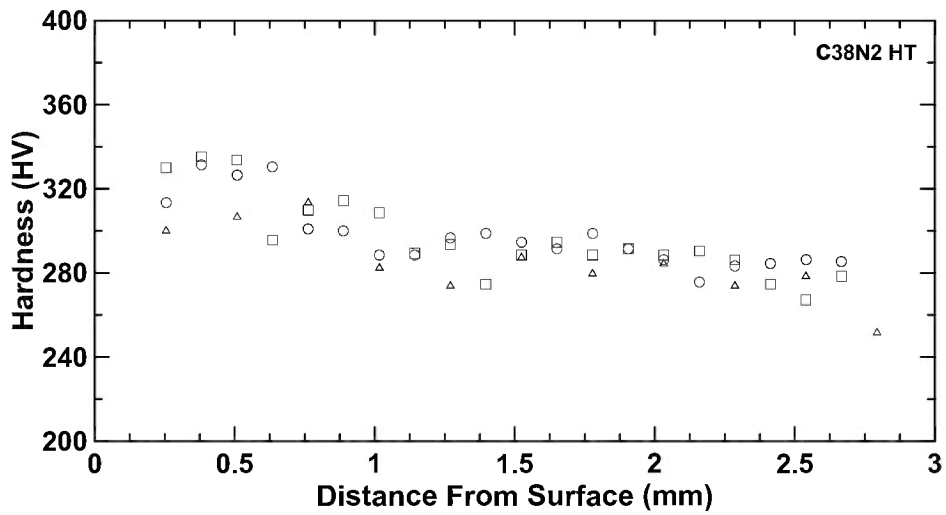
MICROHARDNESS

Microhardness traverses were performed on samples sectioned from the minimum diameter at the root of the fillet in the deep rolled samples. Sectioning was performed using a low speed diamond abrasive cut off saw. Samples were then cold mounted in a clear epoxy before being polished with 6 μm , 3 μm , and 1 μm diamond paste. Three profiles per condition were obtained using a 500 g load and a 10 s hold time using a Vicker's indenter. The conditions tested were room temperature deep rolled C38M and C38N2 as well as C38M and C38N2 deep rolled at 150 $^{\circ}\text{C}$.

The microhardness results for C38N2 are shown in Figure D.1 and the results for C38M are shown in Figure D.2. In both the C38M and C38N2 material an initial rise in the hardness near the surface of the fillet is seen then a decrease is seen as the indentations neared the center of the cross section. This initial hardness increase is expected as a result of the deep rolling process and is also seen in results obtained by Richards [8]. There is no discernible difference between the hardness profiles of the room temperature deep rolled and 150 $^{\circ}\text{C}$ deep rolled conditions for either the C38N2 or C38M materials.

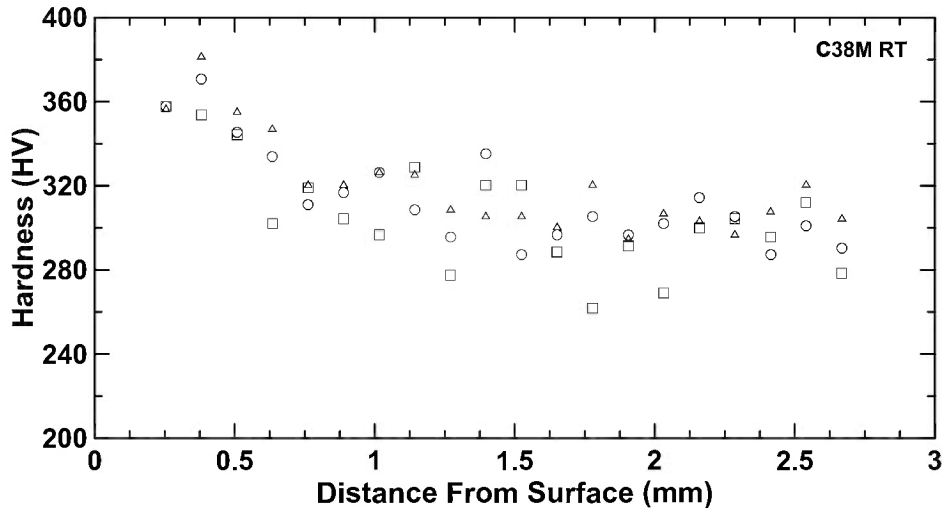


(a)

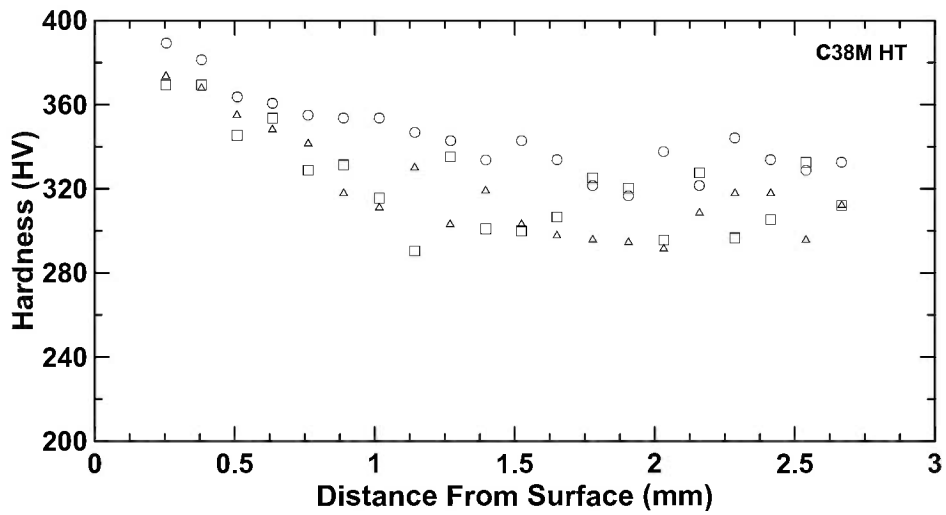


(b)

Figure D.1 Microhardness traverses of C38N2 deep rolled with a rolling force of 10.5 kN at room temperature (a) and at 150 °C (b). 0 represents the surface of the fillet in the root.



(a)



(b)

Figure D.2 Microhardness traverses of C38M deep rolled with a rolling force of 10.5 kN at room temperature (a) and at 150 °C (b). 0 represents the surface of the fillet in the root.